Multi-scale System for Middle Ear Surgery

Jae Hun So

THÈSE

présentée pour obtenir

le titre de Docteur délivré par Sorbonne Université

École doctorale: Science Mécanique, Acoustique, Électronique et Robotique

par

Jae Hun SO

Multi-scale Robotic System for Middle Ear Surgery

Soutenue publiquement le 17 Mai 2022 devant le jury composé de:

Véronique PERDEREAU	Professeure des Universités, Sorbonne Université	Présidente du jury
Sandrine VOROS	Chargée de Recherche Inserm - HdR, TIMC-IMAG Grenoble	Rapportrice
Florent NAGEOTTE	Maître de Conférences - HdR, Université de Strasbourg	Rapporteur
Laurent TAVERNIER	Professeur des Universités - Praticien Hospitalier, CHRUB	Examinateur
Frédéric PLUMET	Maître de Conférences, Sorbonne Université	Invité
Brahim TAMADAZTE	Chargé de Recherche CNRS - HdR	Co-directeur de thèse
Jérome SZEWCZYK	Professeur des Universités, Sorbonne Université	Directeur de thèse

Institut des Systèmes Intelligents et de Robotique (ISIR)
Pyramide Tour 55, 4 Place Jussieu
UMR CNRS 7222, Paris, France

Résumé

Le cholestéatome est une maladie de l'oreille moyenne qui, en absence de traitement, peut entraîner des complications graves (par exemple, une perte d'audition ou une paralysie faciale). Le seul traitement possible est l'intervention chirurgicale (résection). Cependant, cette méthode est invasive et entraîne une incidence élevée de cholestéatome résiduel, qui conduit à de nouvelles interventions post-opératoires. Un nouveau système robotique permettant de retirer efficacement tous les tissus infectés est proposé dans ce manuscrit. Le système robotique développé est composé d'un bras robotique (système à l'échelle macro) au bout duquel est attaché un micro-outil flexible (système à l'échelle micro).

Cette solution robotique innovante appelle au développement parallèle de nouvelles procédures chirurgicales en ayant pour objectif de rendre la résection robotisée du cholestéatome facile, intuitive et rapide. Dans ce manuscrit, les problèmes et les spécificités chirurgicales liés aux différentes phases de la chirurgie (c'est-à-dire les phases pré-opératoires et per-opératoires de la résection du cholestéatome) sont détaillés et les solutions optimales pour résoudre ces problèmes sont également proposées.

Dans un premier temps, ce travail se focalise sur la principale contrainte pour la phase pré-opératoire: faciliter le positionnement de la partie distale du robot dans l'orifice perforée (mastoidectomie). Les solutions proposées recourent à des méthodes de contrôle partagées vision/force dans lesquelles le mouvement linéaire est contrôlé par l'opérateur (par force ou position) et le mouvement de rotation est géré par un contrôleur basé sur vision. Ensuite, d'autres architectures de contrôle sont développées afin de contrôler l'organe terminal du micro-outil à l'intérieur de l'oreille moyenne durant la phase per-opératoire. Les boucles de contrôle intègrent un opérateur humain qui gère le mouvement du bout de l'outil. Enfin, la dernière contribution porte sur la gestion automatique du robot pour détecter et éliminer le cholestéatome résiduel avec une source laser embarquée (dans le micro-outil). Tous les contrôleurs proposés ont été soumis à plusieurs validations expérimentales et ont montré de bons résultats en termes de précision.

Mot-clés: Robotique chirurgicale, Interface homme-machine, Chirurgie de l'oreille moyenne

Abstract

Cholesteatoma is a disease affecting the middle ear, which can potentially lead to severe complications (e.g., hearing loss or facial palsy) in the absence of treatment. The sole treatment is a surgical intervention (resection). However, such a method is invasive and induces a high incidence of residual cholesteatoma, leading to second interventions. Thus, a novel robotic system has been proposed to tackle the problem of residual cholesteatoma by efficiently removing all the infected tissues.

The proposed robotic system is composed of a robotic arm (macro-scale part), to which a flexible micro-tool (micro-scale part) is attached at its distal part. However, different challenges had to be solved for developing the new surgical procedures integrating the robotic solution, wherein the expected objectives were to make the robotized cholesteatoma resection easy, intuitive, and fast. Across this thesis, surgical issues and requirements related to surgical phases (i.e., preoperative, per-operative phases for the cholesteatoma resection) are detailed and the ideal solutions tackling them are proposed.

First, we deal with the main preoperative phase concern : an easy installation of the tool-tip inside the incision hole. The proposed solutions use shared vision/force control methods in which the linear motion is controlled by the operator (by force or position) and the rotational motion is managed by a vision-based controller. Then, control architectures are developed for controlling the tool-tip inside the middle ear during the per-operative phase. The control loops include an human operator and handle the tool-tip motion. Finally, the last contribution bears on automatically managing the developed robot to detect and eliminate the residual cholesteatoma with an embedded laser source. All the proposed controllers have shown good results in terms of accuracy after several experimental validations.

Keywords: Surgical Robotics, Human Machine Interface, Middle Ear Surgery

Acknowledgements

The 3 years of Ph.D. research were for me an astonishing and rich experience. It is sure that it would not be achieved if there were not the entourage's support. So first, I would like to thank Professor Jérôme Szewczyk, my director, and Doctor Brahim Tamadazte, my co-director, who always stayed near me to support, to give me advice and lead to me. Your words always gave me comfort and confidence in my research work full of uncertainty, and your availability and support during the dissertation period was a huge motivation for me to finish this manuscript with ease.

I would also like to thank the members of my jury, the reviewers Doctor Sandrine Voros and Doctor Florent Nageotte, as well as the examiners President of the jury, Professor Véronique Perdereau, Professor Laurent Tavernier and Doctor Frédéric Plumet, for doing me the honour of reporting and reviewing my work and to attend my defence.

Now, I want to thank all the Office mates from J05, Mégane, Eléonore, Jimmy, Jesùs and Clemence, we exchanged a moment of sadness and happiness all together. Having wonderful office mates as you, was luck for me. And, how can I not forget Etienne, Charlotte, Félix, Omar, Mathilde, Angélina, Alexis, Antoine, Saman, Mahdi, Charlélie, and Elie, I thank you all for the pleasant working atmosphere and the daily exchanges during 16h break time sessions. You have become truly more than a friend to me. I truly thank your kindness for integrating a very "introverted" character like I am. For Ousmane, Solène, Lylian and Océane, we surely had not enough time to be closer++, however, it was a great time for meeting you and I wish you good luck to success with your Ph.D.!

Finally, I would like to finally thank my family, my mother, father, sister, and my beloved one for believing in me and for always supporting and encouraging me throughout my life.

Jae Hun.

Contents

List of Figures

List of Tables

Acronyms & Notations

Acronyms

MRI	*Magnetic resonance imaging*
MIS	*Minimally Invasive Surgery*
DOF	*Degree Of Freedom*
FoV	*Field-of-View*
OCT	*Optical coherence tomography*
ENT	*Ear, Nose and Throat*
RCM	*Remote Center of Motion*
HMI	*Human-machine Interface*
PID	*Proportional-derivative-integral*
PD	*Proportional-derivative*
MCMT	*Macro-comanipulation & Micro-teleoperation*
ROS	*Robot Operating System*
F/T	*Force/torque*
STD	*Standard deviation*
ANOVA	*Analysis of variance*
CT	*Computed tomography*
IBVS	*Image-based visual servoing*
PCA	*Principle Component Analysis*
TSP	*Traveler Salesman Problem*

General Introduction

Contents

Context

The origins of robotics and the first robotic system contain diverse names and dates, but they have always shared the same common objective: to prevent or assist humans when they perform heavy, dangerous, and tedious tasks. The integration of robotic solutions in industrial processes showed a great interest in enhancing productivity; repetitive tasks and/or dangerous tasks were gradually assigned to robotic solutions rather than employing humans.

Meanwhile, robotic systems also showed their potential for surgical applications. The first targets were traditional surgeries requiring a high level of expertise of the surgeon or surgeries in which operative posture were not always the most comfortable. Thus, remote control of surgical tool were experimentally tested with the objective to decrease fatigue [Madhani, 1998].

Moreover, additional advantages of using robotic system were found and developed. First, controlling a robotic system increases the precision of tool handling with respect to manual control. It allows canceling unnecessary motion such as hand tremor. Second, the operator's motion can be submitted to scaling parameter, thus reducing the dimension of tool motion and allowing a more sophisticated tool control. Third, vision sensor such

as camera, endoscope, ultra-sounds imaging, magnetic resonance imaging (MRI)..., give a better perception of the pathological area which can be hard to be seen by the surgeon in a physically constrained workspace or a millimetric scale workspace.

All these advantages have contributed to create robot-assisted Minimally Invasive Surgery (MIS), in which the surgery can be achieved without opening the entire cavity [Troccaz, 2013, Taylor et al., 2016]. To do so, small incision holes are perforated through long, rigid, and thin tools (*e.g.,* endoscope, forceps) are inserted. A typical example of MIS is laparoscopic surgery, in which 2 or 3 incisions are made on the abdomen to perform multiple kinds of surgery [Marescaux and Rubino, 2003]. Operating with the smallest opening has contributed to an increased recovery process for the patient, as it decreases infection probability and to less cavity tissue obliteration [Mohiuddin and Swanson, 2013].

Today, robot-assisted surgery is applied to more and more medical fields. Many researches bear on new robotic systems dedicated to specific surgeries. Following this trend, a project named μRoCS was created, funded by French Agency of Research (ANR). It includes robotic laboratories as ISIR (Institut des Systèmes Intelligents et de Robotique, Paris, France), FEMTO-ST Institute (Besançon, France), Inserm and the Besançon University Hospital. The main objective of this project was to develop a robotic solution for middle ear surgery, a particular type of surgery which is not yet investigated enough.

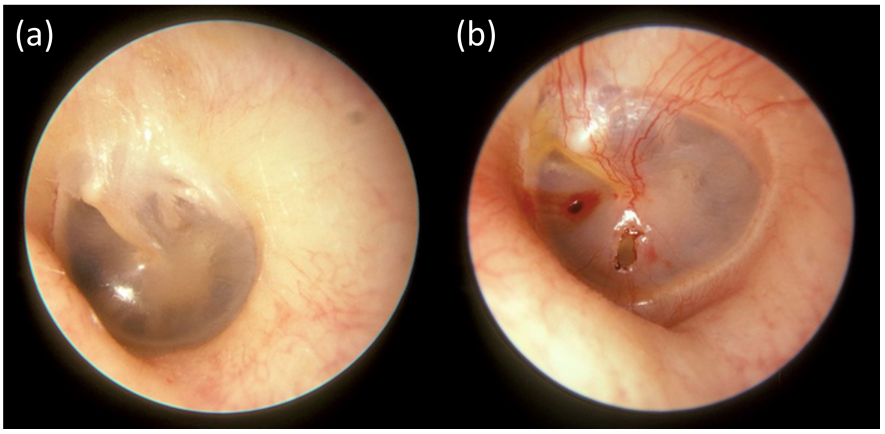

FIGURE 1: Examples of tympanic membranes: (a) healthy and (b) pathological[1].

The typical middle ear surgery that μRoCS investigates is the cholesteatoma resection. Cholesteatoma is an abnormal skin growth that occurs in the middle ear cavity. It is usually due to repeated infections. In France, it was estimated that one case per 10,000 citizens occurs every year. Over time, cholesteatoma expands in the middle ear, filling in the empty cavity around the ossicles and then eroding the bones themselves (ossicles, mastoid) (Figure 1). Cholesteatoma is often infected and results in chronically

[1]This image can be found at: https://www.labroots.com/trending/cell-and-molecular-biology/6750/enabling-eardrum-heal

draining ears. It also results in hearing loss and may even spread through the base of the skull into the brain. Nowadays, the only treatment for cholesteatoma is to surgically remove the infected tissues.

In case of delayed treatment, bone destruction may spread to the skull base, the inner ear, and the facial canal. The risks are then meningitis, vertigo, cophosis (total and permanent deafness), or facial palsy (paralysis). Such complications are very frequent and have a painful long-term impact on the patient's quality of life and/or require very heavy, expensive, and delicate surgical treatment. Therefore, it is crucial that cholesteatoma is removed before complications occur.

The current surgery protocol for cholesteatoma resection is very invasive and requires high-expertise and know-how of the surgeon. Also, it can be underlined that during such an intervention, the access and the visualization of the entire middle-ear cavity through the incision hole is very challenging. Consequently, a perfect ablation of the tissue is not guaranteed and leads, in 20%-30% cases, to a second surgery, 6 to 18 months after the first intervention due to residual cholesteatoma.

Contributions

A preliminary study was made in [Dahroug et al., 2018b] about how to improve the current cholesteatoma resection protocol. Multiple solutions to enhance this middle ear surgery were proposed, starting from the specificity of middle ear dimension, innovative technologies for tissue biopsy and ablation method as well as a blueprint of a novel surgical protocol are detailed within this study. A conceptual system with an actuated micro-tool embedding ablation tool and optical biopsy tool was proposed to be used in such a surgery.

Meanwhile, this thesis focuses on concretizing the suggested proposal by developing a proof-of-concept. Plus, the main objective is to enhance the surgeon's capability for ablating cholesteatoma tissue with ease while using this robotic system. It includes an intuitive control of the robotic tool, a faster installation process of the robot at the pre-operatory stage and a guarantee of total cholesteatoma ablation.

The first contribution of this thesis is the development of a robotic solution for cholesteatoma surgery [So et al., 2022c]. The targeted system is a Macro/Micro-scale robot composed of a redundant 7 degrees of freedom (DOF) on which is attached a 2 DOF robotized fiberscope mimicking an ablation tool. Two different control architectures are proposed to achieve a precise and intuitive robot control during ablation of pathological tissue inside the middle ear cavity. The first proposed control mode is based on the position-based teleoperation of the entire system using a joystick (Phantom Omni) as control device. The second one combines comanipulation of the 7 DOF robotic arm using

an embedded force/torque sensor and an end-frame teleoperation of the fiberscope using a lab-made in-hand joystick [So et al., 2020]. Experimental validation is performed to evaluate and compare the performance of both developed control schemes.

The second contribution of this thesis deals with the robotic system's installation process from an arbitrary position around the patient to the entry point of the middle ear cavity. Owing to the fact that the two foregoing control solutions for middle ear navigation are not suited for large motions, we propose a hybridization of these controllers with a vision-based approach. These two hybrid controllers separate the linear DOF which are controlled in tele-operation or in comanipulation, from the rotational ones which are managed simultaneously by a vision-based control law. All developed control methods are experimentally evaluated, compared, and analyzed [So et al., 2022a, So et al., 2022b].

The last contribution of this study deals with the control of a laser spot in the context of residual cholesteatoma resection in the middle ear. In order to accelerate and optimize this complex and delicate task, we propose a candidate solution to automatically generate optimal laser scanning paths inside the cholesteatoma regions and between these. Then, a laser spot emitted from an integrated source in the micro-tool follows the generated path, using an image-based control scheme. The proposed method and materials were experimentally confirmed using a lab-made simulation setup mimicking residual cholesteatoma regions inside middle ear cavity. The obtained results in terms of accuracy and behavior perfectly meet the laser surgery requirements [So et al., 2022d].

Structure of this manuscript

This manuscript is composed of 4 chapters :

- **Chapter 1** - This chapter presents the clinical background, *i.e.*, the definition of the cholesteatoma and the limitation of current treatment. This part also describes the main requirements for developing a robotic system dedicated to cholesteatoma resection using a laser source. It is then followed by a detailed mechatronic and software design of this system.
- **Chapter 2** - This chapter focuses on how to control the proposed robotic device for cholesteatoma resection. An overview of existing control strategies is detailed, including teleoperation and comanipulation. Two control methods are proposed, then experimentally tested to validate the enhanced performance for tool positioning task compared to manual handling of the designed tool.
- **Chapter 3** - This chapter presents an approach for the pre-operative installation of the robot. The proposed solution aims at an easy positioning of the tool-tip

near the entry site. Two types of hybrid controllers are developed in addition to teleoperation and comanipulation. All four solutions are experimentally tested during a peg-in-hole-like task, and then the results are analyzed and compared.

- **Chapter 4** - This chapter deals with the residual cholesteatoma treatment using a surgical laser. The proposed complete laser resection process includes a function which helps to verify and to plan a path covering all the surface of cholesteatoma small regions. Besides, a solution including the shortest path generator and an image-based laser spot controller is proposed. The developed function is assessed, analyzed through an experimental setup mimicking the surgical setup.

Related Publication

During the thesis, various solutions linked to the improvement on human-machine interface for the cholesteatoma resection were proposed, evaluated and published.

- International Journals:
  - So, J.-H., Tamadazte, B., & Szewczyk, J. (2020). Micro/macro-scale robotic approach for middle ear surgery. *IEEE Transactions on Medical Robotics and Bionics*, 2(4), 533-536.
  - So, J.-H.*, Sobucki, S.*, Szewczyk, J., Marturi, N., & Tamadazte, B (2022). Shared Control Schemes for Middle Ear Surgery. *Frontiers in Robotics and AI*.
- International Conferences:
  - So, J.-H., Sobucki, S., Szewczyk, J., Marturi, N., & Tamadazte, B. (2022). Hybrid controllers for middle ear surgery: towards efficient cholesteatoma removal. *Conference on New Technologies for Computer and Robot Assisted Surgery (CRAS)*.
  - So, J.-H., Tamadazte, B., Marturi, N., & Szewczyk, J. (2022). Dual-scale robotic solution for middle ear surgery. *2022 International Conference on Robotics and Automation (ICRA)*.
- Publication under review:
  - So, J.-H., Szewczyk, J., & Tamadazte, B. (2022). Image-guided laser steering for middle ear surgery. *2022 IEEE/RSJ International Conference on Intelligent Robots and Systems (IROS)*.

Finally, oral presentations were made through different seminars, during the PhD Student Days 2018 at ISIR, CAMI Days in Brest 2018, Summer School in SSR Montpellier 2019.

Chapter 1

Robotic System for Middle Ear Surgery

Contents

This first chapter describes the development of a mechatronic architecture for the robotic assisted middle ear surgery. As previously mentioned in the introduction, this study focuses on proposing an enhanced system to perform the cholesteatoma resection surgery, in which the surgeon receives an increased precision in control, resulting in a decreased difficulty for this surgical gesture. This chapter starts with an introduction of necessary requirements for the middle ear surgery. Section 1.1 deals with the anatomy of the middle ear and the specificity of cholesteatoma resection including the definition of the pathology and the current surgical procedure. Then, a list of benchmarkable robotic systems is presented in Section 1.2. Section 1.3 presents the proposed solution from mechatronic design to low-level software design.

1.1 Medical context

This section focuses on presenting a comprehensive description of the clinical background, *i.e.*, the occurrence of cholesteatoma. To begin with, the first part of this section describes the anatomical specificities concerning the middle ear where the cholesteatoma grows. Then, it is followed by a description of the pathology, its current treatment process, and a proposition of potential improvement points.

1.1.1 Anatomy of the middle ear

Our hearing system is located in both lateral parts of the head skull. From an anatomical point of view, this hearing part is divided into three portions: the outer ear, the middle ear and the inner ear as depicted in Figure 1.1.

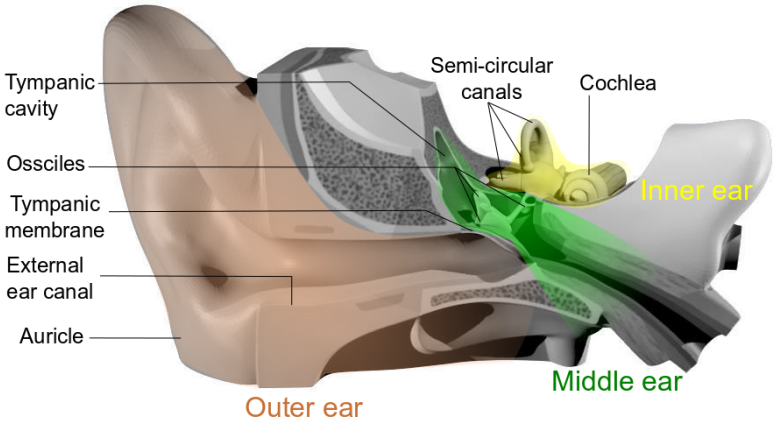

FIGURE 1.1: Anatomy of the hearing organs[1]

The **outer ear**, also called **external ear** is the part which is visible from outside, it includes the auricle, the external ear canal (external acoustic meatus) and the ear drum (tympanic membrane).

The **inner ear** is a part where vestibular system and auditory organ lie, forming the cochleovestibular system. The vestibular system is an organ responsible for sensing the balance. It is formed by three semicircular canals, filled with a fluid. The movement of this fluid inside these canals acts as a gyroscope sensor which provides information about the head orientation. The cochlea is a snail shape organ responsible for the hearing function. The sonic vibration transmitted from the outside is converted into a nervous signal which is then sent to brain.

The **middle ear** is the intermediate air-filled cavity between the inner and the outer ear. It includes the tympanic membrane and the tympanic cavity that shields three

[1]This image can be found on https://www.britannica.com/science/ear

tiny bones (*i.e.*, malleus, incus and stapes, also called *ossicular chain* or *ossicles*). The ossicles are anatomically linking the tympanic membrane and the cochlear oval window in order to induce the vibration from the outside to the inside of the inner ear.

To be more specific, the tympanic cavity is the main part of the middle ear cavity, it is bounded by the petrous portion of the temporal bone, the tympanic membrane, the inner ear structure. The temporal bone (Figure 1.2) is mainly composed of five parts:

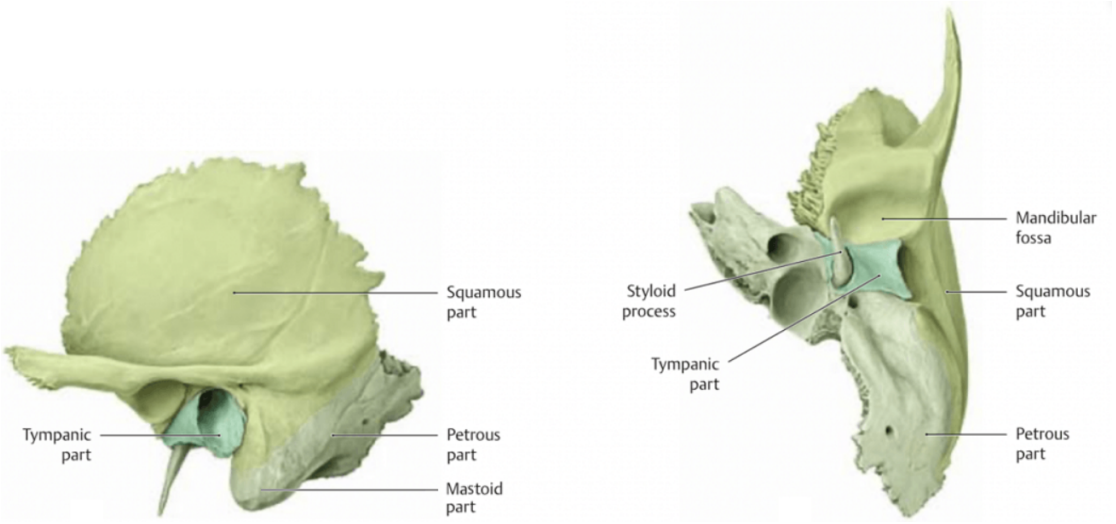

FIGURE 1.2: Anatomy of the temporal bone[2]

- Squamous portion: or *squama temporalis*, it forms the anterior and the upper part of the bone, where its inferior boundary is connected with zygomatic process. Its inferior surface presents depressions corresponding to the convolutions of the temporal lobe of the brain.
- Mastoid portion: it forms the posterior part of the temporal bone. It continues below into a conical projection, the mastoid process, which serves as site of attachment for muscles, an inferior projection of bone, palpable just behind the ear. A section of the mastoid process is filled with a number of air spaces (*i.e.*, mastoid air cells).
- Petrous portion: it contains, in its interior, the essential parts of the organ of hearing and its surfaces consist of canals, openings and grooves to transmit the facial nerve, acoustic nerve and veins.
- Tympanic part: it is a curved plate of bone lying below the squamous portion and in front of the mastoid process. It serves as the attachment of the tympanic membrane and the ligament for the ear.

[2]This image can be found on https://biologydictionary.net/temporal-bone/

- Styloid process: it serves as an attach point for ligaments and muscles linking the mandible.

The mastoid and petrous portions are used as passageway to reach the middle ear cavity in surgical context (more information is detailed below).

1.1.2 Cholesteatoma

The cholesteatoma is an abnormal skin growth in the middle ear cavity. It is an expansion of epithelial cells into the middle ear cavity. Each year, around 10 new cases per 100,000 inhabitants are reported in the world. It affects also men more than women and children less than adults [Olszewska et al., 2004]. The cholesteatoma can lead to several complications such as hearing loss, dizziness, facial palsy and brain damages. The enlisted symptoms are caused by the destruction of bony structures, respectively, hearing bones, inner ear organs, mastoid bone and cranial bone. The only solution to treat the cholesteatoma is to perform a resection surgery.

Origin

The cholesteatoma occurs when keratinizing stratified squamous epithelial cells accumulate in the middle ear cavity or other pneumatized portions of the temporal bone [Dhingra, 2010]. Figure 1.3 shows the difference between a normal and an infected (presence of cholesteatoma) ear tympanic membrane.

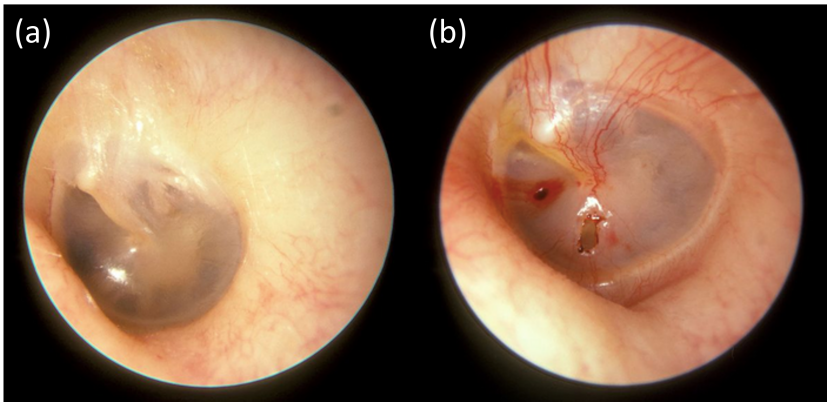

FIGURE 1.3: Examples of tympanic membranes: (a) healthy and (b) pathological[3].

The structure of the cholesteatoma is in two parts: the matrix, which is the keratinized squamous epithelium resting on a thin stroma of fibrous tissues, and a central white mass, consisting of keratin debris produced by the matrix (Figure 1.4).

[3]This image can be found at: https://www.labroots.com/trending/cell-and-molecular-biology/6750/enabling-eardrum-heal

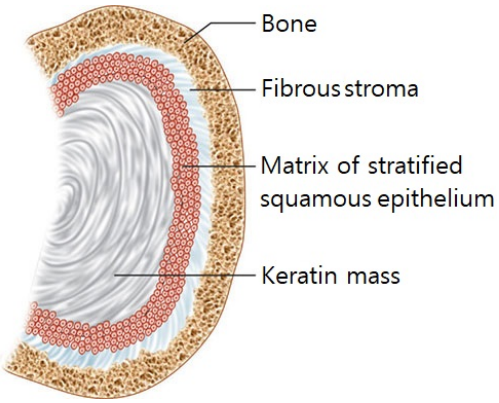

FIGURE 1.4: Structure of cholesteatoma expanding on a temporal bone [Bansal, 2012].

The genesis of cholesteatoma has been subject to debates. On one hand, the origin of congenital cholesteatoma [Nelson et al., 2002] is the remains of epithelial tissue behind an intact tympanic membrane. On the other hand, four different mechanisms or a combination of them [Olszewska et al., 2004] can be proposed for the development of acquired cholesteatoma (Figure 1.5):

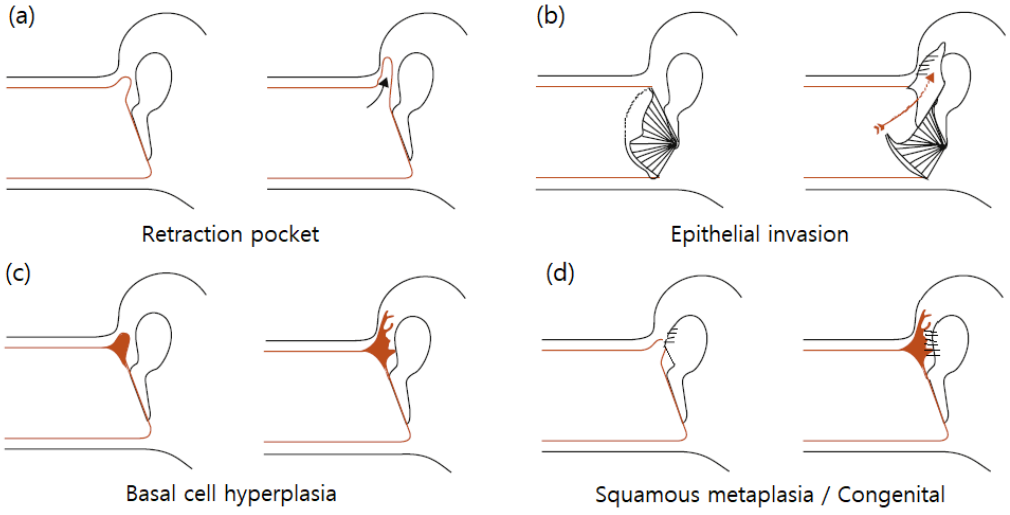

FIGURE 1.5: Types of cholesteatoma occurrence [Dhingra, 2010].

(a) **Invagination theory:** this theory is the most widely supported. It is an invagination of tympanic membrane from the attic or posterosuperior part of pars tensa in the form of retraction pockets. It is due to negative pressure in the middle ear, inflammation or both. The retention of keratin tissues inside the deep **retraction pocket** provokes the cholesteatoma [Wittmaack, 1933].

(b) **Epithelial invasion:** the squamous epithelium migrates from the margin of a pre-existing tympanic membrane perforation into the middle ear spaces [Habermann, 1888].

(c) **Basal cell hyperplasia:** the basal cells of the pars tensa (the upper part of the tympanic membrane) invade into the subepithelial space and form an attic cholesteatoma. Its cause is also the influence of infection [Rüedi, 1959].

(d) **Squamous metaplasia:** the middle ear skin (or *mucosa*) can be transformed into squamous epithelial tissue due to repeated inflammation and/or infection [Sade et al., 1983].

Once cholesteatoma penetrates inside the middle ear cavity, it invades the surrounding structures, first by following the path of least resistance. An attic cholesteatoma may extend backwards into the mastoid bone; medially, it may surround ossicles. Cholesteatoma has the property to destroy bone. It may cause destruction of ear ossicles, erosion of bony labyrinth, canal of facial nerve, sinus plate or tegmen tympani (mastoid portion of the tympanic bone bounding the tympanic cavity) and thus cause several complications.

Treatment

The treatment of the cholesteatoma is only possible by a surgery. The surgical process can be chosen depending on the location and the size of the detected tissue. Basically, there are two surgical protocols to treat cholesteatoma.

The first one uses the external ear canal to reach the middle ear cavity with small rigid instruments [Bae et al., 2019]. However, this protocol is not widely used as it can only be achieved at the early stage of cholesteatoma development which is hard to detect. Note that there is no particular symptoms until the moment when cholesteatoma penetrates in the middle ear and touches the ossicles or facial nerve.

That is why most surgeons use a second surgical procedure. It is based on performing a mastoidectomy, which consists of a large incision hole of about 20-25 mm of diameter in the mastoid and petrous portion of the temporal bone. This incision allows reaching the middle ear cavity, so that the physician has a direct access and vision of the middle ear cavity to mechanically remove the pathological tissues with adapted rigid surgical tools [Bordure et al., 2005]. Two options can be described for this process [Hildmann and Sudhoff, 2006]:

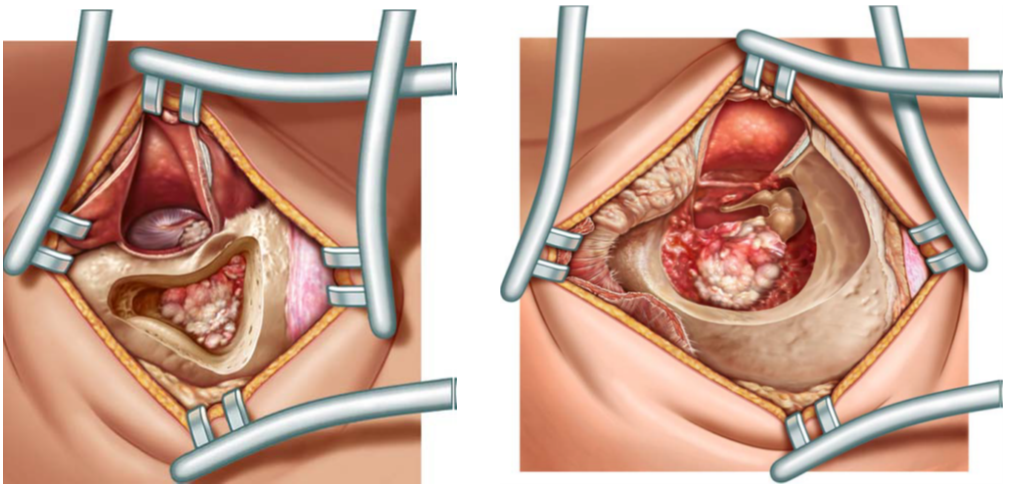

(A) (B)

FIGURE 1.6: Type of mastoidectomy (a) Canal wall up (B) Canal wall down. [Hildmann and Sudhoff, 2006]

- **Canal wall up**: the mastoidectomy process is to drill a hole to reach the middle ear, this perforated hole is separated with the external ear canal, forming a "wall" between the two of them (Figure 1.6). This technique is challenging for non-expert surgeons as the drilled hole gives insufficient field-of-view (FoV) resulting in a potentially incomplete resection. In this case, the rests of the cholesteatoma cells can regenerate inside the middle ear cavity after the operation and lead, in 20%-30% of procedures, to a re-operation [Stevens et al., 2019, Blanco et al., 2014].

- **Canal wall down:** the wall down process is to drill a larger hole than the wall up process, leading to a fusion of the two cavity (the perforated hole and the external ear cavity). This technique lets a clear view of the middle ear and makes easier for the surgeon to perform the resection. However, it is far more invasive than wall up technique, a reconstruction process of the ear canal is then mandatory, leading to a longer post-operative recovery.

The current surgical protocol, in addition to being quite invasive, requires a high know-how of the surgeon. This may partially explain the high failure rate of this type of surgery, caused by the residual cholesteatoma cells that remain after the intervention [Aquino et al., 2011]. In addition, with such techniques, by lack of appropriate tools, (*e.g.*, surgeons use traditional, rigid, and hook-shaped, micro-surgical tools to rack the cholesteatoma [Dahroug et al., 2018b]), the access to the entire epitympanum cavity is impossible. It may result in an increased risk of infection and recurrence of a deeper cholesteatoma by the exposure of the ossicles. It is thus reserved for severe or recurring cases [Alper, 2004]. Hence, there is a high demand for improvement of current surgical

procedures towards less invasive approaches by reducing the incision hole, as well as improving the efficiency of the ablation of infected pathological tissues, and then to avoid repeated surgery.

Objective of improvement

As explained, it is increasingly important to make mastoidectomy evolve toward less invasive (*i.e.*, avoid wall down procedures and reduce the hole size in the wall-up ones) and more efficient techniques *i.e.*, avoid any second intervention.

Improvements in cholesteatoma resection surgery can be achieved in 4 points:

- **Invasiveness:** using the wall up rather than the wall down technique. As described above, the wall down procedure is too invasive and its recovery time is long [Hildmann and Sudhoff, 2006]. It means that wall up technique has to be prioritized. Hence, the main disadvantage of the wall up procedure needs to be fixed, *i.e.*, reduced vision, archaic resection method and the problem of residual cholesteatoma.
- **Optics:** the problem of the reduced FoV for a wall up protocol has to be fixed. Current method to visualize the workspace is to use an oto-microscope during the surgery and an oto-endoscope to get an improved visual feedback of the middle ear [Bordure et al., 2005]. However, it needs a high expertise of the surgeon who has to mentally project the position of the perceived cholesteatoma debris. A possible solution would be to integrate an imaging technique embedded in a flexible tool. The flexibility could be obtained for example, by relying on continuum tool structure such as a soft robot [Burgner-Kahrs et al., 2015],
- **Resection method:** as presented above, conventional tool can potentially cause debris inside the middle ear. It is also related to the surgeon, who needs to be very careful to minimize the occurrence of residues, *i.e.*, a high level of concentration is mandatory. To remedy this, other resection tools can be integrated such as using a laser source to burn the tissue [Hamilton, 2005, Caffier et al., 2008], or using a precise cutting tool manufactured by MEMS technology [Gosline et al., 2012].
- **Residual cholesteatoma:** even if a change of tool can enhance the resection precision, there is a risk of residual disease that obviously remains as a challenge. A real-time imaging technique could be very useful to visualize residual cholesteatoma. A possible solution could be to use Optical Coherence Tomography (OCT) [Huang et al., 1991]. It is a modern imaging method using the same operating principle as echography but with a light source instead of ultrasonor one. It is said to be better than other imaging methods, *e.g.*, ultrasound imaging [Jang et al., 2002] or fluorescence technique [Lademann et al., 2007]. The benefit of OCT would entail from

a real-time and precise detection of the cholesteatoma. Note that various studies have already demonstrated the feasibility of integrating such imaging technique in middle ear context [Monroy et al., 2015, Pitris et al., 2001, Tan et al., 2018].

As mentioned before, the μRoCS project intends to propose a solution to tackle the problems of current treatment protocol and also find out a breakthrough associated with an innovative method for residual cholesteatoma detection and resection. The optimal solution would be to use high dexterity continuum robots with an embedded laser source and a real-time biopsy tool (associating OCT and fluorescence imaging in the same probe). Besides, an intuitive human machine interface (HMI) for the complete system control would be necessary to provide clear clinical added values for the patient and the surgeon.

1.2 Overview of robot-assisted middle ear surgery

As the main pathology has been described above, the objective of this work lies in developing a robotic system that can improve cholesteatoma resection surgery. Logically, the next step is to identify existing robotic solutions for middle ear surgery and also other benchmarkable solutions useful for creating an optimal robotic system for cholesteatoma resection. The following paragraphs highlight existing solutions dedicated to middle ear surgery or related intervention. Then, technical solutions applied in other surgical fields are also investigated to find the ideal robotic system dedicated to middle ear surgery.

First, robotized MIS is gaining more and more importance through increasing accuracy in control of surgical tools [Vitiello et al., 2013]. The use of robotized MIS toin smaller workspaces (millimetric scale) is also a significant trend. Thus, Ear, Nose and Throat (ENT) surgery would greatly benefit from a robotic assistance as the presented cholesteatoma surgery suffers a lack of vision and shows a very limited workspace.

1.2.1 Existing middle ear surgical robots

Two main surgical procedures are present for the middle ear: mastoidectomy and hearing organs replacement. For both procedures, robots were designed to enhance accuracy, dexterity and ergonomy for the physician. Primary studies were devoted to integrate robotic solutions dedicated to other types of surgery, into ENT surgery [Parmar et al., 2010]. Then, multiple studies have been conducted to integrate specific robotic solutions.

Robotic solutions for mastoidectomy

Mastoidectomy is a delicate surgical act to perform an access to the middle ear cavity. Perforating the mastoid bone is challenging since the perforation has to be done in delicate manner behind the auricle. In the way of perforation, the surgeon has to avoid damaging the facial nerve [Hildmann and Sudhoff, 2006] or blood vessel in which a small damage may lead to heavy consequences. Some studies on robot-assisted mastoidectomy have been investigated in the literature.

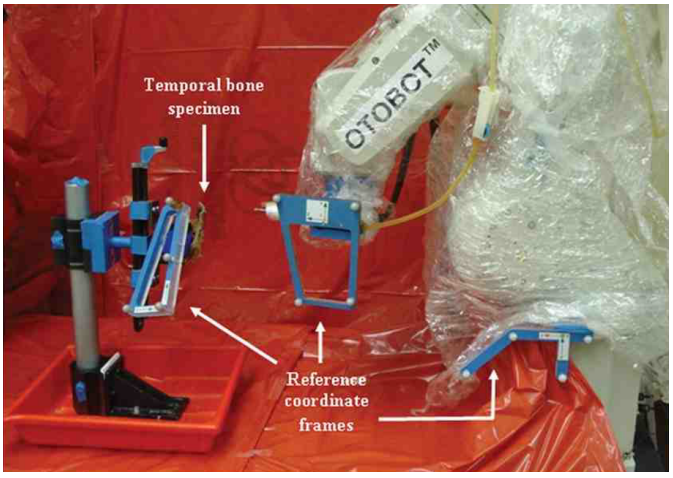

FIGURE 1.7: *OTOBOT* system with multiple optical markers [Danilchenko et al., 2011].

A proposed system in [Danilchenko et al., 2011] is named *OTOBOT*. It consists of an industrial robot arm (Mitsubishi RV-3S) with an attached custom-built end-effector which holds a surgical drill. This system is equipped with an optical tracking system to measure the pose of both the robot and the patient represented in the same frame. When the surgical drill perforate a hole, external optical sensor tracks pre-attached markers on the head and leads to a safe trajectory following whether the human head moves.

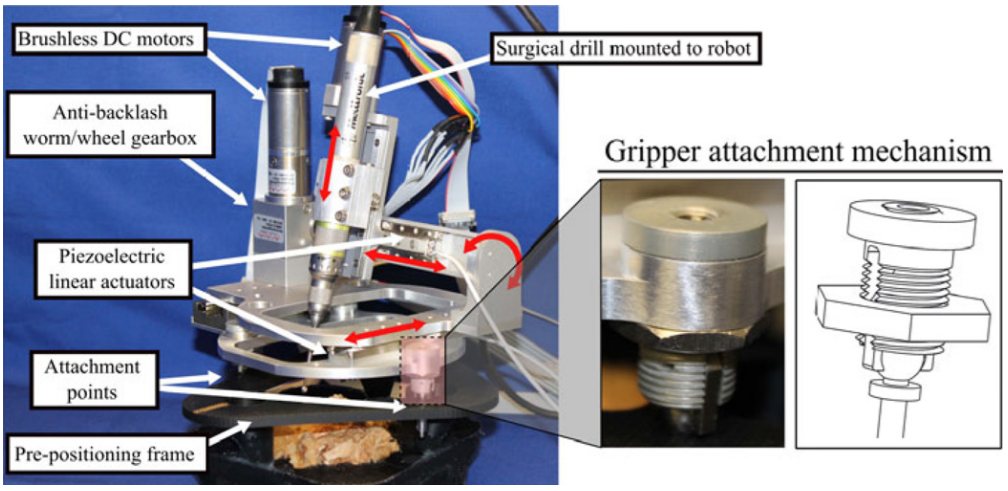

FIGURE 1.8: Bone attached mastoidectomy robot [Dillon et al., 2014].

Another system from [Dillon et al., 2014] uses a different strategy to execute the mastoidectomy. The specificity of this solution bears in the basic installation, where a custom built 4 DOF serial robot is fixed directly on the temporal bone as depicted in Figure 1.8. An installable robot system contributes in eliminating registration steps and then the need for optical tracking system in opposition to *OTOBOT*.

As explained earlier, mastoidectomy is only a part of middle ear surgery protocol. Moreover, it is a surgery which is performed outside of the middle ear cavity, whereas the cholesteatoma resection has to be achieved inside this cavity. Note that, robotized mastoidectomy could be integrated in the resection surgery (in canal wall up technique) but it is not the fundamental part of the cholesteatoma resection surgery.

Robotic solutions for hearing organs replacement:

Defected hearing organ replacement are mainly dedicated to cochlear implantation, tympanic membrane grafts or ossicular chain replacement which requires high accuracy, safety and reproducibility.

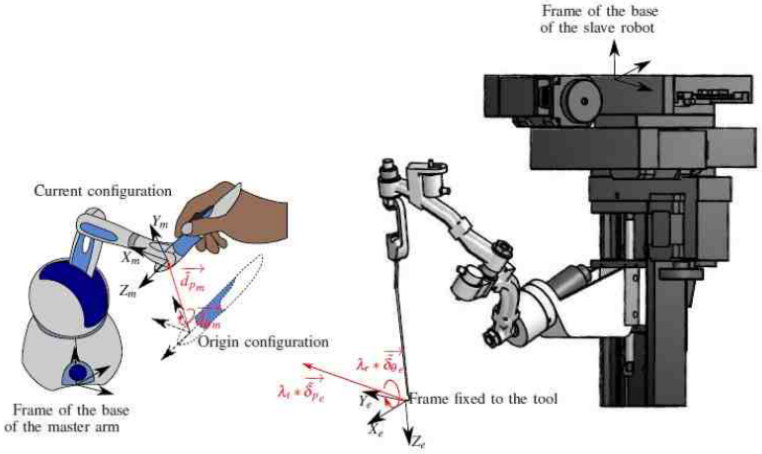

FIGURE 1.9: RobOtol system [Miroir et al., 2012]

A teleoperated robotic system named RobOtol, was proposed to carry out a stapedectomy[4] surgery through the external ear canal [Miroir et al., 2012, Nguyen et al., 2012]. It consists of a slave robotic arm and a master joystick (Figure 1.9). The system is designed to use three robotic arms simultaneously, whereby each arm has 6 DOF. The kinematic structure has been sophistically studied so that each arm preserves the field of vision to the surgeon. A rigid resection tool can be attached at the end-effecting part of this robot for the stapedectomy.

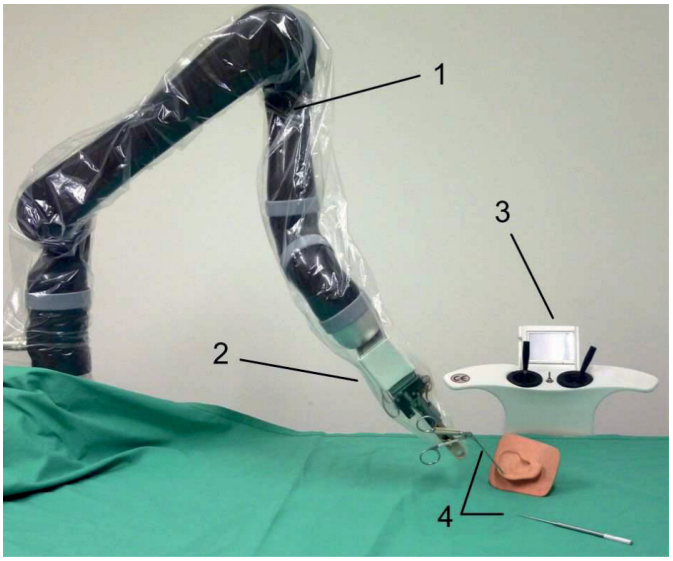

FIGURE 1.10: Macro-micro system for middle ear surgery [Entsfellner et al., 2015] with (1) Robotic arm (2) Micro-tool handling unit (3) joystick (4) conventional tools.

At Munchen University, [Entsfellner et al., 2015] suggest a robotic system which has a 6 DOF robotic arm with an attached 4 DOF telemanipulator for middle ear surgery

[4] A surgery to replace the stapes bone of the middle ear cavity.

(Figure 1.10). The micro-tool is a traditional surgical tool widely used during ENT surgeries. Named as Micro-Macro Telemanipulation System (MMTS), this robotic solution can also be used as a tool handling device. An adaptor is designed for gripping different tools (*e.g.*, endoscope or driller). Moreover, the system is equipped with four force sensors for measuring the applied force at the instrument tip.

However, the presented solutions only integrate rigid tools and do not include any dexterous instrument for intracorporeal (*e.g.*, middle ear cavity) fine movement execution. Study also shows that micro-scale rigid tool can break during the surgery [Koliakos et al., 2008] which raise a safety issue for the patient.

1.2.2 Technical benchmark for middle ear surgery

As mentioned above, current existing solutions for robotic middle ear surgery are dedicated to hearing organs replacement located in the lower part of the middle ear cavity. Thus, most studies propose control of rigid tool inserted via the external ear canal. As for cholesteatoma resection, its workspace lies on the upper and lower part of the middle ear cavity where a straight and rigid tool cannot get access inside (gray surface in Figure 1.11). Presented approaches are not suited for cholesteatoma surgery requiring high accuracy and dexterity due to small access hole. Besides, the ossicles and facial nerve presence within the middle ear cavity makes the surgical task even more complex and risky. Thus, other techniques used in a different context than middle ear surgery had to be investigated.

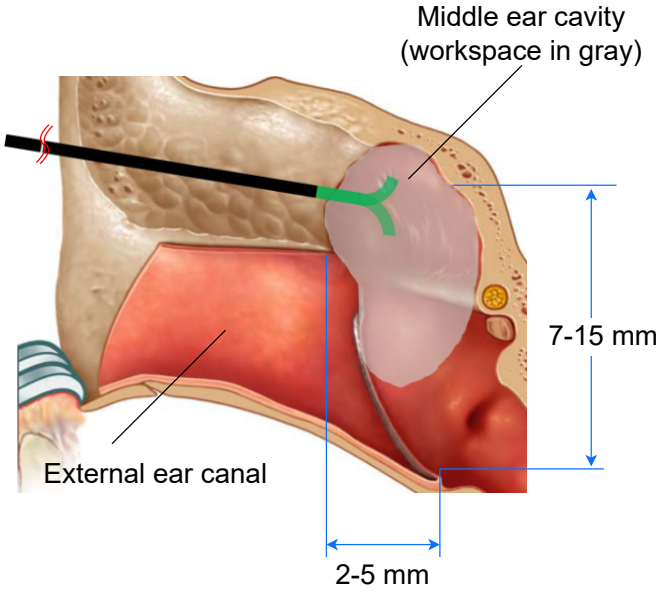

FIGURE 1.11: Conceptual scheme of the desired surgical procedure using flexible manipulator.

According to [Dahroug et al., 2018b], the estimated workspace of the middle ear cavity is about 2-5 mm width and 7-15 mm height and 5 mm of depth. In his study, the required DOF of the micro-scale tool is at least 4 DOF for the end-effector and at least 4 DOF at the proximal part of the tool. To tackle the problem of the fragile, tiny and complex-shaped workspace of middle ear surgery, it is suggested using a bendable tool.

Different techniques of flexible robot can be found in the literature. It can be :

- a conventional manual flexible endoscope where actuating parts are added [Ott et al., 2011]. Such enhancement requires a kinematic modeling of the flexible part and an approximation of the obtained flexion angle depending on the endoscope's trigger (or handle) angle.
- a concentric tube robot which consists of an assembly of multiple elastic tubes in a telescopic manner. The base tube should be a straight, rigid tube, and the others are pre-curved. By sliding and/or rotating the elastic tubes with respect to the base tube, the tool-tip could reach different positions in the space [Gosline et al., 2012].
- a cable-driven flexible unit is a tube with several asymmetric cutouts. The tube bends with the actuation of a single tendon [Fichera et al., 2017], a material which is between rigid and elastic is necessary to make such tube (*e.g.*, nitinol). The number and the width of cutouts determine thes flexion angle and the curvature length.

1.2.3 Macro/micro manipulator

As mentioned above, the flexible tool seems to be an interesting solution for middle ear surgical intervention. However, the micro-scale tool has to be positioned at the entry point and held still before beginning the operation. It means that positioning the tool is also a fundamental task to engage middle ear surgery. That is why, we assumed that a robotic holder which carries the micro-tool would be necessary. This concept is also known as macro/micro manipulator in the literature, including a distal tool (micro-scale part) mounted on a robotic holder (macro-scale part).

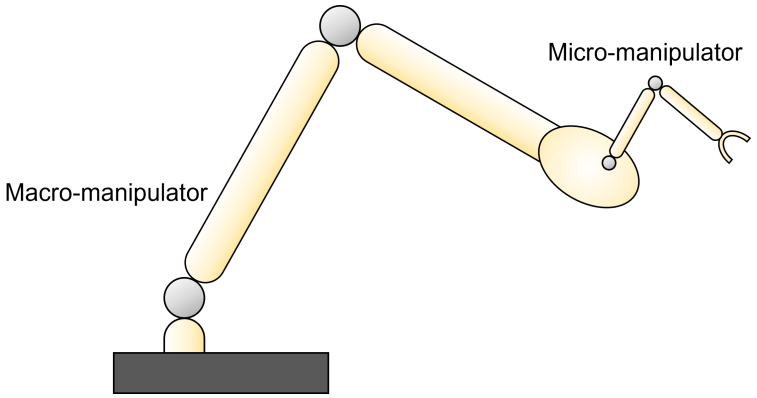

FIGURE 1.12: A macro/micro manipulator scheme.

The macro/micro manipulator was first introduced for industrial tasks, such as the grip-and-move actions [Sharon et al., 1993], based on a system composed of a robotic arm and an attached multi-DOF gripper (Figure 1.12). Previous researches took interest mainly in simplification of the system dynamics and optimized control of these robots under industrial context. As the main difficulties of MIS are narrow access and limited workspace, many researches were performed in order to adapt the macro/micro robot concept to this particular surgical context. Note that, the concept of combined robotic system integrating a robot arm and a micro-tool serially arranged is not a novelty in medical robotics, especially in MIS approaches.

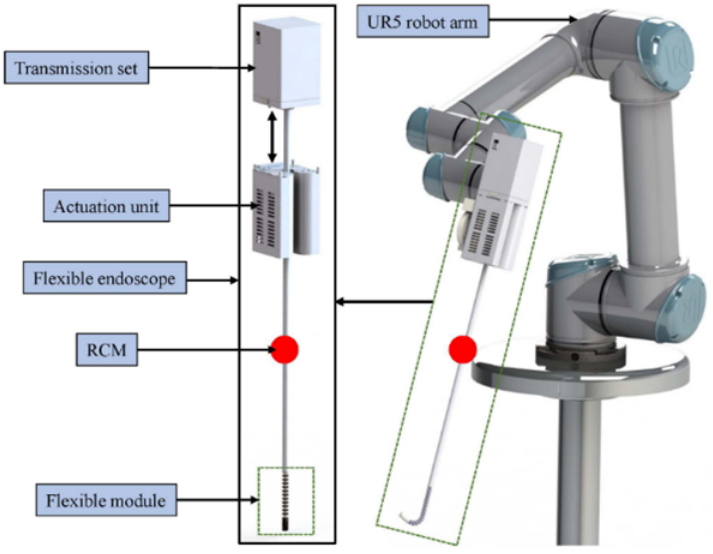

FIGURE 1.13: A macro/micro manipulator integrating a flexible endoscope [Zhang et al., 2020]

A recently developed macro/micro manipulating system which consists of an automatic endoscope handling device [Zhang et al., 2020] integrating a 4 DOF flexible tendon-driven continuum endoscope on a UR5 robot arm (as can be seen in Figure 1.13). This

system performs an automatic trajectory tracking based on a visual servoing controller using the endoscopic images as control feedback. A control method was developed to control the end-effector of the flexible module while the straight part remains fixed at the Remote Center of Motion (RCM). Even if it is dedicated to an imaging function, it can be considered to be a potential candidate system applicable to middle ear surgery.

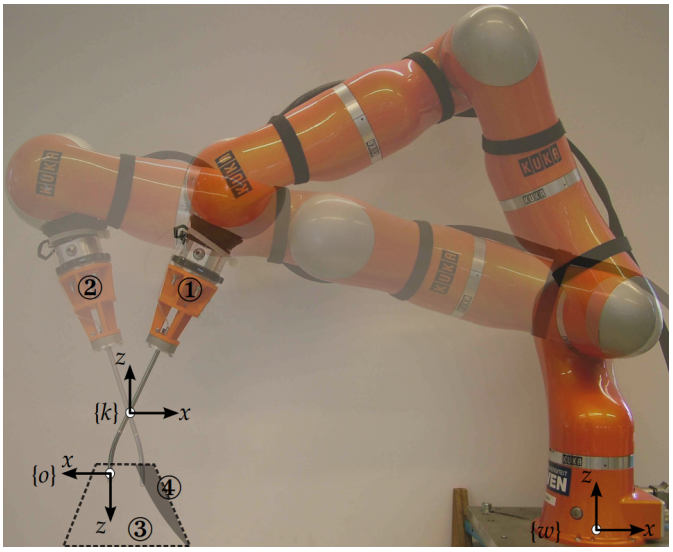

FIGURE 1.14: Heart surgery robot system [Smoljkic et al., 2016].

In surgical context, [Smoljkic et al., 2016] suggests a system merging a 7 DOF KUKA manipulator with a flexible catheter-like micro-tool for heart surgery (as depicted in Figure 1.14). In conventional catheter insertion in the blood vessel, the surgeon only have 4 DOF, 1 linear motion corresponding to the insertion and 3 rotation around trocar. However blood vessels have complex bending features that make the insertion task complicated. This study shows the benefit of using a flexible tool inside vessels where 2 additional DOF on the tool-tip enable an easier insertion of this actuated catheter.

The presented solutions shows a great interest in performing a task in a small and complex workspace. Based on the requirement of the middle ear surgery, the macro/micro manipulator concept seems to be suitable for the cholesteatoma resection, and in extent, for middle ear surgery. The macro-scale part would be an extra-corporeal robotic arm used as a tool-holding device and the micro-scale part would be an intracorporeal flexible micro-robot embedding the laser and imaging technique.

1.3 Proposed solution

As mentioned, the proposed solution is a macro/micro system which consists of a macro-tool holder and flexible micro-tool satisfying the requirement of the cholesteatoma resection. Thus, the mechatronic and software developments of this robotic device is presented

below.

1.3.1 Mechatronic design

The primary phase of our development deals with the mechatronic design of a macro/micro robotic system dedicated to middle ear interventions. The system consists of a Panda robot arm (macro-scale system) on which is fixed a flexible tool (micro-scale tool). The flexible micro-scale tool is an actuated tendon-driven continuum flexible fiberscope in the lumen of which a surgical laser and a optical biopsy tool can be embedded at the distal part. Note that this micro-tool device is in development phase at FEMTO-ST, Besancon [Nguyen et al., 2021], the actuated fiberscope we use in this study is a representative model of a real flexible micro-tool.

Macro-scale part

In this work, the macro-scale part which serves as a tool handler is a 7 DOF Panda arm from Franka Emika (Figure 1.15). Its redundant property allows an internal motion which helps a safer use of the robot. Note that we conserved the original joint-level internal motion control of this macro-scale robot in this work.

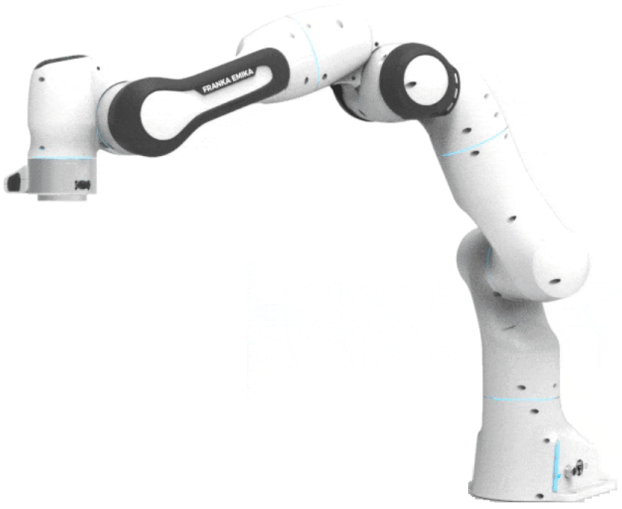

FIGURE 1.15: Panda Robot from Franka Emika®[5].

[5]This image is taken from: https://www.franka.de/

Micro-scale part

The micro-scale part is a 2 DOF actuated system. One is for translation of the whole flexible fiberscope and the other for actuating its flexible part (flexion).

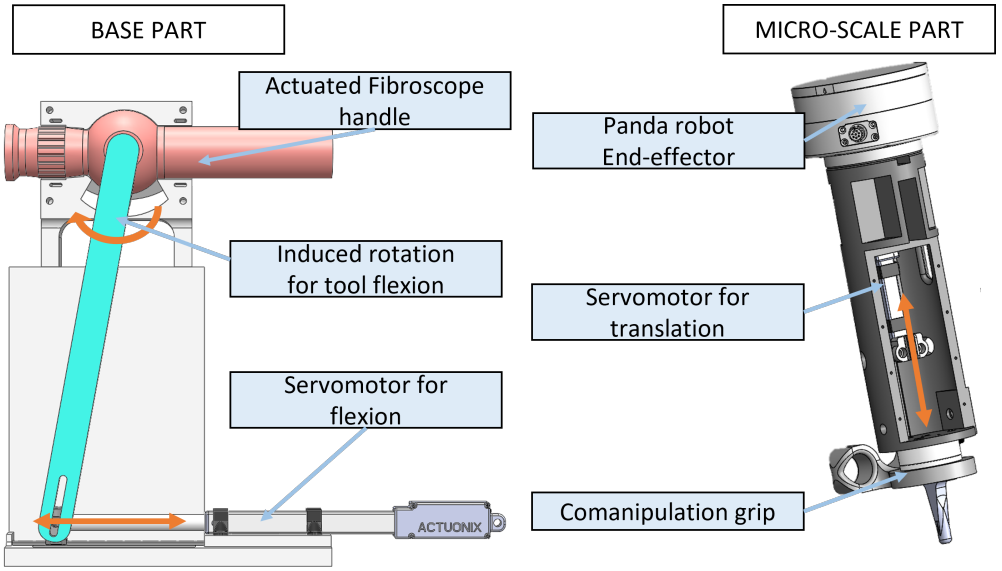

FIGURE 1.16: Transmission mechanism of the micro-scale part of the developed system.

This flexible micro-scale tool consists of a fiberscope from Karl Storz (11292AD1). As explained, it has two actuated DOF, fixed at the Panda end-effector. The flexible tool is namely a $\pm 90°$ flexion and a 50 mm translation (Figure 1.16) device. It is mounted in such a way that its straight configuration coincides with the axis of the distal part of the Panda robot.

The micro-tool transmission is assembled in two parts: the flexion transmission unit controlled at the base part and the translational transmission inside the chassis of the micro-scale part (as depicted in Figure 1.16).

- **Translation:** For the translational motion of the fiberscope, a linear actuator is embedded in a chassis directly mounted on the macro-scale part end-effector. A servomotor from Actuonix (L16-50-35-6-R) controls the position of the linear joint through a screw-nut transmission mechanism.
- **Flexion:** The flexion actuation unit is located at the proximal end of the fiberscope (handle/trigger) and is positioned outside the system due to its unsuited payload. The flexion is produced by a linear shaft coupled to the original fiberscope handle through a bilateral punctual contact. This linear shaft is actuated by an linear servomotor from Actuonix (L16-100-35-12-P) which also provides the measure of the fiberscope flexion angle through a converting equation (Figure 1.16).

The assembled architecture including the macro-part and the micro-part is depicted in Figure 1.17.

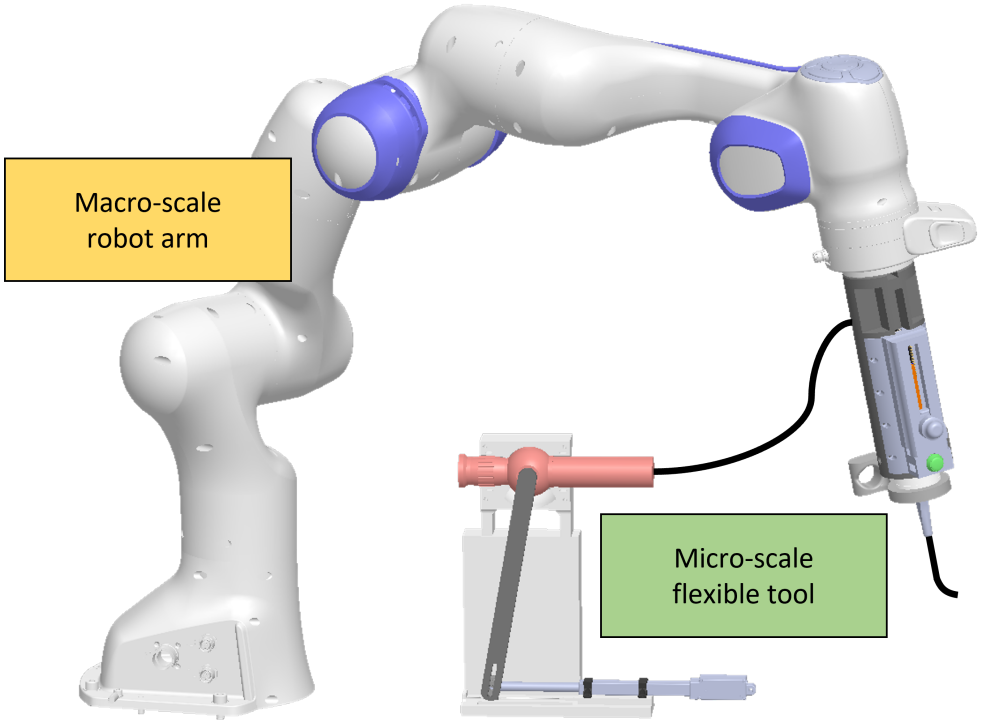

FIGURE 1.17: Our proposed macro/micro scale robotic architecture.

This macro/micro robotic system shows a redundant kinematic structure (9 DOF in total) able to operate in a limited and constrained space like the middle ear cavity. Actually, the total number of DOF has been chosen in order to efficiently control the system end-effector motion while satisfying kinematic constraints at the entrance point of the middle ear [Dahroug et al., 2018b], as mentioned earlier.

1.3.2 Design of the control architectures

As the mechanical and electrical features of the macro/micro robot has been presented above, the next phase is to design the control schemes of each component of the developed system. The macro-scale robot arm can be controlled by comanipulation or teleoperation. In addition, a lab-made 2 DOF joystick was created to control the motion of the corresponding micro-scale part's DOF. Note that, a detailed analysis of control methods are described in the next chapter.

Lab-made joystick

A lab-made 2D joystick was designed to control only the micro-scale part. Thus, it has linear mobile part where is attached a rotational part. This configuration mimics the 2 DOF (translation and rotation) of the micro-scale part.

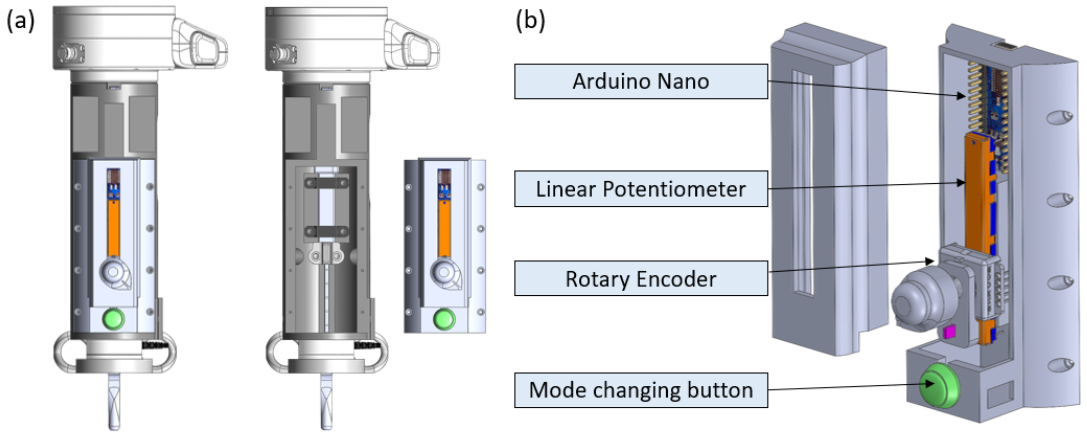

FIGURE 1.18: Lab-made 2 DOF joystick (a) associated with the chassis (b) with embedded components list.

A rotary encoder mounted on a linear potentiometer measures both the desired flexion angle and the desired position of the prismatic joint, respectively. In this work, a BOURNS absolute 128 positions rotary encoder (EAW0J-B24-AE0128L) and an Alps Alpine (RS6011Y1600Q) linear potentiometer are used (as depicted in Figure 1.18).

The measurement of the tension converted in digital value p_v (from 0 to 1023) from the potentiometer is changed into a desired position θ_{td} of the translation. As for the flexion, the desired angle θ_{fd} is obtained from the angle value p_r of the absolute encoder.

$$\theta_{td} = \frac{p_v}{1023} * 50.0 \tag{1.1}$$

$$\theta_{fd} = \frac{p_r}{127} * 360.0 \tag{1.2}$$

The measured desired values of the translation θ_{td} and angle of flexion θ_{fd} are then sent to a server PC to interact with other control functions. Note that, this joystick is mounted on the micro-tool chassis and is structurally aligned with the micro-tool axis thus avoiding any mental registration by the surgeon during the task.

Low-level controller for micro-scale tool

The 2 DOF actuating system of the micro-scale tool is controlled through a low-level position-based controller implemented on an Arduino Mega micro-controller board and Actuonix servomotor. As explained, the translation of the micro-tool is controlled with an integrated encoder inside the servomotor with a resolution of 0.5 mm.

Translation: A simple closed loop control is established to control the translation position of the end-effector. A desired position value θ_{td} is submitted to a min/max controller, the minimal value is set as 0.0 mm and the maximal value as 50.0 mm. It is converted into a position error. A proportional-derivative-integral (PID) controller changes this error into the command of the servomotor. The PID parameters are empirically set to get a reactive and accurate control of the servomotor.

Flexion: The desired flexion angle θ_{fd} has to be converted into the fiberscope's trigger angle θ_{ft} to control the flexion. In order to find this conversion function, the desired flexion angle position every angle value of the trigger was measured for every 10° fiberscope angle from −60° to 90° ("Up" in Figure 1.19) and from 90° to −60° ("Down" in Figure 1.19).

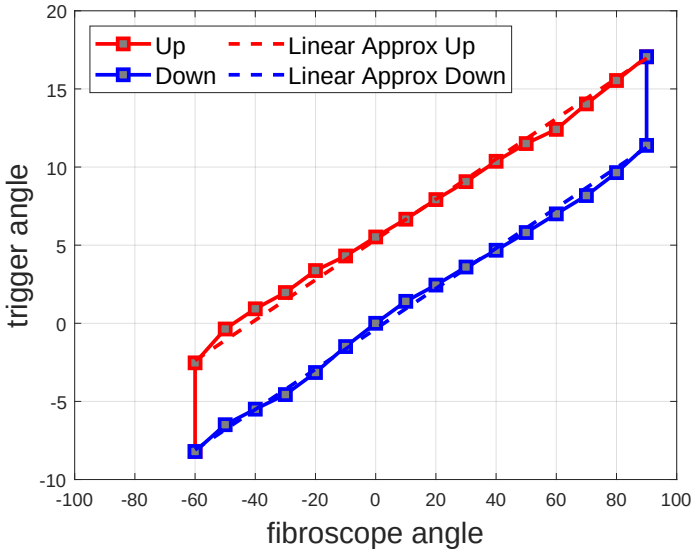

FIGURE 1.19: Flexion angle to Trigger angle.

In Figure 1.19, it can be noticed that the tendon-driven mechanism has hysteresis. Thus, an approximation based on the linear functions was computed, giving:

$$\theta_{ft} = k * \theta_{fd} + 0.0 \quad \text{for} \quad \theta_{fd} : 90^\circ \rightarrow -60^\circ$$
$$\theta_{ft} = k * \theta_{fd} + k_{hyst} \quad \text{for} \quad \theta_{fd} : -60^\circ \rightarrow 90^\circ$$

with the linear function's slope parameter $k = 0.126$ and the hysteresis width $k_{hyst} = 4.5^\circ$.

Same as for the translation, the flexion is submitted into a min/max controller from -60° to 90°. Then, as presented in the mechatronic design part, the flexion is induced by the linear servomotor. Consequently, the trigger angle θ_{ft} has to be changed into a translation value.

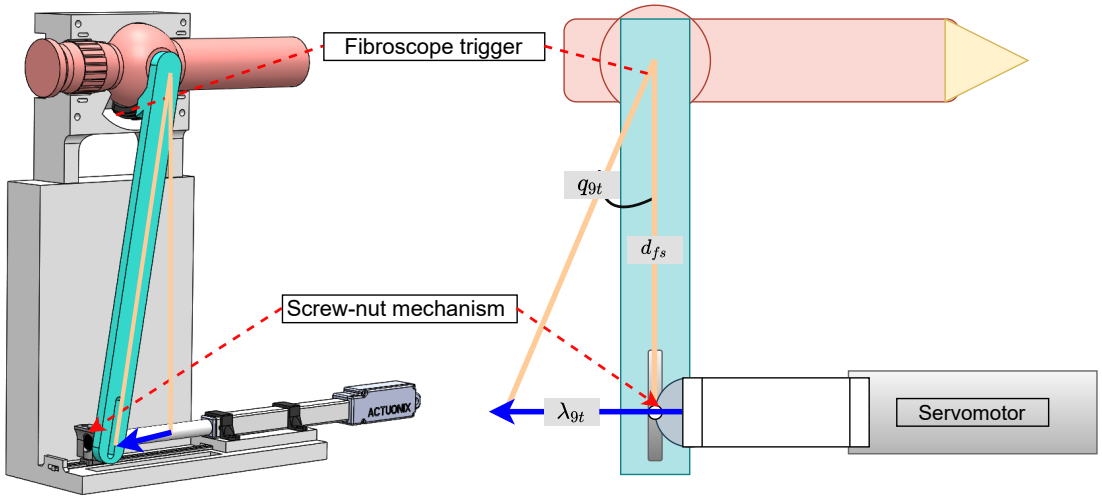

FIGURE 1.20: Scheme explaining the angle of the trigger induced by the translation of the servomotor.

Figure 1.20 shows the mechanism of the trigger angle induced by the translation of the linear servomotor. The mathematical relation of the two variables θ_{ft} and λ_{9t} can be approximated as:

$$\lambda_{9t} = d_{fs} * \tan(\theta_{ft}) \tag{1.3}$$

regarding that $\theta_{ft} \in [-10^\circ, 20^\circ]$ and thus remains relatively small. The desired linear position λ_{9t} is then submitted in a closed control loop, where the position error ϵ_9 is submitted to a PID controller resulting to a command position value λ_{9c} of the servomotor.

As the low-level control of the micro-part was developed, the last phase of control architecture is to implement all the other existing control or measurement functions in a same operating system.

Software design

All the components are implemented on a server PC Ubuntu 16.04 LTS using Robot Operating System[6] (ROS). The control function of the robotic system is under frequency of 100 Hz.

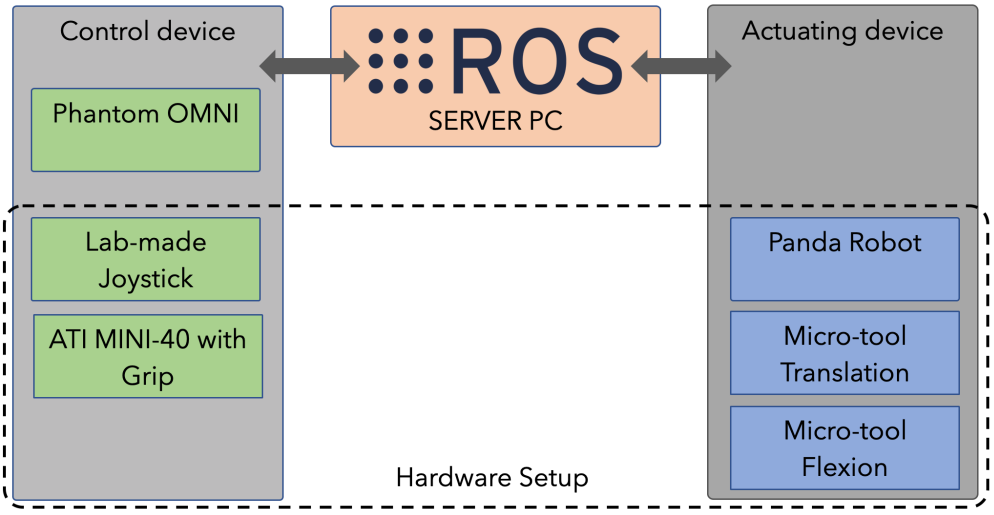

FIGURE 1.21: Software Architecture of the developed macro/micro mani -pulator.

In summary, the developed packages for control device consist of:

- The desired position of the lab-made joystick which lets a teleoperation of the micro-scale tool.
- The measure of the force and torque from the integrated force/torque (F/T) sensor between the macro-robot end-effector and the micro-scale tool so that the macro-robot terminal body can be handled by the user in a comanipulation manner.
- The 6 DOF joystick Sensable Phantom Omni which lets the human operator perform an end-frame teleoperation of both the macro-scale part only or the full macro/micro system.

1.4 Conclusion

We developed a macro/micro system dedicated for the cholesteatoma resection and by extension, for middle ear surgery. The first part of this chapter started by presenting the anatomy of the middle ear, the definition of the cholesteatoma and the current treatment, *i.e.*, the cholesteatoma resection surgery involving conventional rigid surgical tools. The

[6] https://www.ros.org/

problems of such intervention are its invasiveness, the limited sight for the surgeon and the persistent problem of residual cholesteatoma which causes, in 20% to 30% of the cases, a second look-up. To tackle the listed problems, a review of existing middle ear surgical robot and other benchmarkable robotic systems that fits in the requirement of the cholesteatoma resection has been made.

Then a new robotic solution has been proposed in Section 1.3. It consists of a macro-scale robotic arm and a new designed flexible micro-scale surgical tool where a surgical laser can be embedded on. The mechatronic design and the software architecture are both treated, explaining precisely how this novel robotic device was created.

The combined robotic device gives a number of DOF superior to six (in total 9 DOF), which creates redundancy. Controlling the movement of a redundant system is a complex task, due to its diverse angular configurations for a desired position of the end-effector (*i.e.*. the internal motion). This versatility can disturb a surgeon during and consequently, an intuitive control interface must be developed to ensure a precise control of the system and an optimal ergonomic.

Another point is that the robotic arm (macro-part) remains entirely outside of the body during the intervention and the end-effecting part of the latter has to follow the RCM constraint [Su et al., 2018, Dahroug et al., 2020b] to avoid collision and tissue damage. That is why, the next Chapter will be devoted on creating a control strategy in order to handle the redundancy problem and to ensure a sufficient precision of the designed system.

Chapter 2

User Integrated Control Techniques for Robotized Middle Ear Surgery

Contents

The previous chapter described the development of the robotic system targeted for a middle ear surgery. Hence, the next step is to develop a control method which can help users to easily manipulate the system during the surgical intervention. This chapter starts by enlisting the existing control strategies in terms of teleoperation or comanipulation methods in Section 2.1. These control methods being fundamental in control theory, a detailed research is necessary to propose an adapted control solution for the developed system. Then, a kinematic modeling of the robotic system is presented in Section 2.2, as

an essential requirements to implement any control law. An additional part is dedicated to the integration of the kinematic modeling under a spatial constraint, *i.e.*, RCM, in order to achieve accurate positioning tasks in a limited environment. Section 2.3 shows two designed controllers ensuring the control of the macro/micro system via:

- an end-frame teleoperation of the whole kinematic structure with an intuitive and transparent management of the fulcrum effect resulting from the RCM;
- a combination of a comanipulation method for the macro-scale robot and an in-hand teleoperation for the micro-scale tool.

In Section 2.4, both control schemes are evaluated individually and compared through a scenario that mimics the task of pointing out residual cholesteatoma cells with a surgical laser.

2.1 Overview of existing control strategies

This section presents existing control methods for surgical robots. Also, this section gives the benefit and the drawback of enlisted control strategies to find out an adapted method for the developed system. Note that each control method can also be coupled with diverse control devices, *e.g.*, joystick, sensors. Thus, the weaknesses due to control devices, are also presented.

2.1.1 Teleoperation

Teleoperation is the operation of a machine, system or robot from a distance via a control interface. First systems integrating teleoperation control began in the 50's by Goertz [Goertz, 1949, Goertz and Thompson, 1954] in order to manipulate radioactive material. The development of such a control method came from the need to achieve a complex task in a hostile, space-constrained environment where the human operator cannot be physically present. Thus, the benefit of teleoperation is to extend the human capacity for manipulating objects by providing similar conditions as those encountered in the remote workspace [Sheridan, 1995], and to also increase handling precision. Later, teleoperation became a widely used control technique in surgical robotics (mainly in minimally invasive surgery) with the development of Zeus [Marescaux and Rubino, 2003] and Da Vinci robots [Guthart and Salisbury, 2000]. This control method helps the surgeon to manipulate parts of organ and to manoeuvre complex tasks in a closed environment. Therefore, it contributes to an increase of the precision during surgical intervention, *e.g.,* by scaling the motion of the operator sent to the robot [Moorthy

et al., 2004, Prasad et al., 2004]. In many cases, it also contributes to faster post-operative recovery of the patient[Fuchs, 2002].

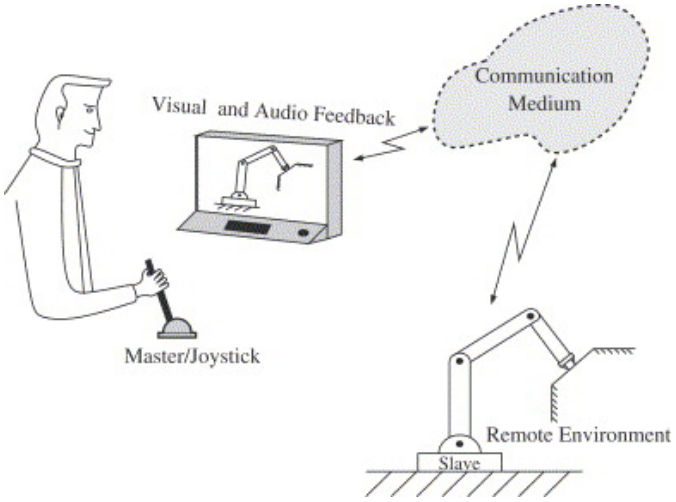

FIGURE 2.1: Scheme representing an unilateral teleoperation [Hokayem and Spong, 2006].

The first teleoperation was achieved only with visual and/or audio feedbacks [Lichiardopol, 2007] (as depicted in Figure 2.1). Thus, it is called unilateral control in which the control scheme reduces to a coupling between master and slave arms positions. The human operator sends a desired position x_m information throughout a communication access and the following robot tends to the received desired position (*i.e.*, upper position control part of Figure 2.2).

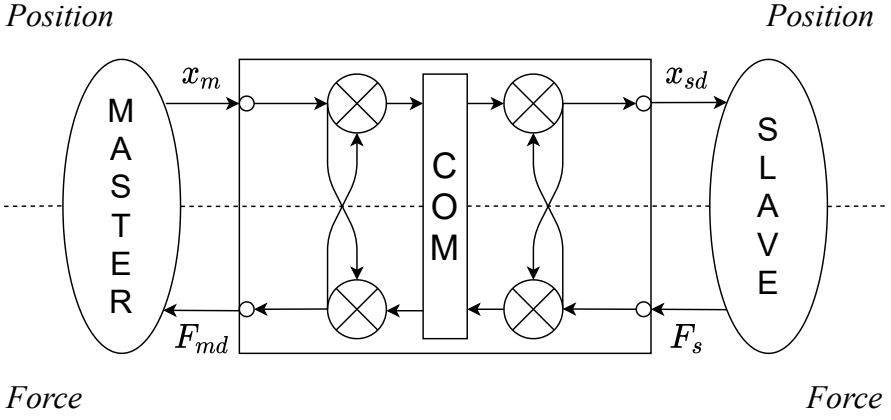

FIGURE 2.2: Scheme representing the unilateral (only upper part of the scheme) and bilateral (full scheme) teleoperation.

However, in a case where the manipulation is performed in a fragile or deformable environment, the unilateral control does not always provide necessary information to manipulate safely. Indeed, the operator may need other feedbacks, for example when the visual and audio feedbacks are not enough to avoid collision of the controlled unit with the environment. A possible solution is then to fuse an another type of information in the

control loop. For example, force feedback gives a better and more realistic perception of the interaction between the slave robot and the environment. It leads to bilateral control, meaning that the operator sends a position command (x_m) to the following system via a control device [Anderson and Spong, 1988, Hokayem and Spong, 2006] and this system returns back a reaction force (F_s) measured via a force sensor to the operator (Figure 2.2).

In this work, due to the narrowness of the micro-tool, the integration of a force sensor at the tool-level is impossible. As the micro-tool would bend with external or contact force, the force sensor would give a poorly exploitable measurement. Only the unilateral control (position-position) was then considered to develop our end-frame tele-manipulation scheme.

Teleoperation is a wide field of study, it can be categorized with different parameters such as the field of application, the number of controllable points, advanced point in control theory (*e.g.,* stability, precision or redundancy), the number of robot controlled simultaneously [Mehrdad et al., 2021] etc... . In the following, we present different classes of teleoperation approaches according to the kind of implemented mapping between master and slave spaces.

End-frame teleoperation

The end-frame teleoperation is the best known teleoperation type in the literature [Simorov et al., 2012]. This control technique is to command the position of the end-effector of a robotic system using its kinematic properties and a direct mapping between master and slave end-frames. In the surgical context, the operator has to control the functional part of a surgical tool (*e.g.*, clamp of a forcep), this functional part being located at the distal end of the slave robot. Thus, if a robotic system integrating surgical tools is controlled under teleoperation strategy, it is logical to implement, an end-frame teleoperation. Following paragraphs detail some examples of robotic systems using end-frame teleoperation applicable to the developed robotic system.

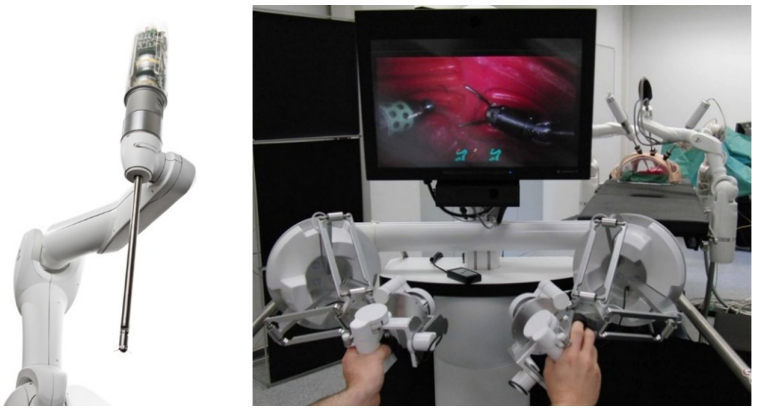

FIGURE 2.3: 7 DOF MiroSurge robot and its 6 DOF joystick [Tobergte et al., 2011].

The MiroSurge robotic system [Simorov et al., 2012] is a teleoperated robotics system used in laparoscopic surgery. Its back-drivability lets the user move freely the robotic arm if the robot configuration disturbs the workspace of the additional surgeons who are working close to the patient and the system. The teleoperation interface is similar to the Da Vinci robot, it provides a visual feedback from the endoscope and a 6 DOF joystick controlling the position [Tobergte et al., 2011] of a 7 DOF robot's end-effector (as depicted in Figure 2.3). An additional haptic feedback has been added to the joystick, bringing to the user a better comprehension of the workspace and enhancing the precision of the surgical tasks.

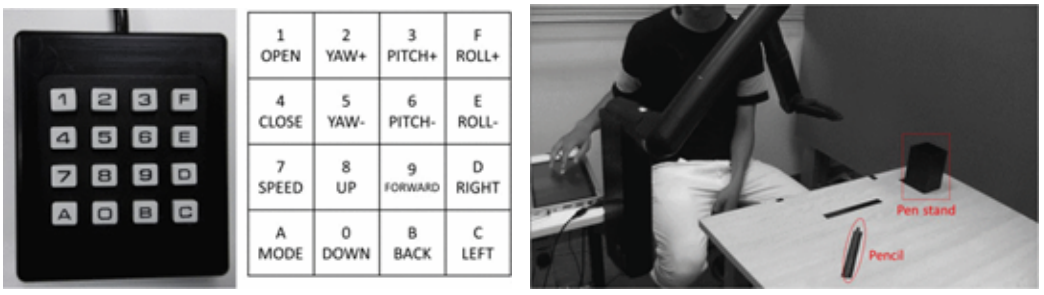

(A) Control pad (B) Robotic setup

FIGURE 2.4: The touch pad with all possible movement [Oka and Matsushima, 2016].

Another example of end-frame teleoperation is the voice and multi-touch command [Oka and Matsushima, 2016]. The aim of this prototype system is to make the manipulation easy and intuitive. A 16-button pad (Figure 2.4A) can control the speed and different orientation/position of the end effector. The voice command allows to select between three modes of end-effector control; the 3 modes include the horizontal and vertical translation and the orientation switching mode. However, this kind of control is exhausting for the user who has to constantly project and interprete the end-effector's position in 3-D space.

The end-frame teleoperation mode is a solution giving an easy and intuitive control for a teleoperated robot. Besides, it allows implementing a scale factor between master and follower spaces for increasing the motion accuracy. Also, different kinds of mapping between the coordinates in these two spaces are possible (*e.g.*, position-position, position-velocity, etc). However, for robotic systems having more than 6 DOF like the macro/micro system we developed in Chapter 1, the control is more difficult due to the high number of joints and the fact that multiple joint configurations are possible for a same end-frame position (*i.e.*, the internal motion). This leads to an uncontrolled joint configuration which can cause safety issue *e.g.*, collisions with the environment. To tackle this issue, additional functions which automatically handle the internal motion (*e.g.*, collision detecting function, controllable internal motion) have to be developed.

Two frames teleoperation

One solution to resolve the internal motion issue, mentioned just before, is to control two frames instead of the sole end-effecting frame. Controlling two frames is analogical to do end-frame teleoperation on two systems linked in a serial configuration. Thus, it gives additional manoeuvrability for redundant robotic structures. In case of a macro/micro system, one end-frame teleoperation can be devoted to the control of the distal part of the macro-system and another can be applied to the micro-system.

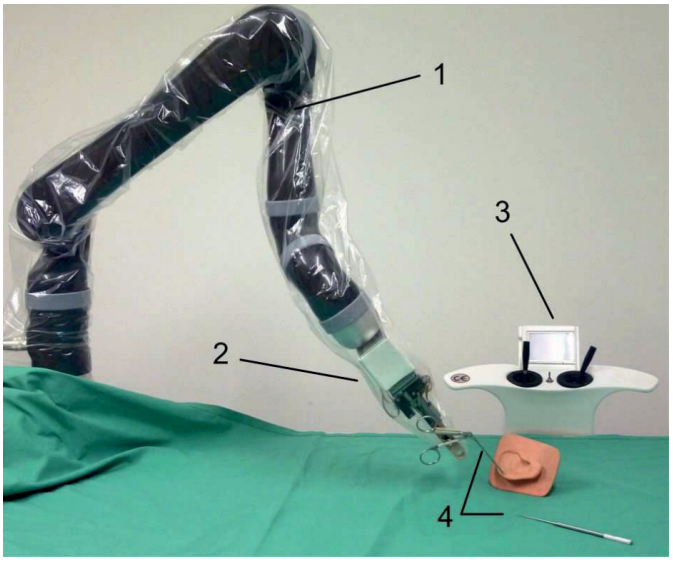

FIGURE 2.5: 10 DOF MMTS for microsurgery system [Entsfellner et al., 2012].

The Macro-Micro Telemanipulation System (MMTS) [Entsfellner et al., 2012] is quite similar to our developed macro/micro system. It is controlled by 2 joysticks, one for a 6 DOF robotic arm and another for a 4 DOF micro manipulator attached at the distal part of the robot arm (as depicted in Figure 2.5). However, as the joystick gives only a

planar control profile, the surgeon has to change the control plane with a touch screen ($x-y$, $y-z$ or $z-x$). To do that, the operator has to mentally project the tool-tip position in the 3-D space in order to choose which plane to control. This can lead to a high level of concentration burden and therefore a higher level of fatigue accumulated during the surgery.

Joint to joint control

A second alternative solution to the internal motion issue is the joint to joint control. A simple and intuitive joint to joint control of teleoperation is to have a master device which has the same joint structure as the slave device [Heunis et al., 2012]. Using encoders to assess the angular positions of each joint at master level one obtains the desired joint positions at the slave level.

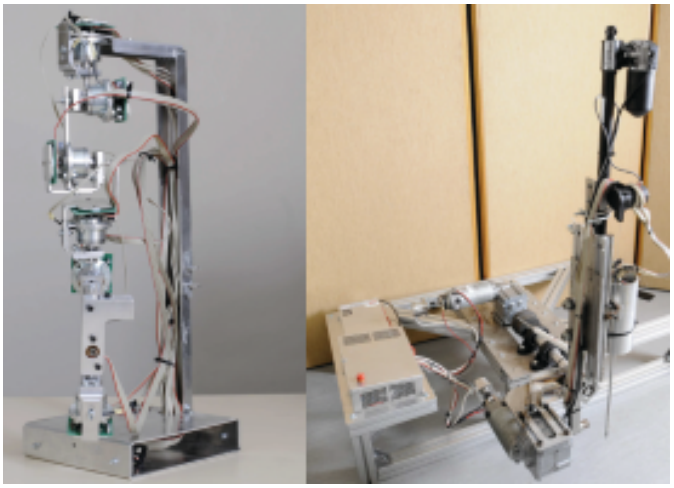

FIGURE 2.6: Master and Slave 7 DOF robots [Heunis et al., 2012].

Another example of joint to joint control is the inertial motion capture. It is a method proposed in [Kobayashi et al., 2013], to control a redundant robot with a combination of three inertial measurement units (IMU). This way, one can control a manipulator by measuring the joint positions of the hand, the forearm and the upper arm of the user (Figure 2.7). The set of 9 returned IMU orientations must be simplified to control the 6 DOF robot arm with an additional gripper. Note that force feedback cannot be implemented within this framework.

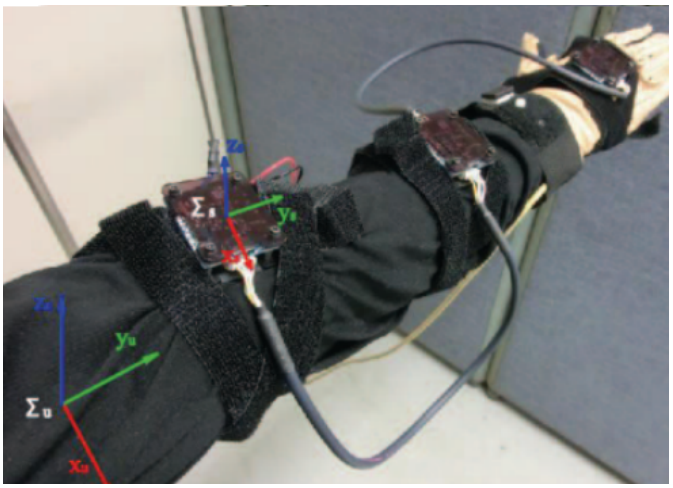

FIGURE 2.7: Motion capture control using IMU [Kobayashi et al., 2013].

Among the different teleoperation techniques, the joint to joint control is the simplest (at software level) to integrate in a redundant system. However, it has some limits since the operator has to control each joint one by one, causing a large amount of concentration to the user. More anthropomorphic master devices exist but at the expense of more technological complexity *i.e.*, using multiple sensoring sources to track the joint position [Du et al., 2014, Fang et al., 2017], thus decreasing the ease of software integration mentioned just before.

2.1.2 Comanipulation

Focusing on the surgical context, teleoperation can be a good choice to control a MIS-oriented robot. However, a distance gap between the surgeon and the patient can incite psychological effect on the surgeon who feels that he/she is not fully managing the operation [Morel et al., 2013]. To decrease this feeling of doubt, the solution is to let surgeon next to the patient and the robot.A possible approach to that is comanipulation. Comanipulation is a control method which consists in moving a robotic system or a surgical instrument with the operator's direct interaction. Two categories of comanipulation for robot's distal part can be defined as:

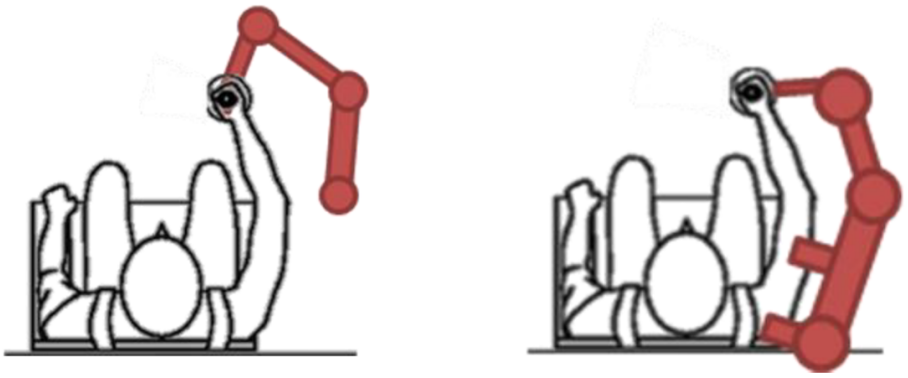

(A) Parallel comanipulation (B) Orthotic comanipulation

FIGURE 2.8: Types of comanipulation controlling the distal part of a robotic system [Morel et al., 2013].

- **Parallel comanipulation:** The robotic system is fixed on a base while its distal part is guided by the operator's hand (Figure 2.8A). As for the instrument, its proximal part is connected to two parallel kinematic chains, *i.e.*, the arm of the user and the robot, the distal part being in contact with the environment.
- **Orthotic comanipulation:** It is the same principle as the parallel comanipulation but with multiple attachment points between the user and the robotic system (Figure 2.8B). Most orthotic comanipulators are designed to follow the human motion. Thus, an orthotic system has an anthropomorphic design, *i.e.*, same geometrical and kinematical properties as human limb, *e.g.*, an exoskeleton.

From a hardware point of view, the displacement compatibility between the human operator and the robotic system is made possible by two techniques. First is the reversibility of the mechanical system, *i.e.*, the joint configuration of the mechanical system can be changed only by applying a direct external effort. Second is to convert the applied force on a F/T sensor into a desired displacement velocity. In the following, comanipulation modes are categorised into two types depending on the applied force location and on the number of controlled joints.

Parallel comanipulation

In parallel comanipulation, the human operator controls the end-effecting part while the robot base is fixed. An example of a surgical robot using the parallel comanipulation is the ROSA® system from Zimmer Biomet. It allows motion control using a force-torque (F/T) sensor placed between the robot end-effector and the tool (Figure 2.9). This control allows a precise positioning of the tool in the pre-operatory stage before the knee

FIGURE 2.9: ROSA® surgical system.

replacement surgery. Plus, the surgery itself can also be operated in comanipulation if the registration of the surgical site is pre-defined.

Multi-frame comanipulation (Orthotic comanipulation)

The multi-frame comanipulation is a manipulation where multiple joints can be controlled at the same time in a comanipulation manner. In this case, there are multiple interaction points between the robot and the user. It can be an exoskeleton-like robot attached to an operator and following the human motion.

In Germany, an exoskeleton like robot has been developed for orthopedic surgery [Hessinger et al., 2015]. Depicted in Figure 2.10A, the system is attached to the user's arm from the shoulder to wrist, the entire system is carried on a base. Optical markers are attached on the end-effector and the spinal bones. An optical tracking system computes the positions of these parts. Consequently, the exoskeleton lets the user move the tool freely and also blocks the motion when necessary (*e.g.*, wrong position of the tool, dangerous motion of the user), relaying on the information pulled from the visual tracking algorithm. The benefit of this system is the transparency of the robot, following exactly the operator's movements. Thus, the internal motion control of this structure is intuitively achieved.

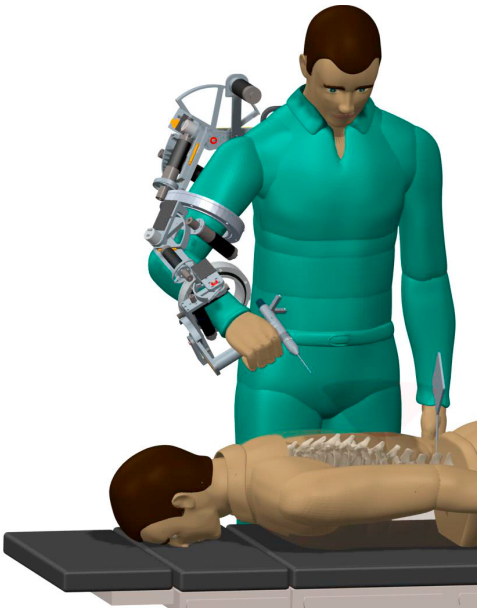

(A) SMART exoskeleton for spine surgery [Hessinger et al., 2015].

(B) RIO robotic arm [Hagag et al., 2011].

FIGURE 2.10: Examples of multi-frame comanipulation.

Another multi-frame comanipulation is MAKOplasty's RIO robot (Figure 2.10B). It is a 6 DOF robot for orthopedic surgeries such as knee arthroplasty [Hagag et al., 2011]. A control handle at the elbow joint gives a wide range control of the robot used for positioning the tool near the surgical area. Another control handle on the tool facilitates the control of the surgical motion. The comanipulation is particularly efficient in this case where the surgeon has to check and validate necessary positions before operating. For that, the surgeon has just to position the end-effector on the required area and save its spatial coordinates.

To finish on comanipulated tools, in [Zhan et al., 2015], multiple robotic systems integrating comanipulation are enlisted. It shows that using comanipulation control can be a good solution to control an assistive robot during the surgery. Depending on the robot programming, comanipulation can reduce tremor and increase the accuracy and precision. Plus, the direct interaction between the operator and the robot makes its use more intuitive than teleoperation and therefore, it is better accepted from surgeons [Morel et al., 2013].

Control Methods	Difficulty of development	Ergonomic	Intuitiveness	Manipulability
End-frame Teleoperation	-	++	-	++
Two-frames Teleoperation	+	+	-	-
Joint to joint Teleoperation	++	-	+	–
End-frame Comanipulation	-	+	++	++
Multi-frame Comanipulation	+	-	+	+

TABLE 2.1: Qualitative comparison of presented control methods

Table 2.1 sums up all the specificities of the control strategies described in this section. In this table, the difficulty of implementation (*i.e.*, hardware and software development), intuitiveness, ergonomy and manipulability (*i.e.*, ease of control) are treated as qualitative variables for comparison. These variables reflect the main objectives of this work, as mentionned in Chapter 1. The targeted system must be easily integrated in different robotic platform and has to be user-friendly in three points; the user does not need a long time to get used to control the developed device, he does not need a high level of concentration on controlling the robot and last, the robot has to be sufficiently transparent to the user's intention.

Among the listed two control methods (*i.e.*, teleoperation and comanipulation methods) the benefits and drawbacks with respect to robotic-assisted surgery are pretty clear: the comanipulation gives an intuitive control of the robot in the external environment (*i.e.*, external from the patient), the teleoperation gives an accurate tool handling in the internal environment (internal human cavity, *e.g.*, the abdominal cavity for laparoscopic surgery or middle ear cavity for ear surgery). Besides, defferences in terms of speed/accuracy tradeoff can also be highlighted in [Gijbels et al., 2014], where a comparative study of both control methods is presented. This study shows that the comanipulation tool approach tends to be faster than teleoperation, but with lower precision than teleoperation in which mapping scale factor can be implemented. One interesting point is that teleoperation takes in up to 2 times more time than comanipulation, including the integration time (adaptation of the user to manipulate). To conclude, comanipulation tends to be more intuitive and teleoperation tends to be more precise.

Based on this, we decided to explore both comanipulation and teleoperation to find a solution that is adapted to control the developed robotic system and that meets the requirement of the cholesteatoma resection surgery. However, supplementary information *e.g.*, the geometrical and the kinematic models of the system, is necessary to implement the two options.

2.2 Kinematic modeling of the robotic system

The following section describes the kinematic modeling of our 9 DOF robot which will be used for the integration of control method (presented in later Section 2.3).

2.2.1 Mapping between joint-space and task-space

First, we derive the forward kinematic model establishing a mathematical relation between the robotic system joint variables and the end-effector frame configuration with respect to the robot base frame $\mathcal{R}_0$, as depicted in Figure 2.11. This model can be split

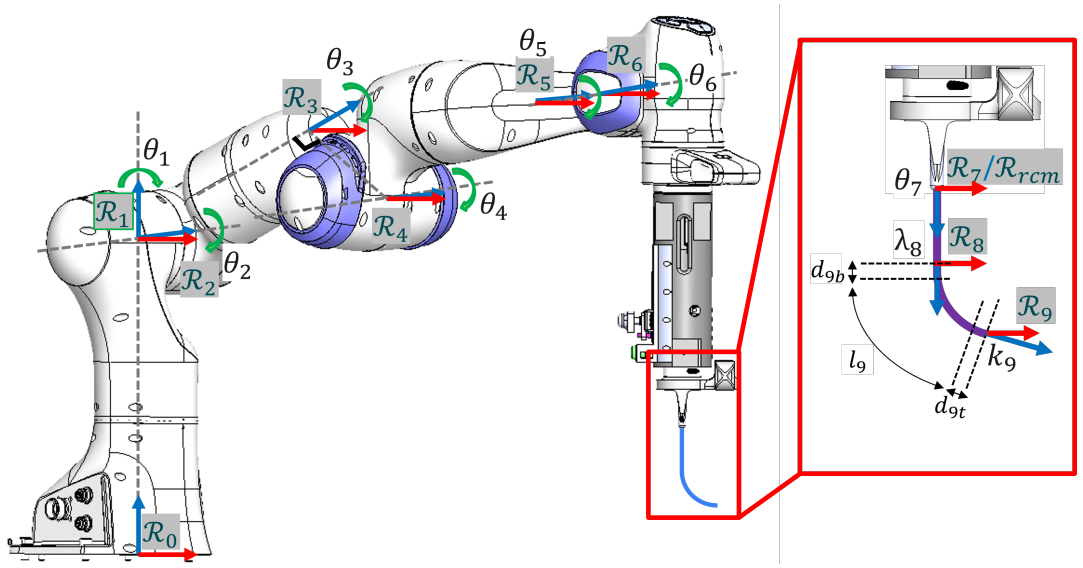

FIGURE 2.11: Kinematic diagram of the whole robotic system.

in two parts corresponding to macro-scale and micro-scale subsystems. Each sub-model is identified through a transformation matrix linking the last and the first frames of the corresponding chain.

Joint N°	a_i(m)	d_i(m)	α_i(rad)	θ_i (rad)
1	0	0.333	0	θ_1
2	0	0	-π / 2	θ_2
3	0	0.316	π / 2	θ_3
4	0.0825	0	π / 2	θ_4
5	-0.0825	0.384	-π / 2	θ_5
6	0	0	π / 2	θ_6
7	0.088	0.259	π / 2	θ_7

TABLE 2.2: Modified Denavit-Hartenberg parameters of the macro-scale part[1].

Actually, the mapping between the macro-scale subsystem joint values and its operational configuration ($\mathcal{R}_7$) is obtained via a set of transformation matrices ${}^{i}\mathbf{T}_{j}$ based on the modified Denavit-Hartenberg (D-H) parameters (from Table 2.2) which are expressed as follows:

$$ {}^{i-1}\mathbf{T}_{i} = \begin{bmatrix} c_{\theta_i} & -s_{\theta_i} & 0 & a_{i-1} \\ s_{\theta_i} c_{\alpha_{i-1}} & c_{\theta_i} c_{\alpha_{i-1}} & -s_{a_{i-1}} & -d_i s_{a_{i-1}} \\ -s_{\theta_i} s_{\alpha_{i-1}} & c_{\theta_i} s_{\alpha_{i-1}} & c_{a_{i-1}} & d_i c_{a_{i-1}} \\ 0 & 0 & 0 & 1 \end{bmatrix} \tag{2.1} $$

[1]The Denavit-Hartenberg parameters can be found at https://frankaemika.github.io/docs/control_parameters.html.

where $i \in \{1, 2, \cdots, 7\}$ is the index of the i-th actuator , $s_{\theta_i} = \sin(\theta_i), c_{\theta_i} = \cos(\theta_i)$, and d_i, a_i, θ_i, α_i are the modified D-H parameters as shown in Figure 2.11. Logically, the kinematic model of the macro-scale system is obtained as follows:

$$ {}^{0}\mathbf{T}_7 = {}^{0}\mathbf{T}_1 {}^{1}\mathbf{T}_2 {}^{2}\mathbf{T}_3 {}^{3}\mathbf{T}_4 {}^{4}\mathbf{T}_5 {}^{5}\mathbf{T}_6 {}^{6}\mathbf{T}_7 \tag{2.2} $$

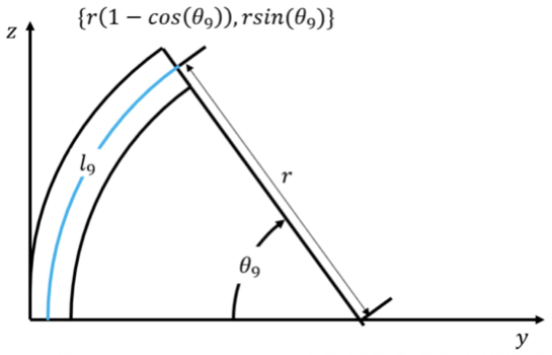

FIGURE 2.12: Kinematic diagram of the flexible part.

Concerning the micro-tool part, the first actuated motion is a translation. The distance between $\mathcal{R}_7$ and $\mathcal{R}_8$ along the z_7 axis varies with the distance λ_8. This leads to a transformation matrix ${}^{7}\mathbf{T}_8$ expressed as follows:

$$ {}^{7}\mathbf{T}_8 = \begin{bmatrix} 1 & 0 & 0 & 0 \\ 0 & 1 & 0 & 0 \\ 0 & 0 & 1 & \lambda_8 \\ 0 & 0 & 0 & 1 \end{bmatrix} \tag{2.3} $$

The second actuation is a flexion of the tool-tip. For parts, we apply the constant curvature model, often used in the literature [Webster III and Jones, 2010, Robert J. Webster and Jones, 2010, Ott et al., 2011]. Figure 2.12 shows the modelling of the flexible tool using the constant curvature model.

The fiberscope terminal body is divided in three parts, as shown in Figure 2.11:

1. A rigid part d_{9b}
2. A flexible bending mechanism with length l_9
3. Another rigid part at the tool-tip d_{9t}

According to Figure 2.12 and the flexion model presented in Section 1.3, the flexion position can be computed as $y = r * (1 - \cos(\theta_9))$ and $z = r * \sin(\theta_9)$ where $r = l_9/\theta_9$ is the radius of the arc made by the flexion and θ_9 the angular position. This leads to the following expression:

$$\begin{pmatrix} x_9 \\ y_9 \\ z_9 \end{pmatrix} = \begin{cases} \begin{pmatrix} 0 \\ \frac{l_9}{\theta_9}\Big(1-\cos(\theta_9)\Big) \\ \frac{l_9}{\theta_9}\Big(\sin(\theta_9)\Big) \end{pmatrix} & \text{for} \quad \theta_9 \neq 0 \\ \begin{pmatrix} 0 \\ 0 \\ l_9 \end{pmatrix} & \text{for} \quad \theta_9 = 0 \end{cases} \tag{2.4}$$

In the literature, the flexion angle θ_9 is commonly represented as curvature parameter k, that is why, we define a new joint variable k_9 giving the relation between z_8 and z_9 as $k_9 = \frac{\theta_9}{l_9}$. Thus, the transformation matrix ${}^8\mathbf{T}_9$ function of the new variable k_9 is expressed as:

$${}^8\mathbf{T}_9 = \begin{cases} \begin{bmatrix} 1 & 0 & 0 & 0 \\ 0 & c(k_9 l_9) & -s(k_9 l_9) & d_{9t}\ s(k_9 l_9) - (1 - c(k_9 l_9))/k_9 \\ 0 & s(k_9 l_9) & c(k_9 l_9) & d_{9b} + d_{9t}\ c(k_9 l_9) + s(k_9 l_9)/k_9 \\ 0 & 0 & 0 & 1 \end{bmatrix} & \text{for} \quad \theta_9 \neq 0 \\ \begin{bmatrix} 1 & 0 & 0 & 0 \\ 0 & 1 & 0 & 0 \\ 0 & 0 & 1 & d_{9b} + d_{9t} + l_9 \\ 0 & 0 & 0 & 1 \end{bmatrix} & \text{for} \quad \theta_9 = 0 \end{cases} \tag{2.5}$$

As a result, the total transformation matrix from $\mathcal{R}_0$ to $\mathcal{R}_9$ is obtained by the product of equations (2.2), (2.3) and (2.5) giving the following expression:

$${}^0\mathbf{T}_9 = {}^0\mathbf{T}_7\,{}^7\mathbf{T}_8\,{}^8\mathbf{T}_9 = \begin{bmatrix} {}^0\mathbf{R}_9 & {}^0\mathbf{t}_9 \\ 0 & 1 \end{bmatrix} \tag{2.6}$$

Here, ${}^0\mathbf{R}_9 \in \mathbb{R}^{3\times3}$ and ${}^0\mathbf{t}_9 \in \mathbb{R}^{1\times3}$ are respectively the rotation matrix and translation vector of the tool-tip frame $\mathcal{R}_9$ with respect to the base frame $\mathcal{R}_0$.

The velocity-level kinematic mapping between the joint configuration space and the task space can be obtained by:

$${}^0\dot{\mathbf{x}} = \mathbf{J}\ \dot{\mathbf{q}} \tag{2.7}$$

where ${}^0\dot{\mathbf{x}} = [{}^0\mathbf{v}^\intercal, {}^0\omega^\intercal]^\intercal \in \mathbb{R}^6$ represents the linear (${}^0\mathbf{v}^\intercal$) and angular (${}^0\omega^\intercal$) velocities of the tool-tip with respect to the base frame $\mathcal{R}_0$, $\dot{\mathbf{q}} = [\dot{\theta}_1, \dot{\theta}_2, \cdots, \dot{\theta}_7, \dot{\lambda}_8, \dot{k}_9]^\intercal \in \mathbb{R}^9$ is the joint-velocity vector; and $\mathbf{J} \in \mathbb{R}^{6\times9}$ is the robot Jacobian matrix which can be calculated using (2.6). Derivation of the Jacobian matrix $\mathbf{J}$ is described in the Appendix A.1

2.2.2 Remote center of motion simplification

The surgical protocol devoted to middle ear interventions as mentioned in [Dahroug et al., 2018b] induces an insertion hole defined as a RCM separating the external environment from the internal one. This narrow access point imposes the quite bulky macro-system effector to remain outside and only allows the thin micro-tool to enter inside the middle ear cavity. Besides lateral motions of the micro-tool at this access point are utterly restricted.

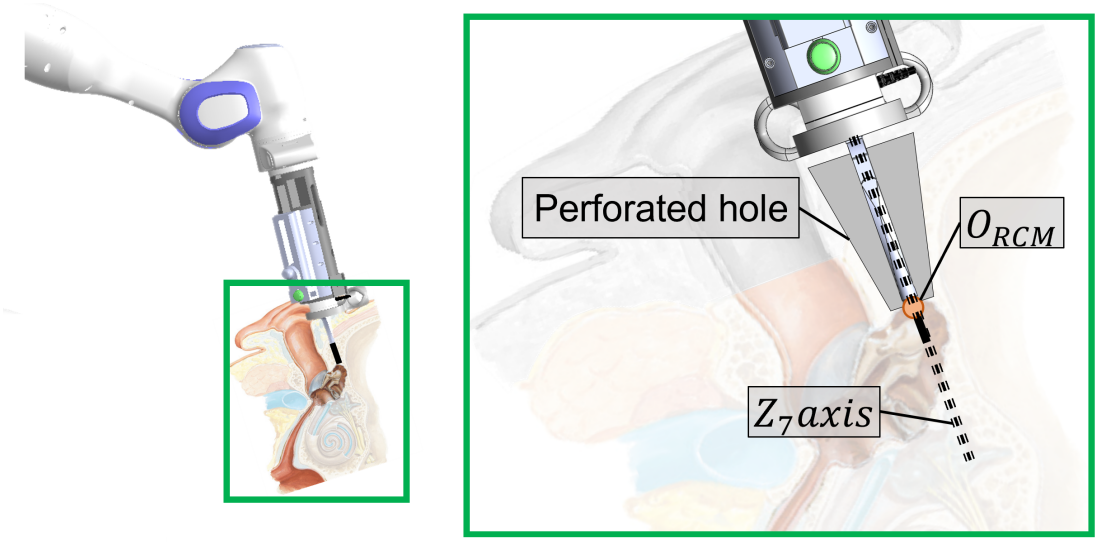

FIGURE 2.13: Scheme representing the robot position under RCM constraint.

From a kinematic point of view, a RCM is imposed to the robot at this access hole to the middle ear (Figure 2.13). Concretely, a point O_{RCM}, located on the Z_7 axis where the flexible fiberscope emerges from the chassis, is imposed to coincide with this insertion point and to be motionless. This specific configuration has the same kinematic property as an insertion point in laparoscopy, for example. It is called here virtual RCM.

Considering the kinematic constraints induced by this virtual RCM, the fiberscope end-frame configuration can be now uniquely controlled by the three rotations of the Panda's end-effector around this point and by the two DOF of the micro-tool. Consequently, we defined a reduced set of joint variables including the $\mathcal{R}_7$ Roll-Pitch-Yaw (RPY) angles (α, β, γ) with respect to $\mathcal{R}_{rcm}$ plus the micro-tool motions λ_8 and k_9. The corresponding simplified kinematic model is expressed thanks to the transformation ${}^{rcm}\mathbf{T}_7$ defined by:

$$ {}^{rcm}\mathbf{T}_7 = \begin{bmatrix} c_\beta c_\gamma & c_\gamma s_\alpha s_\beta - c_\alpha s_\gamma & s_\alpha s_\gamma + c_\alpha c_\gamma s_\beta & 0 \\ c_\beta s_\gamma & c_\alpha c_\gamma + s_\alpha s_\beta s_\gamma & c_\alpha s_\beta s_\gamma - c_\gamma s_\alpha & 0 \\ -s_\beta & c_\beta s_\alpha & c_\alpha c_\beta & 0 \\ 0 & 0 & 0 & 1 \end{bmatrix} \tag{2.8} $$

where α, β and γ are the three rotations at the RCM, and $s_i = \sin(i)$, $c_i = \cos(i)$. Finally, the transformation matrix from $\mathcal{R}_{rcm}$ to $\mathcal{R}_9$ is thus:

$$ {}^{rcm}\mathbf{T}_9 = {}^{rcm}\mathbf{T}_7 {}^{7}\mathbf{T}_8 {}^{8}\mathbf{T}_9 = \begin{bmatrix} {}^{rcm}\mathbf{R}_9 & {}^{rcm}\mathbf{t}_9 \\ 0 & 1 \end{bmatrix} \tag{2.9} $$

with ${}^{rcm}\mathbf{R}_9 \in \mathbb{R}^{3\times3}$ and ${}^{rcm}\mathbf{t}_9 \in \mathbb{R}^3$ are respectively the rotation matrix and translation vector of the tool-tip frame $\mathcal{R}_9$ according to the fixed RCM frame $\mathcal{R}_{rcm}$. Thereby, the velocity-level kinematic mapping between the joint space and the task space can be obtained by:

$$ {}^{rcm}\dot{\mathbf{x}} = \mathbf{J}^* \, \dot{\mathbf{q}}^* \tag{2.10} $$

with $\dot{\mathbf{q}}^* = [\dot{\alpha}, \dot{\beta}, \dot{\gamma}, \dot{\lambda_8}, \dot{k}_9]^\intercal$, the joint space velocity vector and ${}^{rcm}\dot{\mathbf{x}} \in \mathbb{R}^6$, the task space velocity vector of the micro-scale part expressed in $\mathcal{R}_{rcm}$, and $\mathbf{J}^* \in \mathbb{R}^{6\times5}$ the Jacobian matrix of the simplified model.

As the origins of $\mathcal{R}_7$ and $\mathcal{R}_{rcm}$ always coincide, the operational velocity vector of the macro-scale robot can be expressed as ${}^{rcm}\dot{\mathbf{x}}_7 = [0_{3\times1}, \dot{\alpha}, \dot{\beta}, \dot{\gamma}]^\intercal$. Also, the mapping between the macro-scale robot joint and task spaces is formulated as:

$$ {}^{rcm}\dot{\mathbf{x}}_7 = \mathbf{J}_7 \, \dot{\mathbf{q}}_7 \tag{2.11} $$

with $\dot{\mathbf{q}}_7 = [\dot{\theta}_1, \dot{\theta}_2, \cdots, \dot{\theta}_7]^\intercal$ the joint-space velocity vectors and $\mathbf{J}_7 \in \mathbb{R}^{6\times7}$, the Jacobian matrix for the motion of the macro-scale robot constrained by at the RCM point. Thanks to this simplified two-part kinematic model, the computation process of the differential kinematics of the 9 DOF system constrained by the access point will be much easier than using the global 9 DOF differential relation computed via the equation 2.7. Besides, thanks to this simplfication, there is no need, for controlling the system internal motion, to resort to any complex task-priority based control involving the 9 joint-space variables and the orthogonal projection matrix in the null space of $\mathbf{J}$ [Siciliano et al., 2008].

The formulation of Jacobian matrix $\mathbf{J}^*$ is described in the Appendix A.2. $\mathbf{J}_7$ can be obtained directly from the Panda robot's control interface.

2.3 Proposed control techniques

In order to control the developed robotic system, two different control schemes are proposed, evaluated, and compared using a scenario simulating the laser ablation of cholesteatoma inside the middle ear cavity. One is end-frame teleoperation, when the second consists of the combination of macro-comanipulation and micro-teleoperation. In the latter, the Panda robot is controlled by comanipulation and the micro-scale tool by an embedded 2 DOF joystick.

2.3.1 End-frame teleoperation

The end-frame teleoperation is a referenced control method in MIS. In our approach, the surgeon can directly control the system end-effector (flexible endoscope tool-tip) by a master arm, while the RCM kinematic constraint is automatically fulfilled by the controller exploiting the redundancy of the kinematic chain as described in section 2.2. The advantage of using such an approach lies in the direct mapping between the master arm and the end-effector motion while the RCM constraint remains transparent for the user. However, this approach requires a precise registration between the patient frame and the robot frame along with an accurate positioning of the kinematic constraint location with respect to the robot base frame.

The Jacobian matrix $\mathbf{J}^*$ is a rectangular matrix with only five inputs (joint variables) and six outputs (task space variables); thus, one component of the task space has to remain uncontrolled. As the tool-tip rotation around its own axis z_9 is of no importance for a pointing task, this corresponding DOF can remain uncontrolled without affecting the task execution. Thus, in order to derive a corresponding reduced square Jacobian matrix $\mathbf{J}_{tip} \in \mathbb{R}^{5\times5}$, the operational rotation velocities are shifted to the micro-tool tip frame $\mathcal{R}_9$ and a selection matrix $\mathbf{S}$ is applied.

$$\mathbf{J}_{tip} = \mathbf{S} * \begin{bmatrix} \mathbf{I}_{3\times3} & 0 \\ 0 & {}^{rcm}\mathbf{R}_9 \end{bmatrix}_{6\times6} * \mathbf{J}^* \quad \text{with} \quad \mathbf{S} = \begin{bmatrix} \mathbf{I}_{5\times5} & \mathbf{0}_{5\times1} \end{bmatrix}_{5\times6} \tag{2.12}$$

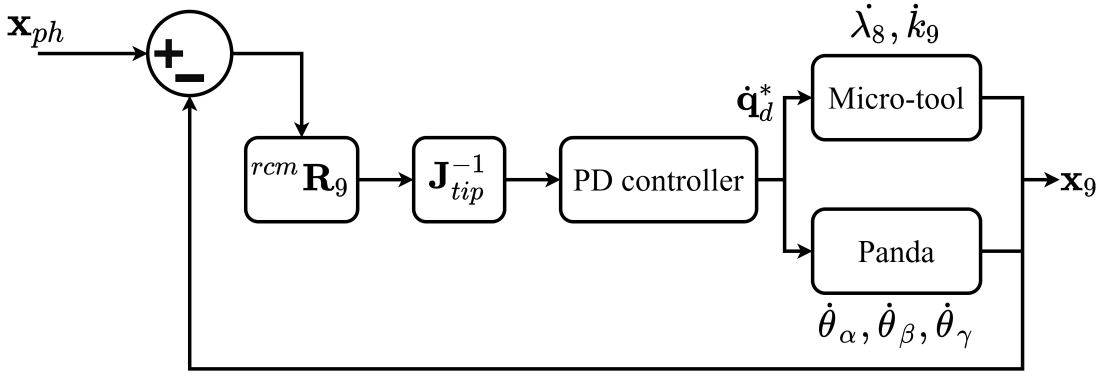

FIGURE 2.14: Control loop of the teleoperation.

The resulting end-frame teleoperation scheme is depicted in Figure 2.14. As we can see, the error at task-space level between the master-arm configuration (position value of Phantom Omni) $\mathbf{x}_{ph}$ and the feedback $\mathbf{x}_9$ from the tool-tip configuration is first

converted at joint-space level using the inverse of the reduced Jacobian matrix $\mathbf{J}_{tip}^{-1}$. Then, a proportional-derivative (PD) controller is applied to obtain the desired joint velocities $\dot{\mathbf{q}}_d^* = [\dot{\alpha}, \dot{\beta}, \dot{\gamma}, \dot{\lambda}_8, \dot{k}_9]^\intercal$ that serve as inputs to the Panda robot and the micro-scale tool unit. The 3 first joint velocity variables are used to control the orientation of the Panda arm, the 2 last ones are to control the translation and flexion of the actuated micro-tool.

2.3.2 Macro-comanipulation & Micro-teleoperation

The second control scheme is based on a dual loop control integrating macro-comanipulation and micro-teleoperation (MCMT). It is separated into two control chains (*cf.* the controller architecture of Figure 2.15) working in parallel: a control law for the macro-scale extra-corporeal robot and another for the micro intra-corporeal tool. Note that this control approach does not require any registration nor kinematic constraint modelling.

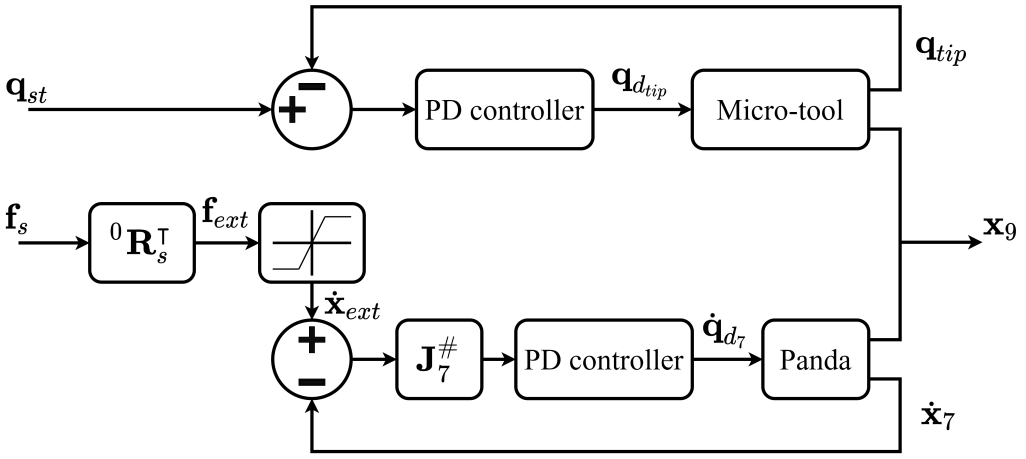

FIGURE 2.15: Control loop architecture of the macro-comanipulation and micro-teleoperation.

As shown in Figure 2.15, the upper control loop is meant to control the micro-tool using a joint-position control. The micro-scale subsystem is teleoperated using the 2 DOF joystick embedded on the arm terminal body, as presented in Chapter 1. The position of this joystick $\mathbf{q}_{st} = [\lambda_{st}, k_{st}]^\intercal$ is directly interpreted as the desired joint configuration of the flexible tool $\mathbf{q}_{d_{tip}}$.

The lower part of Figure 2.15 represents an admittance control of the end-effector position of the macro-scale Panda arm. The macro-scale extra-corporeal part is directly guided by the user in a comanipulation manner through measuring of the wrench $\mathbf{f}_s = [f_s^\intercal, \tau_s^\intercal]^\intercal \in \mathbb{R}^6$ applied at the grip handle by the operator. f_s is the applied linear force and τ_s, the applied torque value acquired by the F/T sensor. As $\mathbf{f}_s$ is expressed in the

sensor frame $\mathcal{R}_s$, the converted vector $\mathbf{f}_{ext}$ with respect to $\mathcal{R}_0$ can be computed as:

$$\mathbf{f}_{ext} = ({}^0\mathbf{R}_{rcm})^\intercal \, \mathbf{f}_s \tag{2.13}$$

by using the rotation matrix ${}^0\mathbf{R}_s \in \mathbb{R}^{3\times3}$.

$\mathbf{f}_s$ is converted into a velocity command $\dot{\mathbf{x}}_{ext}$ with a min/max saturation selector. The velocity command $\dot{\mathbf{x}}_{ext}$ is then converted into joint-space velocity command for the macro-scale part using $\mathbf{J}_7^{\#}$, the pseudo-inverse of the Jacobian $\mathbf{J}_7$ of the Panda robot. This joint-space velocity command is finally changed into a robot command $\dot{\mathbf{q}}_{d_7}$ by a PD controller.

2.4 Experimental comparison

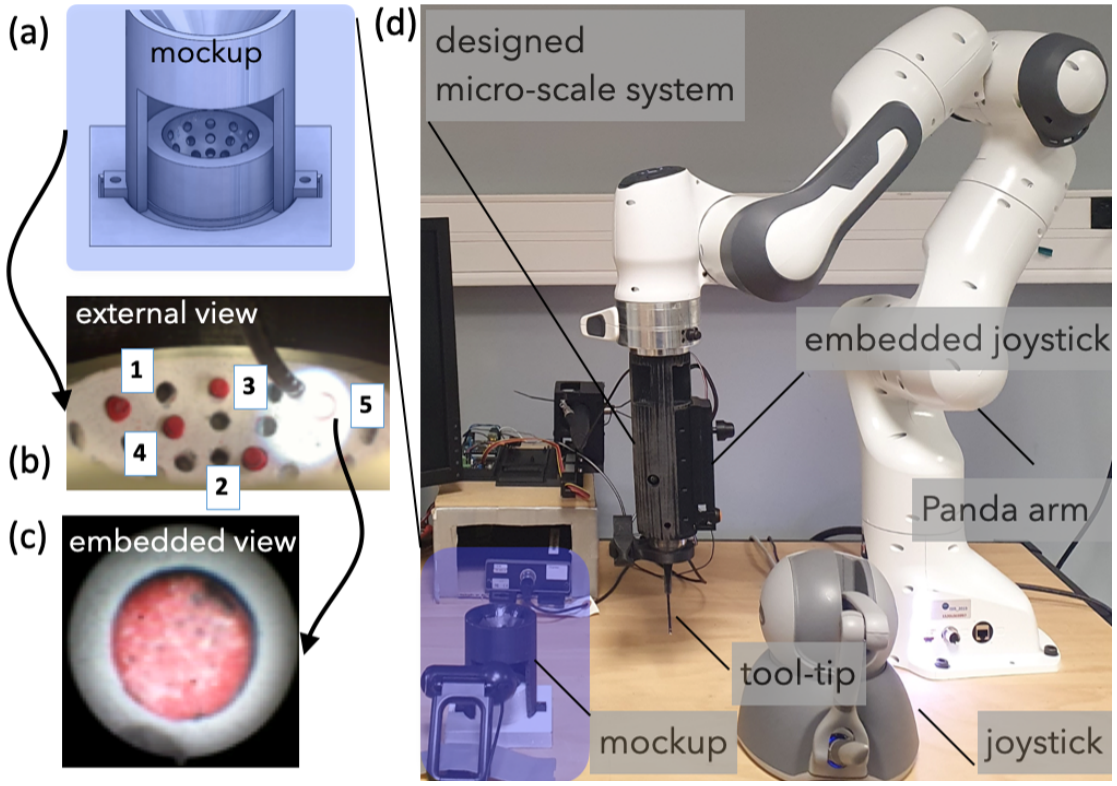

FIGURE 2.16: Experimental setup with (a) the fiberscope integrated visual feedback and (b) the webcam view.

To assess the proposed controllers, an experimental setup is configured as can be seen in Figure 2.16. The middle ear cavity is simulated by a mock-up with a conic entrance similar to a drilled hole in the mastoid in case of MIS procedure. The infected tissues inside the middle ear cavity are mimicked by five targets of 3 mm of diameter placed on a spherical surface (Figure 2.16). Note that consistently with the factor 3 between the diameters of the tool-tip in Figure 2.16 and of the future micro-device currently under

development at FEMTO-ST Institute, the mock-up in our test-bed has been realized with a scale factor of 3 as well. Two visual feedbacks are made available to the operator as during a real intervention, one via an external webcam (Logitech QuickCam Pro 9000) mimicking an endoscope view through the tympanic access (Figure 2.16(b)) and another from the internal camera that equips the flexible endoscopy system (Figure 2.16(c)). Note that the experimental setup has been designed with the help of an expert surgeon in Otology. The teleoperation mode is performed with the Sensable Phantom OMNI allowing the control of the tool-tip motion. The comanipulation mode is achieved thanks to the F/T sensor (ATI MINI-40) attached to the Panda robot end-effector, as well as to an ergonomically designed hand-grip. In this mode, the remaining 2 DOF (*i.e.*, the flexible micro-scale system) is controlled using the embedded joystick.

2.4.1 Validation Scenario

The carried-out validation scenario consists of pointing, in a predefined order (here, from 1 to 5), the infected tissues placed inside the cavity as depicted in Figure 2.17. The surgeon/operator has thus the task of positioning the tool-tip in front of each target with the tool-tip oriented as perpendicular as possible to the cholesteatoma. The tool-tip is initially placed at the RCM, then the operator starts controlling the tool-tip inside the cavity passing through the incision and pointing consecutively the five targets. A group of 15 inexperienced subjects, *i.e.*, persons who are not familiar with robotics (representing possible future clinicians), were recruited. Each volunteer was given a 10-minute training session before each test to familiarize him/her with the experimental setup and each of the developed controllers. The operator uses one of the proposed controllers to perform the pointing task. Both the trajectories and the final positions of the tool-tip are recorded to evaluate the performance of each controller.

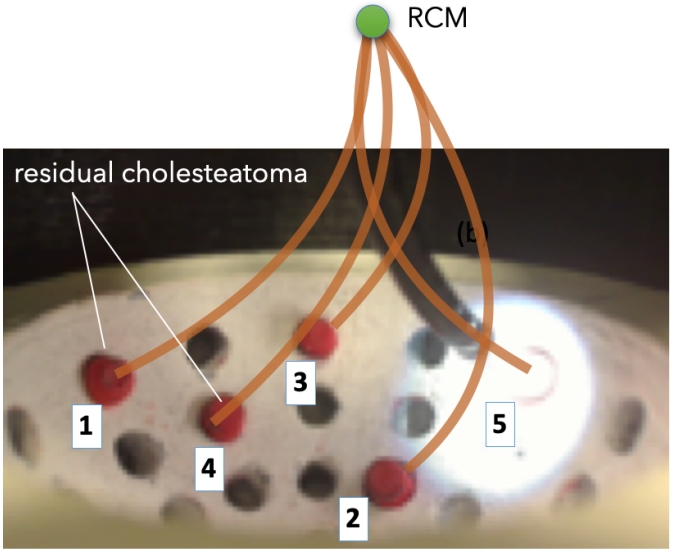

FIGURE 2.17: Conceptual illustration of the pointing task.

To assess the global performance of the designed multi-scale robotic platform as well as the developed controllers, the Cartesian pose error of the tool tip is recorded when the operator judges that each target (consecutively from 1 to 5) is successfully aimed. The control inputs (velocity, position, and force/torque) are also recorded in order to monitor the robot behaviour for each performed pointing task. Additionally, the kinematic constraint (RCM) violations are tracked for each volunteer as well as the time required to perform the whole scenario (pointing the five targets). Finally, the performance of both control methods are compared to each other and to a manual mode, which consists of pointing the target manually by keeping the fiberscope in hand while respecting the RCM constraint.

Note that using the MCMT control and manual handling, the user must be careful not to violate the RCM constraint. An alarm sound is triggered when the robot is about to collide the environment and incite the operator to move back the macro-scale system to the RCM position. In opposition, this constraint is automatically fulfilled when using the teleoperation mode.

2.4.2 Results and discussion

The obtained results for the developed control methods as well as the manual method are depicted in Figure 2.18. It shows the 5 targets (illustrated by a green circle ◯) to be pointed by each volunteer and the final 3D position of the tool-tip when the operator judges that the target is reached (represented by an oriented symbol ⊸). Knowing the spatial positions of targets as well as the final positions of the tool-tip at the end of the pointing task, it is possible to compute the linear and angular accuracy for each pointed target.

Accuracy

The numerical values for the accuracy evaluation are summarized in Table 2.3 and compared to those obtained when the task is performed manually.

As mentioned beforehand, the surgical procedure consists of accurately positioning a surgical laser in front of the infected tissues to be burned to prevent re-growth of the cholesteatoma. Consequently, the accuracy should be high in terms of positions and orientations along the x and y directions (*i.e.*, the tool tip should be in front of the target and should be perpendicular to the $x-y$ plane of the target) without any requirement to touch it. This means that $\bar{e}_z$, and $\bar{e}_{\theta_z}$ can be considered less meaningful than the others cartesian errors. This explains why the linear and angular errors relative to the z axis are often greater than the others.

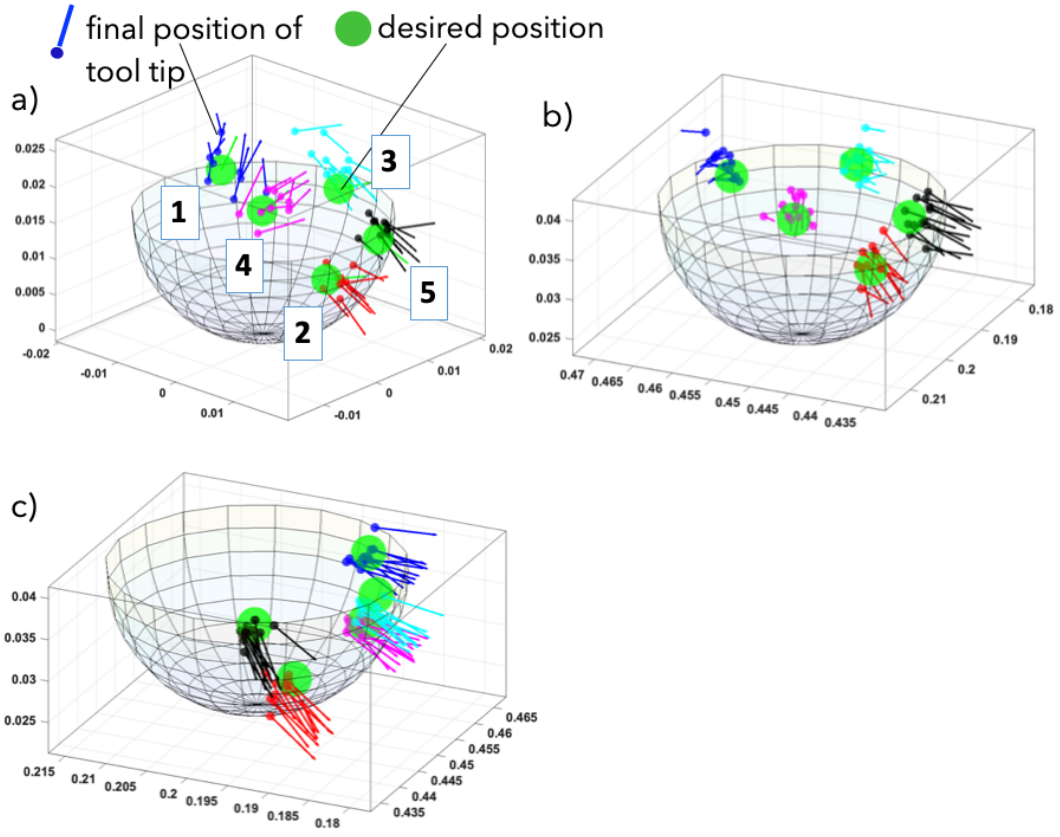

FIGURE 2.18: Plot of the results of the pointing task performed by the recruited volunteers. (a) results when the task is performed manually, (b) using the MCMT method, and (c) using the end-frame teleoperation method.

Control mode	Teleoperation	MCMT	Manual
$\bar{e}_x$ (mm)	0.98 ± 0.37	0.83 ± 0.15	1.4 ± 1.00
$\bar{e}_y$ (mm)	1.20 ± 0.28	1.20 ± 0.45	2.3 ± 0.94
$\bar{e}_z$ (mm)	0.95 ± 0.36	1.30 ± 0.10	2.2 ± 1.50
$\bar{e}_{\theta_x}$ (deg)	7.75 ± 1.37	8.54 ± 1.54	13.68 ± 13.88
$\bar{e}_{\theta_y}$ (deg)	4.83 ± 3.40	3.33 ± 1.61	17.68 ± 10.28
$\bar{e}_{\theta_z}$ (deg)	8.97 ± 1.17	9.64 ± 3.53	7.16 ± 4.57
$\bar{e}_{xy}$ (mm)	1.70 ± 0.90	$\mathbf{1.60 \pm 1.10}$	2.90 ± 1.50
$\bar{e}_{\theta_x,\theta_y}$ (deg)	2.92 ± 2.10	$\mathbf{2.46 \pm 1.49}$	20.84 ± 18.92

TABLE 2.3: Accuracy comparison of the different control modes.

Based on Table 2.3, the mean linear error $\bar{e}_x$ and $\bar{e}_y$ are both around 1 mm which is in phase with the predefined medical requirements [Dahroug et al., 2018b], where accuracy must be in the range of one millimeter. The obtained accuracy also reflects the margin of tolerance resulting from a purely direct control of position using only visual feedback. Otherwise, it can be underlined that the manual mode, even if it can be considered

accurate for linear motions, is substantially less accurate for angular motions compared to both developed controllers. The mean angular error $\bar{e}_{\theta_x}$ and $\bar{e}_{\theta_y}$ are quite similar for teleoperation and MCMT modes and are estimated to be near 5 °, when the manual mode shows an average angular error of about 15 °. It is reported [Scheiner and Schmitt, 2019] that the laser ablation requires minimal incidence angle (*i.e.*, to be perpendicular to the surface of interest) to be more efficient. Thus, low average angular errors from robot-assisted control modes seem to be an important advantage in performing laser ablation.

This conclusion is confirmed with a statistical analysis using an analysis of variance (ANOVA) method (Figure 2.19). The p-values for the position error and rotation error

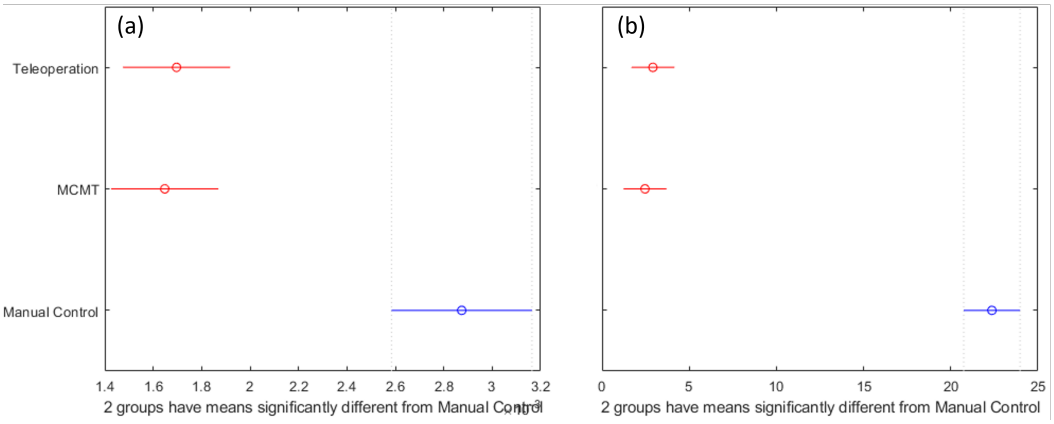

FIGURE 2.19: Results of ANOVA. (a) Analysis on position error $\bar{e}_{xy}$ (b) Analysis on rotation error $\bar{e}_{\theta_x,\theta_y}$.

were reported as below 10^{-7} for both robot-assisted control methods to manual control. This highlights that our developed control methods outperform the manual handling.

The first outcome of this experiment is that the proposed multi-scale robotic setup improves significantly the accuracy of the positioning task inside the middle-ear cavity, regardless of the selected control mode (teleoperation or MCMT). Besides, between the MCMT and teleoperation controllers, it can be highlighted that the MCMT method gives a slightly better accuracy. Also, according to the survey used in this experiment, the majority of the volunteers stated that the MCMT method is more intuitive and easier to use than the teleoperation mode.

Time required to achieve the pointing task

Control mode	Teleoperation	MCMT	Manual
Mean Time duration (s)	215.08	177.17	139.61
Standard deviation (STD) (s)	114.83	49.61	27.66

TABLE 2.4: Time required to achieve the proposed controllers.

The elapsed time to achieve the predefined task scenario (*i.e.*, pointing the 5 targets) with the different developed modes was evaluated. It appears that the manual mode is slightly faster ($139.61 \pm 27,66$ seconds) than the teleoperation (215.08 ± 114.83 seconds) and MCMT (177.17 ± 49.61 seconds) methods (Table 2.4). This may be due to the fact that the initial pose in the case of manual mode is closer to the incision hole compared to the robotic methods where the initial positions were slightly further. Otherwise, when considering only the robotic methods, the MCMT appears to be faster than teleoperation.

Respect of the spatial constraint

The last parameter to evaluate and compare between the three modes consists of the number of violations of the RCM constraint, which represents a potential risk of collision with the mastoid wall and the facial nerve that may be in the immediate vicinity for some patients.

Control mode	**Teleoperation**	**MCMT**	**Manual**
Mean violation number (-)	0.0	3.7	5.5
STD (-)	0.0	2.32	2.65

TABLE 2.5: Average number of violations of the RCM constraint recorded for each control mode.

As presented in Table 2.5, the MCMT control gives an average of 3.7 constraint violations per operator (an average of 0.7 violation per pointing task), when the manual mode scored in average 5.5 constraint violations (an average of 1.1 violations per pointing task). The high number of constraint violations in manual control can be explained by the tremor effect and by the presence of multiple visual feedbacks. To minimize the constraint violations, the operator had to directly look at the mock-up whereas the pointing task required focusing on the endoscopic views at the monitor. It was observed that subjects had higher concentration on endoscopic views and thus neglected the spatial constraint. The teleoperation mode is not concerned by this evaluation due to the fact that this method does not allow any linear motion of the entering part of the tool-tip at the RCM.

2.5 Conclusion

This chapter began by presenting a summary of existing control methods for surgical robots adaptable to the newly designed robot system. The benefits and drawbacks were also described to get a clear view of each technique.

Then, the main contribution of this chapter was the proposal of two control schemes: an end-frame teleoperation method and an approach relying on macro-comanipulation and micro-teleoperation of the whole redundant kinematic chain. The end-frame teleoperation is chosen since it is a reference control method. The MCMT is a new hybrid control method in which the benefit of teleoperation and comanipulation is appropriately combined.

To assess the performances of the developed robotic setup as well as the controllers, an evaluation scenario was implemented. It mimics the surgical procedure of infected tissue ablation with a surgical laser. To do this, a group of 15 volunteers was recruited. The designed robotic platform combined with the developed controllers has been shown to meet the requirements of a minimally invasive surgical procedure of the middle ear, especially the MCMT approach, in terms of accuracy, rapidity, intuitiveness, and usability.

To summarize, this chapter suggests a control solution of the novel macro/micro robot tool for cholesteatoma resection. The enhancement of tool handling is visible for both proposed control methods. Future work will have to apply and test the developed functions in experimental conditions similar to a real clinical case of middle ear surgery, particularly with respect to the geometrical shape and scale of a real middle ear.

Chapter 3

Pre-operative Positioning of the Robot

Contents

3.1 Introduction

As mentioned in the previous section, the positioning and the insertion of the developed macro/micro system has to satisfy the requirement of the cholesteatoma resection surgery. According to Chapter 2, the distal-part of the macro-scale, *i.e.*, the frame $\mathcal{R}_7$ of the robotic system, has to coincide with the entrance of the middle ear cavity. Starting from this chapter, additional functions related to the surgical protocol of cholesteatoma resection are treated. The next point to enhance cholesteatoma surgery is the tool pre-positioning at the early phase of the surgery.

To begin, the problem related to the developed system, *i.e.*, the incompatibility of the proposed control method for a positioning task, is described. Then, an overview of tool pre-positioning under surgical context is enlisted in Section 3.2. Then, Section 3.3 deals with a proposal of various control methods which can be applied to control the robotic setup during the pre-positioning task. Precisely, it introduces an adaptation of end-frame teleoperation and comanipulation developed in the earlier sections, and it presents the development of two shared control laws, which combine proximal (local) and global measurements. Specifically, local measurements provided by position or force sensors are combined with globally observed visual information acquired from a camera attached to the robot end-effector in an *eye-in-hand* configuration. Section 3.3 describes the development of two shared control methods; the parallel hybrid controller and the external hybrid controller wherein the vision-based control is associated with teleoperation or comanipulation control methods. Finally, Section 3.4 presents the implemented experimental setup to assess the different controllers and compare them to the classical teleoperation and comanipulation control modes. A discussion on the pros and cons of each control approach is also reported in Section 3.5.

3.2 Overview of tool positioning

This section explains the main problem of the previously developed control schemes. Then, existing solutions in the context of medical applications where surgical tools are positioned automatically are described.

3.2.1 Problem statement

The requirements and control specificities of middle ear surgery were presented in Chapter 1 and 2. The developed control methods require that RCM point to be fixed at the entry site of the middle ear cavity (Figure 3.1). It means that the previously developed control methods require that the macro-scale end-effector part coincides with the expected RCM position (including the orientation). This constraint imposes an initial pre-positioning task to be executed at the first phase of the operation.

Previous chapters focused on developing an interactive surgical robot and its control strategy in a millimetric workspace. This brings up to the question of how to control the tool-tip during the installation phase, from an arbitrary initial position to the surgical site (*i.e.*, the expected virtual RCM position as depicted in Figure 3.1).

In opposition to tool handling inside the middle ear, the installation process involves a broader gesture of the surgeon. Thus, developed control methods in Chapter 2 seems to be incompatible for a broader range of motion. It is impossible for a surgeon to

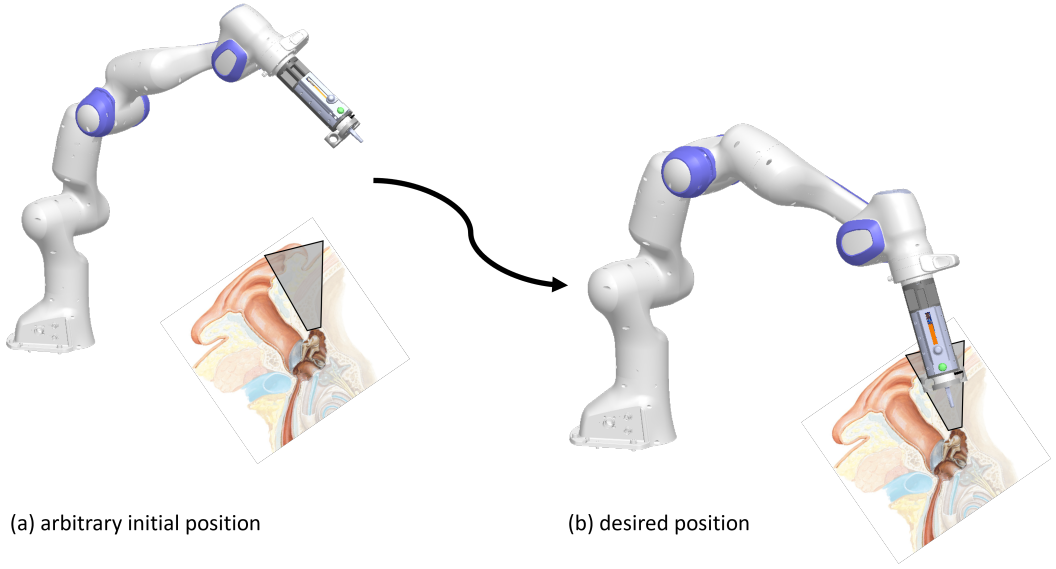

FIGURE 3.1: Figure depicting the positioning of the robotic system from (a) an arbitrary initial position to (b) a desired RCM position.

control the robotic system with the developed control method to reach the desired tool-tip position. It would slow down the surgery and be seen as inefficient. Therefore, specific motion control for the pre-positioning task is necessary to install the surgical configuration. This controller has to enhance control velocity, accuracy, and precision of the tool initial positioning.

3.2.2 Robot tool positioning

The question of tool pre-positioning or tool installation in surgery is less representative than problems related during the operation. However, it is a prominent issue for surgeries that require pre-planning of the surgical spot. Thus, precise tool positioning at the early stage of a surgical workflow is mandatory. The installation protocol of the robot depends on the patient's morphology, surgical parameters, and spatial constraints. Following paragraphs enlist used methods to position a robotic tool to a specific point (*e.g.*, RCM position, surgical point of interest) and in different applications.

Robot pre-positioning on the surgical site can be classified into 2 categories:

- The robotic system is guided manually by the surgeon.
- The robotic system assists the tool guidance of the surgeon.

Manual guiding by surgeon

First, the typical way to position a robot tool is to guide manually by an operator directly. It is the simplest method to install a tool near the surgical area.

An example of a robot in laparoscopic surgery is the Da Vinci system from Intuitive™ [Guthart and Salisbury, 2000]. The Da Vinci robot is positioned manually by a human operator before starting the intervention. As already mentioned in the previous chapter, the back-drivability of this robot gives an easy insertion of the tool (*e.g.*, cannula, forceps) throughout the pre-placed trocar. However, the installation process is time-consuming. First, the RCM point is defined by the robot and not the patient, a marker indicating the RCM is placed on the tool. It means a specific actuated surgical cart has to be prepared to place the robot. The second point is due to a high number of robots, a specific protocol including the inspection of joint angle configuration, collision avoidance, has to be managed before beginning the surgery. These points make the installation process more challenging.

FIGURE 3.2: Installation scheme of Da Vinci robot.

In Nagoya University, a robotic system [Colan et al., 2020] for endoscopic nasal surgery has been developed, *i.e.*, for tumor or pituitary adenomas resection. To specify the requirement of such operation, a rigid tool and rigid endoscope have to penetrate inside the nasal cavity along 100 mm to reach the surgical area, *i.e.*, the sella region. The developed system is a 6 DOF robot arm where 2 DOF or 4 DOF [Arata et al., 2019] forceps tool can be attached. This study also detailed the pre-positioning task; the operator has to directly insert the forceps inside the nasal cavity by a comanipulation method. The positioning task is related to MIS, where the entry hole of the nasal cavity constraints the insertion. So, the first task is to put the tool-tip near this RCM point to save its 3D coordinates. Then, the insertion is done with only 3 DOF, *i.e.*, the translation

to penetrate inside the nasal cavity, 2 rotations from the RCM with an impedance control of the fulcrum motion via a variable damping parameter.

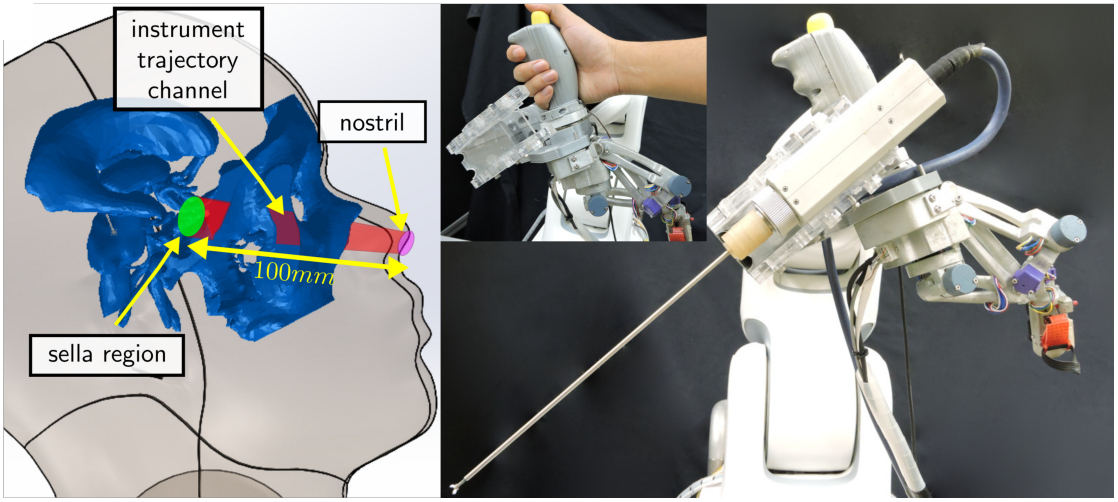

FIGURE 3.3: Endonasal surgical robot [Colan et al., 2020].

In orthopedic knee replacement surgery, the robot's positioning is important since the key issue is to plan the surgical trajectory as optimal as possible. For the osteotomy, [Maillet et al., 2005] have developed BRIGIT (MedTech), a robotic solution to assist osteotomy (Figure 3.4). This robotic solution can be manipulated by either comanipulation method or teleoperation with a Phantom Omni. To process the osteotomy, it requires a registration of multiple landmarks in order to characterize the cutting plan of bones. The installation process can be done in comanipulation manner wherein the surgeon chooses all the positions needed to operate.

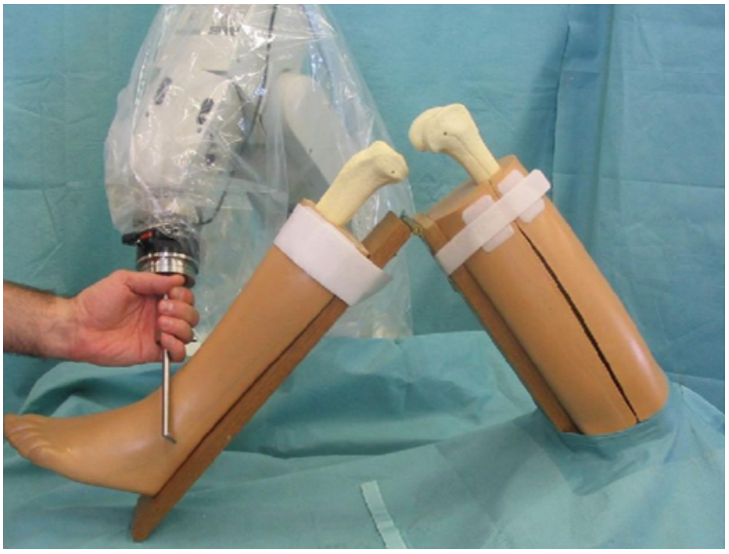

FIGURE 3.4: Use case of BRIGIT system [Maillet et al., 2005].

Computer-assisted guiding:

On the contrary, the installation process can be achieved with an assistance via imaging techniques and thus vision-based controllers. This kind of assistance is often seen for surgeries which require precise positioning of the tool (position and orientation).

In spine surgery, all necessary positions have to be defined precisely to diminish the possibility of damage on the spinal cord. [Tian et al., 2019] show a robotic solution for pedicle screw placement (Figure 3.5) on spinal bones. In this work, the investigation starts with selecting the implant position via intra-operative images and then planning the surgical trajectory. The next phase consists of registering selected positions into spatial coordinates for the robot. The robot's approach to points of interest is tracked via an optical tracking system that checks any type of movement of the surgical area (*e.g.*, movement due to respiration). The positioning process is achieved by moving the robot with an attached guide, including an F/T sensor.

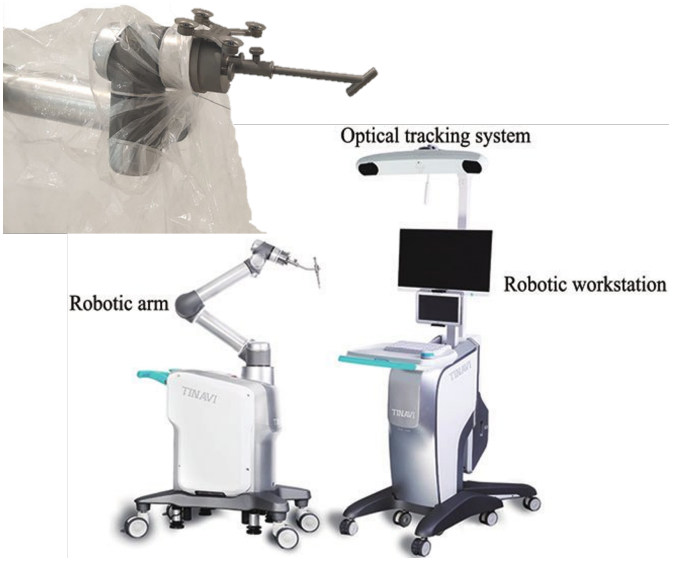

FIGURE 3.5: TianJi robotic system [Tian et al., 2019].

Brain surgery regroups diverse surgical acts on brain not only open brain surgery but also surgical acts such as brain biopsy, brain stimulation, stereo-electroencephalography (SEEG). ROSA system is applied for brain operations. [Liu et al., 2019] describes a specific surgery, lead implantation for deep brain stimulation assisted with ROSA system. To perform this, several markers that help position the tool are stuck on the cranial surface of the patient. These markers, which can be also visualized on *e.g.*, computed tomography (CT) scans help to determine the anatomical position for tool insertion. These markers are then used to track the head orientation during the insertion process (as depicted in Figure 3.6).

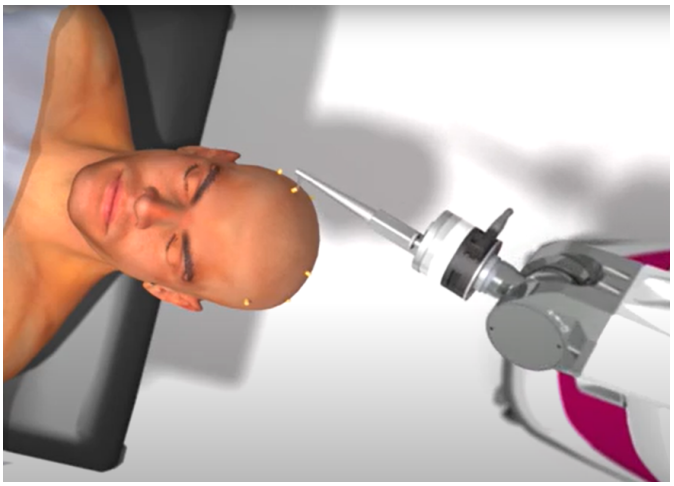

FIGURE 3.6: ROSA system for brain surgeries[1].

To finish, the enlisted categories of the pre-positioning process show that it is surgical requirement-dependent. Various sensors can be integrated into a robotic system dedicated to surgery. However, it is sure that each solution is answering to specific requirements of each surgery, *e.g.*, control difficulty, admitted precision of position, the difficulty of the installation process. Presented solutions have their own benefit and drawback:

- For surgeries that need an approximate installation position, it can be easier to opt for a manual guiding of the tool. When the surgeon is an expert, it is admissible to use a robotic system in a more manual manner, *i.e.*, the surgeon manipulates the robot himself; he/she knows all surgically important positions during the operation. It increases the cognitive load of the surgeon, thus it is not advisable for medical trainees who lack surgical experience.

- Fusion of multiple information is highly studied for MIS to decrease mental load. For example, integrating force sensors gives local information of tool pressure applied on biological tissues, and visual feedback provides the tool position. This supplementary information increases the precision and the ease of control for the surgeon during an operation. However, the assisted guiding of the tool requires several registration processes to prepare the surgery. Thus, the surgical time-cost may be elongated.

Therefore, a custom solution has to be proposed for the developed system for middle ear surgery. The main objective of this part is to create a wider scale controller to facilitate the installation of the micro-tool inside the middle ear throughout the perforated hole (mastoidectomy). Another objective is to increase the precision of positioning and

[1]This image is taken from: https://www.youtube.com/watch?v=kPzDq9Tb0uE

decrease the surgeon's cognitive load. All these objectives had to be achieved with the simplest method. To make it happen, a possible assisted control method combining the measurements from force sensors and vision sensors was also investigated [Morel et al., 1998, Mezouar et al., 2007, Prats et al., 2007, Liang et al., 2017, Adjigble et al., 2019].

3.3 Proposed methods

As the existing robot installation solutions are presented above, the next step is to develop a efficient and accurate control method which facilitate the positioning task. Thus, multiple control schemes are candidates in order to let the operator to perform the positioning task. In this section, following methods are proposed: classic teleoperation and comanipulation and two shared control laws that combine the visual feedback with force or position information.

3.3.1 Classical methods

To begin with classic methods, Figure 3.7 depicts the modified robotic system, the robot arm, and the joystick with their associated frames and the notations that are used in the following. Because the micro-tool (fiberscope) is not used during the initial positioning, the robot configuration is simplified with a rigid rod attached at the distal part of the macro-part system (Panda robot).

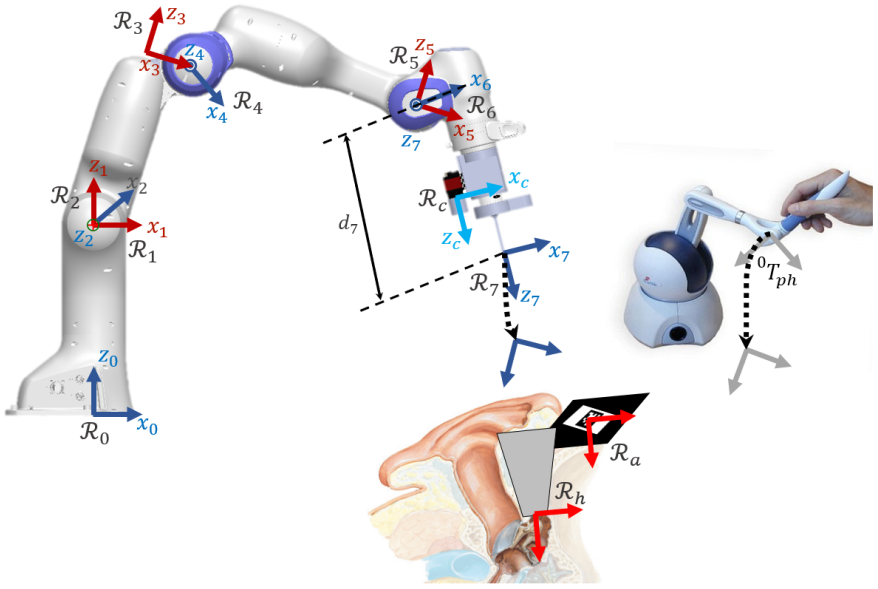

FIGURE 3.7: Kinematic model of the robotic system with the associated frames, the joystick for the teleoperation and the target positions (marker and incision hole).

End-frame Teleoperation

Unlike the previously described end-frame teleoperation in Section 2.1, the teleoperation mode developed in this chapter aims at controlling the distal part of the modified system, the frame $\mathcal{R}_7$. The teleoperation is also based on a position-based controller allowing the interpretation of the local pose of a Phantom Omni end-effector as the desired pose of the tool-tip attached to the robot arm. The motion of the joystick is directly mapped into the robotic system's end-effector space, which gives an intuitive position-based control for the user.

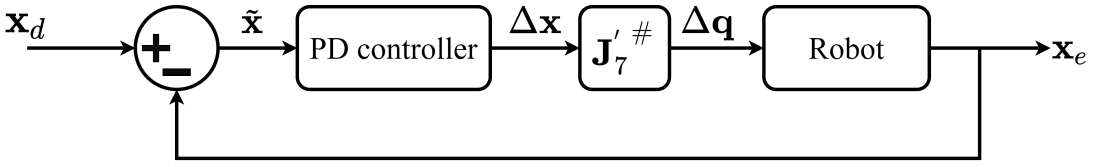

FIGURE 3.8: Control scheme of the classical teleoperation.

The control scheme is also identical to Chapter 2, the desired position $\mathbf{x}_d$ of the joystick expressed in frame $\mathcal{R}_7$ is used as the control input (Figure 3.8). Using the continuous mapping between robot end-effector motion and that of the joystick, the position error $\tilde{\mathbf{x}}$ (on the end-effector's position) is expressed as

$$\tilde{\mathbf{x}} = \mathbf{x}_d - \mathbf{x}_e \tag{3.1}$$

where, $\mathbf{x}_e$ is robot end-effector positions. Then, $\tilde{\mathbf{x}}$ goes through a proportional-derivative (PD) controller in order to get the control set-point $\Delta\mathbf{x}$. Therefore, the robot joint space velocities $\Delta\mathbf{q}$ are obtained from the task-space velocities using the pseudo-inverse of robot's Jacobian $\mathbf{J}_7^{'\#} \in \mathbb{R}^{7\times6}$:

$$\Delta\mathbf{q} = \mathbf{J}_7^{'\#}\Delta\mathbf{x} \tag{3.2}$$

Note that the robot's Jacobian matrix $\mathbf{J}_7^{'}$ is the same as $\mathbf{J}_7$ from Chapter 2 except the parameter d_7 from the modified D-H parameter with $d_7 = 0.196\ m$.

Comanipulation

Another interesting method to control the motion of the robotic system is comanipulation. In this chapter, the comanipulation scheme is the same as the comanipulation control loop from the MCMT method which is equivalent to an admittance control loop. In the presented system, the force sensor is attached to the robotic arm at the frame $\mathcal{R}_7$ where the control point is located. The implemented comanipulation mode is trivial and does not require any registration or specific parameters tuning.

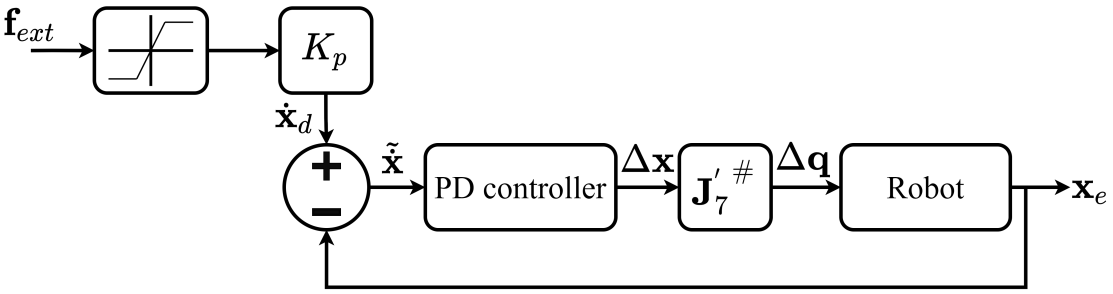

FIGURE 3.9: Illustration of the implemented control scheme in case of comanipulation mode.

To move the robot in the comanipulation manner, the user has a 3D printed and ergonomic wrist attached to the F/T sensor which itself is attached to the distal part of the robotic arm (Figure 3.10).

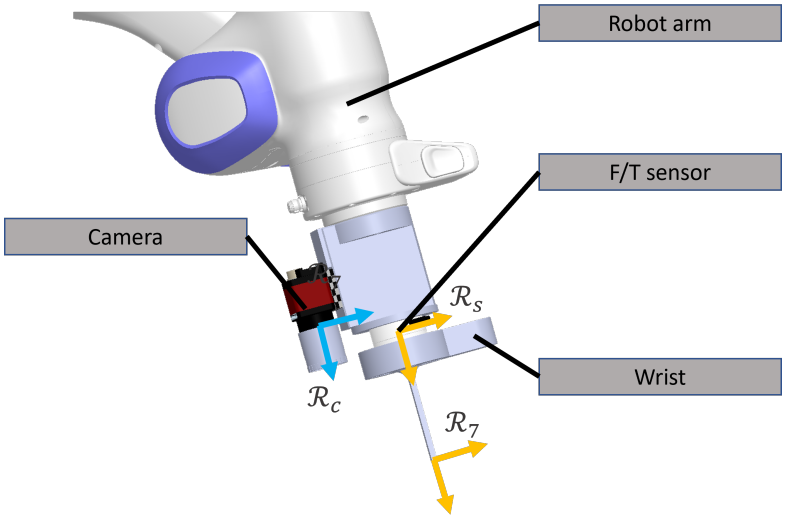

FIGURE 3.10: Image depicting the F/T sensor and wrist mounting on the robotic arm.

The user pushes the wrist and the F/T sensor provides the applied force and torque onto the wrist, represented by $\mathbf{f}_{ext}$, expressed in the frame $\mathcal{R}_7$. The measured force and torque are then converted to desired operational velocities, represented by $\dot{\mathbf{x}}_d$, and thanks to a proportional gain and min/max saturator, the output $\tilde{\dot{\mathbf{x}}}$ is injected into a PD controller (Figure 3.9). Finally, equation (3.2) allows converting the task-space operational control vector $\Delta\mathbf{x}$ to joint-space operational one $\Delta\mathbf{q}$.

3.3.2 Proposed shared controllers

In order to make the controllers more intuitive, easier to use, and faster, especially for a non-specialist (*e.g.*, a novice surgeon), shared control schemes are proposed. Indeed,

it has been shown that among the 6 DOF involved in a 3D positioning task, the three rotations (*i.e.*, θ_x, θ_y, θ_z) are the most difficult to achieve, in particular for a non-specialist [Adjigble et al., 2019, So et al., 2022a, So et al., 2022b]. Logically, in order to reduce the cognitive load on the surgeon, we have proposed two decoupled control modes allowing to decouple translations and rotations. Thereby, the three involved rotations will be managed automatically based on the vision feedback, when the three translations are still controlled by the previously introduced classic teleoperation or comanipulation.

Parallel hybrid

Consistently with the approach mentioned above, the first shared controller proposed in this section consists of a parallel juxtaposition of two internal loops. The first loop is a position-based (in teleoperation mode) or force-based (in case of comanipulation) loop to control the linear motion. The second is a vision feedback loop to manage the angular motion of the robot automatically. Figure 3.11 depicts the control diagram of the so-called parallel hybrid controllers [Mezouar et al., 2007].

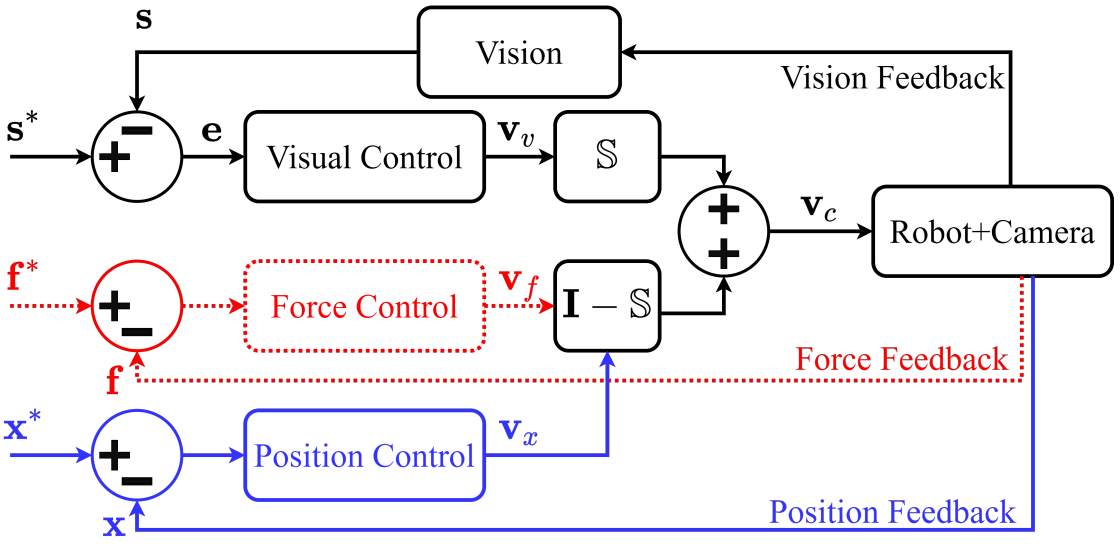

FIGURE 3.11: Parallel hybrid force/vision comanipulation (in red) and position/vision teleoperation (in blue) control scheme.

To have a perfect decoupled control law, *i.e.*, the rotations and the translations are controlled independently without one interfering with the other and then avoiding any conflict at the actuator level, we have opted for a position-based visual controller [Chaumette and Hutchinson, 2006, Ourak et al., 2016b]. Besides, to ensure the

orthogonality between force or position and vision controller outputs, we introduce a selection matrix $\mathbb{S}$.

$$\mathbb{S} = diag(0,0,0,1,1,1) = \begin{bmatrix} 0 & 0 & 0 & 0 & 0 & 0 \\ 0 & 0 & 0 & 0 & 0 & 0 \\ 0 & 0 & 0 & 0 & 0 & 0 \\ 0 & 0 & 0 & 1 & 0 & 0 \\ 0 & 0 & 0 & 0 & 1 & 0 \\ 0 & 0 & 0 & 0 & 0 & 1 \end{bmatrix} \tag{3.3}$$

The selection matrix $\mathbb{S}$ allows selecting the rotation DOF to be managed by the vision-based control and the remaining DOF, *i.e.*, translations to be controlled by the force or position controller.

As previously stated, the context of this work is to execute a middle ear surgery wherein the target corresponds to an incision of millimeter-diameter performed in the mastoid (access to the middle ear cavity). Following the overview in Section 3.2, a fiducial marker (*e.g.*, a printed *QR-code*) with known geometry can be sticked on an attachable structure applied next the mastoid bone [Liu et al., 2019] or directly on the mastoid bone [Katanacho et al., 2016]. Thus, the full pose of the target (orientations and translations) can be estimated in the camera frame $\mathcal{R}_c$. The homogeneous transformation from the frame $\mathcal{R}_h$ attached to the incision hole towards the camera frame $\mathcal{R}_c$ is represented by ${}^c\mathbf{M}_h$.

A feature characterizing the camera-hole's relative configuration can be extracted from ${}^c\mathbf{M}_h$ as $\mathbf{s} = (\mathbf{t},\ \theta\mathbf{u})^\top$, where $\mathbf{t}$ is the translational part $(t_x, t_y, t_z)^\top$ of the homogeneous matrix ${}^c\mathbf{M}_h$ and $\theta\mathbf{u}$ is the axis–angle representation of the rotation matrix. Furthermore, the Cartesian error $\mathbf{e}$ is regulated between the current position of the robot end-effector noted $\mathbf{s}$ and the desired position $\mathbf{s}^*$, corresponding to configuration when the tool is inserted in the incision hole. By considering $\mathbf{s} = (\mathbf{t},\ \theta\mathbf{u})^\top$ as the current position and $\mathbf{s}^* = (\mathbf{t}^*,\ \mathbf{0}_{1\times3})^\top$ as the desired one, the Cartesian error $\mathbf{e}$ is:

$$\mathbf{e} = \mathbf{s}^* - \mathbf{s} = \big(\Delta\mathbf{t}, -\theta\mathbf{u}\big)^\top \tag{3.4}$$

where, $\Delta\mathbf{t} = \mathbf{t}^* - \mathbf{t}$.

The time-derivation of $\mathbf{s}$, *i.e.*, $\dot{\mathbf{s}} = \big(\dot{\mathbf{t}},\ \dot{\theta}\mathbf{u}\big)^\top$ allows linking the camera velocity twist $\mathbf{v}_v = (v, \omega)^\top$ to the visual features variation [Marchand et al., 2002]:

$$\dot{\mathbf{s}} = \begin{pmatrix} \mathbf{I}_{3\times3} & \mathbf{0}_{3\times3} \\ \mathbf{0}_{3\times3} & \mathbf{L}_w \end{pmatrix} \begin{pmatrix} v \\ \omega \end{pmatrix} \tag{3.5}$$

where,

$$\mathbf{L}_w = \mathbf{I}_{3\times3} - \frac{\theta}{2}[\mathbf{u}]_\times + \Big(1 - \frac{\text{sinc}(\theta)}{\text{sinc}^2(\frac{\theta}{2})}\Big)[\mathbf{u}]_\times^2 \tag{3.6}$$

in which $\mathbf{I}_{3\times3}$ is the 3×3 identity matrix and $\mathbf{L}_w$ is the interaction matrix such that $\mathbf{L}_w^{-1}\theta\mathbf{u} = \theta\mathbf{u}$ as reported in [Malis et al., 1999]. Note that, $\text{sinc}(\theta) = \frac{\sin(\theta)}{\theta}$, and $[\mathbf{u}]_\times$ being the anti-symmetric matrix associated to the vector $\mathbf{u}$. Therefore, the camera velocity twist can be expressed as follows:

$$\begin{pmatrix} v \\ \omega \end{pmatrix} = -\lambda \begin{pmatrix} \mathbf{t} - \mathbf{t}^* \\ \theta\mathbf{u} \end{pmatrix} \tag{3.7}$$

Finally, the selection matrix $\mathbb{S}$ allows expressing the parallel hybrid controller as follows: $v_c = v_f$ or v_x (provided by the force/position controller) and $\omega_c = -\lambda\theta\mathbf{u}$ (provided by the vision-based controller):

$$\mathbf{v}_c = \begin{pmatrix} v_f \\ -\lambda\theta\mathbf{u} \end{pmatrix} \text{or} \begin{pmatrix} v_x \\ -\lambda\theta\mathbf{u} \end{pmatrix} \tag{3.8}$$

External hybrid

When both the force/position and vision-based controllers work in parallel, there is a risk that the tracked visual features (*i.e.*, the marker) goes out of the camera FoV. This could jeopardize the accuracy of the positioning task. To tackle this issue, we have designed another hybrid controller as shown in Figure 3.12. The underlying idea is to express the control task as two hierarchical sub-tasks. The first task (priority sub-task) deals with maintaining the target at the center of the camera FoV, while the second one (secondary sub-task) is devoted to the regulation of the error between the current and the desired poses.

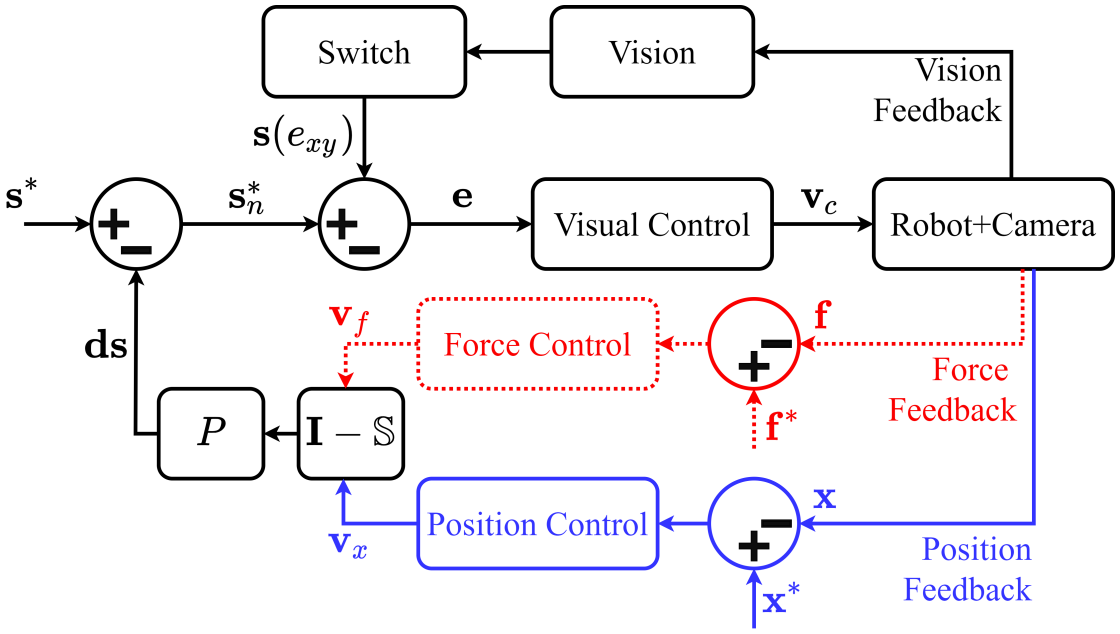

FIGURE 3.12: External hybrid force/vision comanipulation (in red) and position/vision teleoperation (in blue) control scheme with the function of keeping the target in the center of the camera FoV.

Therefore, to continuously maintain the target in the center of the camera FoV, we introduce a target locking mode based on the angular deviation $\theta\mathbf{u}_{lock}$ that can be defined as follows:

$$\begin{aligned} \theta u_{lock_x} &= \text{atan2}(t_y, t_z) \\ \theta u_{lock_y} &= \text{atan2}(t_x, t_z) \end{aligned} \tag{3.9}$$

where, t_x, t_y, and t_z are respectively the translation components along the x, y, z directions of the homogeneous matrix ${}^c\mathbf{M}_o$ that represents the 3D pose of the fiducial marker expressed in the camera frame $\mathcal{R}_c$.

In the target locking mode, the rotation part of the desired position is then defined as $\theta\mathbf{u}_{lock} = (\theta u_{lock_x}, \theta u_{lock_y}, \theta u_z)$. Besides, the Euclidean distance $e_{xy} = \sqrt{t_x^2 + t_y^2}$ expressed in the camera frame $\mathcal{R}_c$ is used to define a threshold to switch between free and locked modes:

$$\mathbf{s}(e_{xy}) = \begin{cases} \mathbf{s} = (\mathbf{0}_{1\times 3},\ \theta\mathbf{u}_{lock})^\top, & \text{if } e_{xy} > \epsilon = \sqrt{\frac{1}{2}}d \\ \mathbf{s} = (\mathbf{0}_{1\times 3},\ \theta\mathbf{u})^\top, & \text{else} \end{cases} \tag{3.10}$$

where, d is the side-size of the fiducial marker and ϵ is a pre-defined threshold triggering the switch between free and locked modes.

In this external hybrid force (or position) vision approach, the controller outputs are used to modify the desired visual features vector $\mathbf{s}^*$. This is associated in the visual servo control by considering that the desired visual features is $\mathbf{s}_n^*$ = $\mathbf{s}^*$ - $\mathbf{ds}$, where

$\mathbf{ds} = (\mathbf{t}_{ds},\ \mathbf{0}_{1\times 3})^\top$ and the Cartesian error is $\mathbf{e} = \mathbf{s}_n^* - \mathbf{s}(e_{xy})$. Thereby, the final camera velocity twist $\mathbf{v}_c$ is expressed as follows:

$$\begin{pmatrix} v \\ \omega \end{pmatrix} = -\lambda \begin{pmatrix} \mathbf{t}_{ds} - \mathbf{t}^* \\ \theta\mathbf{u}(e_{xy}) \end{pmatrix} \tag{3.11}$$

then,

$$\begin{aligned} v &= -\lambda(\mathbf{t}_{ds} - \mathbf{t}^*) \\ \omega &= \begin{cases} -\lambda\theta\mathbf{u}_{lock}, & \text{if } e_{xy} > \sqrt{\frac{1}{2}}d \\ -\lambda\theta\mathbf{u}, & \text{else} \end{cases} \end{aligned} \tag{3.12}$$

The proposed hybrid controllers are designed in an *eye-in-hand* configuration, *i.e.*, the camera is mounted on the robot arm. Thus, the relation between the robot velocity $\dot{\mathbf{q}}$ and the camera velocity $\mathbf{v}_c$ is obtained as follows:

$$\dot{\mathbf{q}} = -\mathbf{J}_{\mathbf{7}}^{'\,\#}\ {}^0\mathbf{V}_c\ \mathbf{v}_c \tag{3.13}$$

where $\mathbf{J}_{\mathbf{7}}^{'\,\#}$ is the pseudo-inverse kinematic Jacobian matrix of the 7 DOF robot arm in the base frame $\mathcal{R}_0$, and ${}^0\mathbf{V}_c$ is the transformation matrix from $\mathcal{R}_c$ to $\mathcal{R}_0$. The latter is constructed as:

$${}^0\mathbf{V}_c = \begin{bmatrix} {}^0\mathbf{R}_c & {}^0\mathbf{t}_{c_{[\times]}}\,{}^0\mathbf{R}_c \\ 0 & {}^0\mathbf{R}_c \end{bmatrix}$$

where ${}^0\mathbf{R}_c$ is the 3×3 rotation matrix from $\mathcal{R}_c$ to $\mathcal{R}_0$, ${}^0\mathbf{t}_c$ is the 3×1 associated translation vector, and ${}^0\mathbf{t}_{c_{[\times]}}$ is the skew symmetric matrix associated to the vector cross-product.

3.4 Experimental validation

The experimental setup was modified to adapt to the developed controllers' assessment protocol. It consists of a 7 DOF robot arm (same as Chapter 2) in which a different micro-part is fixed at the end-effector. The micro-part is a 3D printed tool (2 *mm* of diameter), which mimics a typical surgical instrument used in the middle ear. A standard CCD camera, AVT Guppy PRO F033b (resolution: 800×600 pixels and frame-rate: 25 images/second), is also mounted in an *eye-in-hand* configuration on the robot end-effector (Figure 3.7).

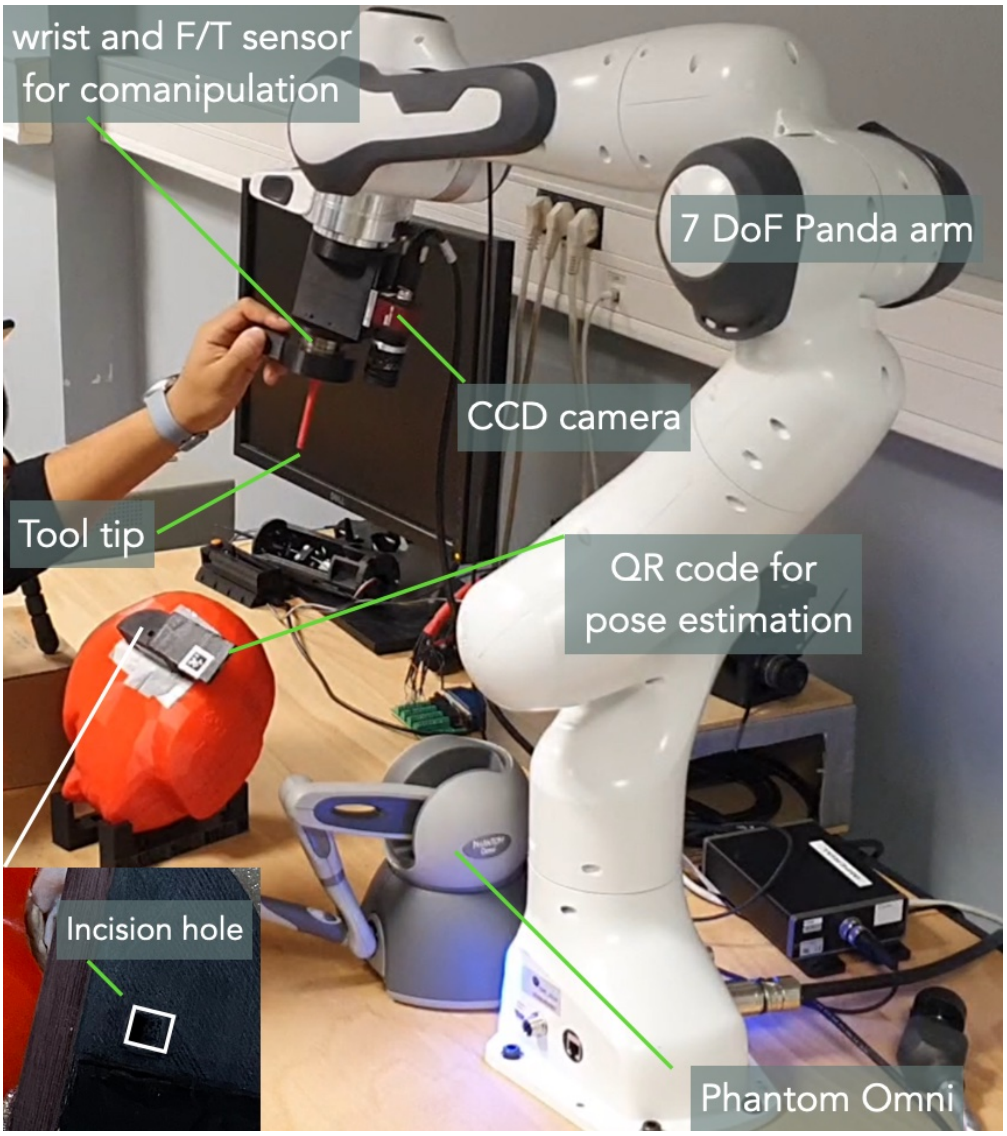

FIGURE 3.13: The developed experimental setup for this work.

However, the experimental setup keeps the same control devices for the operator. A Sensable Phantom Omni joystick is used to teleoperate the tool-tip of the system. As for comanipulation, a 6 DOF F/T sensor (ATI MINI-40) is fixed at the micro-tool part.

A head phantom at scale $1:1$ is positioned in order to simulate the position of a patient on the operating table. The tunnel drilled on the head has the same shape as the 3D tool fixed on the robot, with a tolerance of $0.5\ mm$. For the shared control methods, an *Apriltag* [Olson, 2011] of about 3 cm square is positioned next to the drilled hole. This fiducial marker is used to estimate the pose of the hole in the CCD camera frame as depicted in Figure 3.13. Note that the *AprilTag* is positioned next to the incision hole, with a distance equals to that of between the tool-tip and the camera. This is to maintain the marker inside the camera's FoV until the end of the insertion task.

3.4.1 Validation scenario

The experimental setup was designed to carry out a specific scenario where the 3D printed tool has to be positioned into the incision hole. Initially, the robot is placed in an arbitrary position. Then, the operator has to place the tool front to the incision point and insert the tool until the surface of the hole and a marking line on the tool coincide. The depth of the incision hole is estimated to be 5 mm. The marking line was drawn at 5 mm before the tool-tip. Note that the positioning task must be done manually without any visual feedback (*i.e.*, CCD camera's vision). Figure 3.14 shows an instant when the operator is performing the task, just before the insertion of the tool-tip inside the hole.

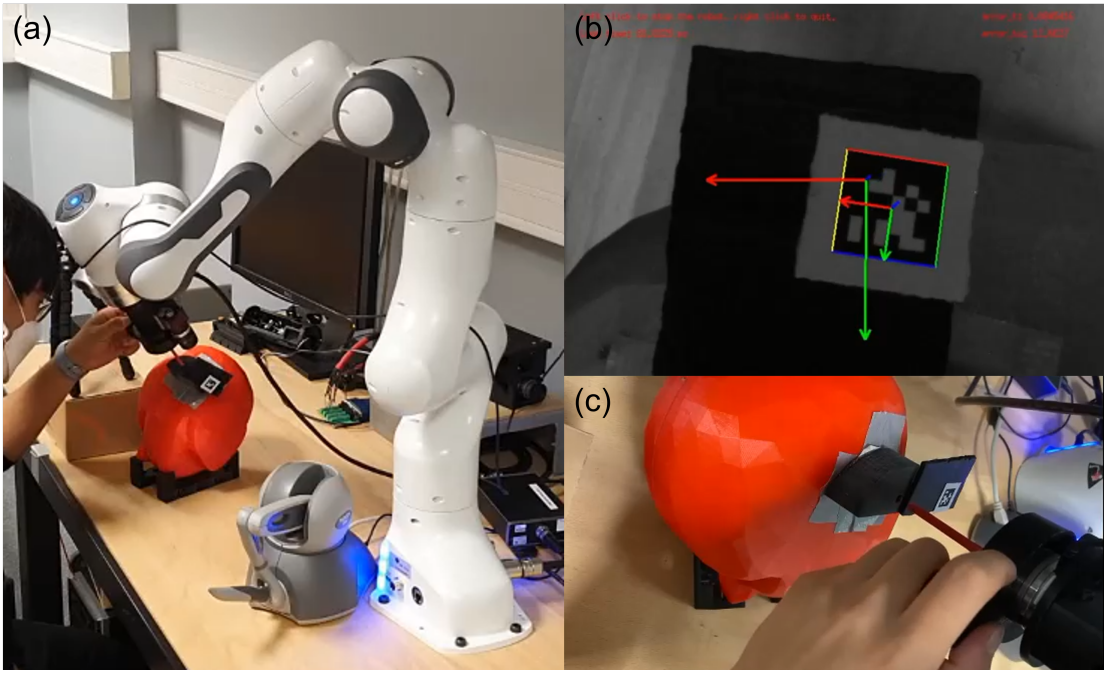

FIGURE 3.14: Images of validation task (a) General view in which the operator is inserting the tool-tip (b) View from the CCD camera showing the image position of the *AprilTag* (c) Local view depicting the head phantom.

A group of five participants (two experts and three novices) is volunteered to carry out the positioning and insertion tasks using different teleoperation (classic, parallel hybrid, and external hybrid) and comanipulation (classic, parallel hybrid, and external hybrid) control modes. Note that the experts are operators who have already manipulated robotic systems under teleoperation or comanipulation while the novices are operators who never had. For each of the performed tasks, Cartesian errors (along each DOF), the twist $\mathbf{v}_c$ expressed in the camera frame, the 3D trajectory of the robot end-effector, as well as the time required to achieve the tasks are recorded and analyzed. Note that the teleoperation modes were scaled with a scale factor set as optimal to do either the wide displacement motion or the precise control for the insertion.

Control	e_x (mm)	e_y (mm)	e_z (mm)	e_{θ_x} (deg)	e_{θ_y} (deg)	e_{θ_z} (deg)
CTo[1]	1.79 ± 1.57	1.21 ± 1.09	3.47 ± 6.84	6.88 ± 3.56	4.18 ± 3.45	9.16 ± 10.07
PHTo[2]	$\mathbf{0.78 \pm 0.55}$	$\mathbf{1.22 \pm 0.93}$	$\mathbf{0.83 \pm 0.77}$	$\mathbf{0.34 \pm 0.17}$	$\mathbf{0.31 \pm 0.24}$	$\mathbf{0.5 \pm 0.28}$
EHTo[3]	2.51 ± 3.65	1.39 ± 1.11	2.61 ± 4.79	6.46 ± 6.83	5.6 ± 5.93	0.76 ± 0.62
CCo[4]	0.73 ± 0.6	1.73 ± 1.09	1.52 ± 1.18	3.67 ± 3.33	7.49 ± 4.14	8.87 ± 9.22
PHCo[5]	$\mathbf{0.49 \pm 0.52}$	$\mathbf{0.97 \pm 0.5}$	$\mathbf{0.55 \pm 0.52}$	$\mathbf{0.37 \pm 0.27}$	$\mathbf{0.46 \pm 0.34}$	$\mathbf{0.52 \pm 0.31}$
EHCo[6]	1.16 ± 0.47	2.19 ± 0.96	1.12 ± 0.69	1.84 ± 1.62	5.88 ± 5.7	1.49 ± 1.37

* Tukey HSD p-value (teleoperation, mean angular error) : classical vs external hybrid $\rightarrow p = 0.005$ and classical vs parallel hybrid $\rightarrow p = 0.001$. Note that $p < 0.05$, which means statistically significant.
* Tukey HSD p-value (comanipulation, mean angular error) : classical vs external hybrid $\rightarrow p = 0.0016$ and classical vs parallel hybrid $\rightarrow p = 0.001$.
* Tukey HSD p-value (comanipulation, mean linear error) : classical vs external hybrid $\rightarrow p = 0.001$ and classical vs parallel hybrid $\rightarrow p = 0.0039$.

[1] CTo: Classical teleoperation
[2] PHTo: Parallel hybrid teleoperation
[3] EHTo: External hybrid teleoperation
[4] CCo: Classical comanipulation
[5] PHCo: Parallel hybrid comanipulation
[6] EHCo: External hybrid comanipulation

TABLE 3.1: Comparison of the positioning errors obtained with different control modes

3.4.2 Experimental Results

As mentioned above, the validation task was performed by 5 different participants. Each participant was asked to repeat the same task three times, alternatively using the developed controllers (3 control modes for the teleoperation and 3 others for the comanipulation).

Accuracy

The first analysis criterion concerns the accuracy of each control mode. The final error $\mathbf{e}_f$ corresponds to the difference between the final position of the robot end-effector and the reference position (recorded when the 3D printed tool is inserted into the incision hole). Table 3.1 summarizes the Cartesian error for each DOF.

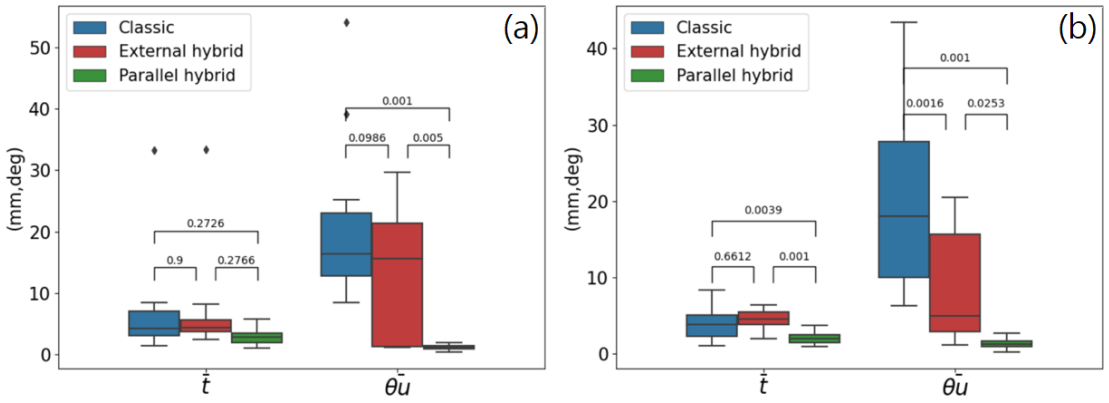

FIGURE 3.15: Mean steady-error and post-hoc Tukey HSD p-values for the evaluated control laws (a) teleoperation modes (b) comanipulation ones.

Concerning the comanipulation control modes, we can point out that both the shared control methods (parallel hybrid and external hybrid) outperform the classical control law (Figure 3.15(b)). As for the teleoperation case, the parallel hybrid is more accurate. The average linear error is $e_t = 0.67\ mm$ (1.32 mm and 1.49 mm for the classical and external hybrid methods, respectively), while the average angular error is $e_r = 0.45°$ (6.67° and 3.07° for the classical and external hybrid methods, respectively).

Globally, the parallel hybrid mode is the most accurate mode (Figure 3.15(a)) with a mean linear error (average of e_x, e_y, and e_z) estimated to be 0.94 mm (2.24 mm and 4.17 mm for the classical and external hybrid methods, respectively), while the mean angular error (average of e_{θ_x}, e_{θ_y}, and e_{θ_z}) is 0.17° (6.74° and 4.27° for the classical and external hybrid methods, respectively).

This conclusion is confirmed by a post-hoc Tukey HSD analysis to evaluate the relevance of the obtained statistical data. As reported in Table 3.1, the comparison of the different control modes is statistically relevant confirming that the parallel hybrid control law surpasses in term of accuracy the other control laws, in both teleoperation (Figure 3.15(a)) and comanipulation (Figure 3.15(b)).

Trajectory

The second evaluation criterion concerns the global behavior of the robot end-effector while conducting the task (positioning and insertion). To do this, the spatial trajectory performed by the 3D printed tool for each control mode was recorded. An example of this trajectory is shown in Figure 3.16(a), which depicts the 3D trajectory done by the tool-tip for each of the three control teleoperation modes achieved by one subject and Figure 3.16(b) shows the trajectories under the three comanipulation modes. It can be pointed out that those executed by the parallel hybrid method are smoother compared to the others. This suggests that the parallel hybrid method is more intuitive and makes it easier to manage positioning tasks.

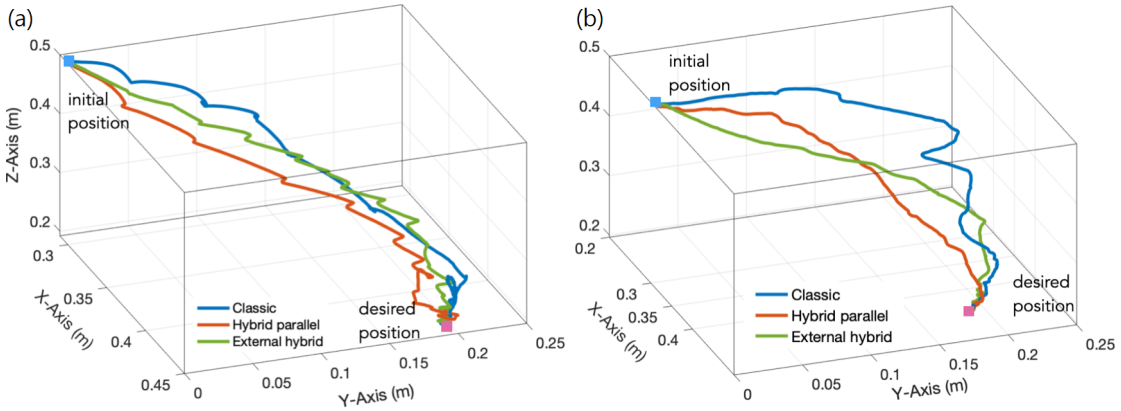

FIGURE 3.16: 3D trajectories carried out by an operator using the different implemented (a) teleoperation modes and (b) comanipulation ones.

On the other hand, it appears that the major difference between the trajectories lies mainly in the second phase of the task, *i.e.*, insertion of the tool into the incision hole. In the case of classical teleoperation and comanipulation methods, the operator has to repeat the process several times with small movements to find the correct orientation of the tool with respect to the incision hole before starting the insertion, while with the developed hybrid methods the operator can achieve this insertion with minimum effort.

Quality of error regulation

The third evaluation criterion concerns the behavior of the controllers according to the quality of the error $\mathbf{e}$ regulation as well as the velocities $\mathbf{v}_c$ sent to the robot while accomplishing the task. Indeed, as can be seen in Figure 3.17 for teleoperation, the regulation to zero of the error in each DOF is smoother in the case of hybrid teleoperation methods (Figure 3.17(t-b)(t-c)) compared to the classical one (Figure 3.17(t-a)). Additionally, both the hybrid controllers converge accurately towards zero when the classical mode shows a significant residual error in several DOF. The same observation can be made for the comanipulation evaluation as depicted in Figure 3.17 (lower row). In contrast to the classical comanipulation (Figure 3.17(c-a)), the hybrid comanipulation methods show error regulation that are smoother and close to exponential decay profile (Figure 3.17(c-b)(c-c)).

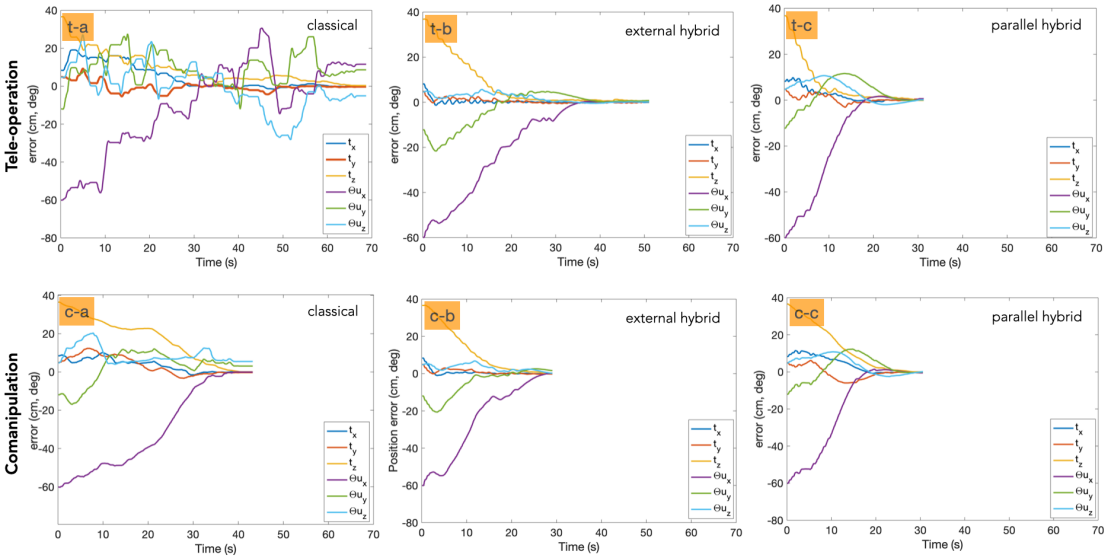

FIGURE 3.17: Error decay in each control mode. The upper row shows the teleoperation mode and the lower row represents the comanipulation one.

The velocity twist $\mathbf{v}_c$ sent to the robot was also recorded during each task. Figure 3.18 (upper row) depicts the velocity twist evolution with teleoperation controllers, while Figure 3.18 (lower row) depicts the same for comanipulation modes. In the case of teleoperation, the hybrid approaches (Figure 3.18(t-b) (t-c)) obviously shows better behavior compared to the classical ones (Figure 3.18(t-a)). Additionally, it can be noticed that the parallel hybrid methods (Figure 3.18(c-c)) outperform both the classical and the external hybrid ones (Figure 3.18(c-a)(c-b)).

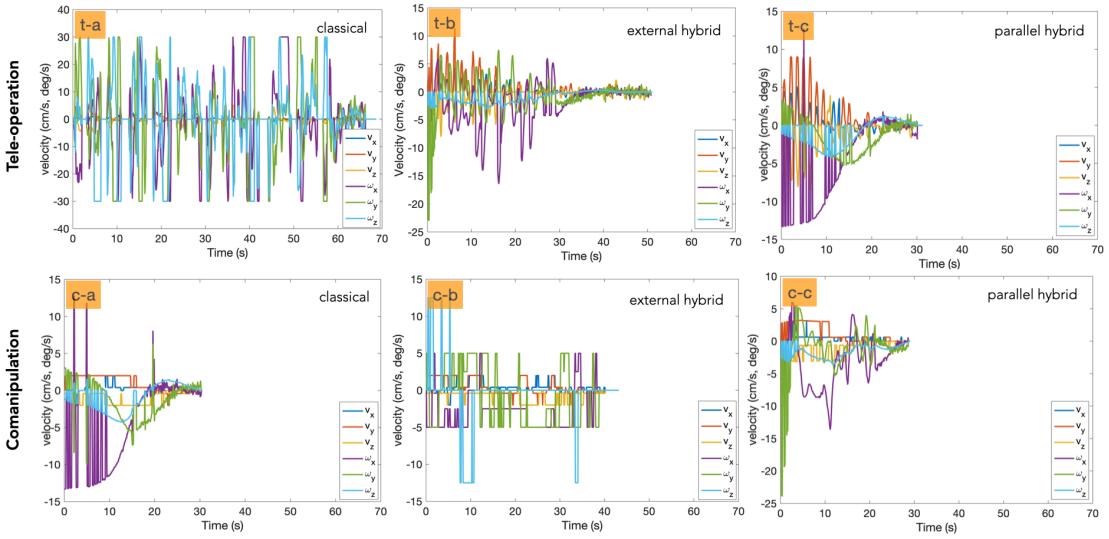

FIGURE 3.18: Illustration of the velocity twist involved in each control mode. The upper row shows the teleoperation mode and the lower row represents the comanipulation one.

Time required to achieve the task

It was noticed that the time required to achieve the task varies significantly from the hybrid methods comparing to the classical ones, for both the teleoperation and comanipulation modes.

Control mode	**Time duration (s)**
Classical teleoperation	64.05 ± 33.84
Parallel hybrid teleoperation	$\mathbf{40.53 \pm 10.09}$
External hybrid teleoperation	67.82 ± 26.53
Classical Comanipulation	39.22 ± 8.38
Parallel hybrid comanipulation	$\mathbf{29.03 \pm 6.94}$
External hybrid comanipulation	36.53 ± 5.40

TABLE 3.2: Time required to achieve the task with different control schemes.

Table 3.2 summarizes the observed average time. It appears that the parallel hybrid teleoperation approach requires in average 40.53 ± 10.09 seconds, which means 50% faster than the classical and external hybrid ones. The same conclusion can be made for the comanipulation methods. Indeed, the parallel hybrid controller requires on average 29.03 ± 6.94 seconds to achieve the task, which means approximately 25% faster than the others control schemes.

3.5 Conclusion

The objective of this chapter was to provide surgeons with an ergonomic, intuitive, and accurate control method for the tool positioning at the early stage of cholesteatoma surgery. The developed controllers in Chapter 2 were inappropriate for assisting the micro-tools initial installation since manual guidance of the robot by the operator is insufficient to position precisely to the entry point.

That is why the main contribution of this chapter is the design of shared control methods combining force/position control with a vision-based control. In total, six control schemes are implemented, evaluated and compared to each other: a classical end-frame teleoperation, two shared vision/position teleoperation controllers (called external/parallel hybrid methods), a classical comanipulation controller, and two shared vision/force comanipulation controllers (also called external and parallel hybrid methods). Note that the classical end-frame teleoperation and comanipulation are reference for comparison.

The performance of the developed controllers are analyzed under a validating scenario, *i.e.*, the insertion of the tool-tip inside a small incision hole perforated behind the ear lobe. The experimental validation was conducted with 5 participants (3 experts and 2 novices). Each participant did the positioning task three times. Various evaluation criteria: accuracy, the trajectory of the tool-tip, error regulation, and time required to achieve the implemented positioning task, were selected to compare qualitatively the performance of the developed control methods. The evaluation showed that shared control methods (external hybrid and parallel hybrid) surpass classical methods in both modes, *i.e.*, teleoperation, and comanipulation. Moreover, the parallel hybrid approaches are much more efficient than the external hybrid ones in almost all the evaluation criteria.

To summarize, this section suggests an efficient control solution for the macro/micro robot control during the tool positioning of cholesteatoma resection. This is particularly significant since the enhancement of tool handling is visible for both shared control modes (the best for parallel hybrid). Future work will focus on the implementation of the proposed controllers in real conditions of use, *i.e.*, minimally invasive surgery in the middle ear. Senior and junior surgeons will be recruited to evaluate the benefit of such approaches in the operating room.

Chapter 4

Vision-based Laser Steering

Contents

Previous chapters focused on innovating cholesteatoma surgery by integrating a new robotic system into the surgical protocol. The next challenge consists of improving the cholesteatoma resection process and then decreasing the current high re-operation rates due to residual cholesteatoma which is not removed during the first surgery [Gaillardin et al., 2012].

Chapter 4 is organized as follows: Section 4.1 introduces the definition of the residual cholesteatoma after an ablation surgery, its consequences, and the current treatment protocol. Section 4.2 briefly presents studies engaging image processing techniques for robot control such as visual tracking, image-based control strategies, path generation, and planning. Section 4.3 describes the detection and the visual tracking of both residual

cholesteatoma and laser spot and deals with the formulation of an image-based approach to control the laser spot displacements along the defined path. Section 4.4 formulates the generation of a path, which allows scanning all the individual residual cholesteatoma regions optimally. Section 4.5 presents the developed experimental robotic platform as well as the experimental evaluation of the proposed materials and methods.

4.1 Residual cholesteatoma

Residual cholesteatoma appearing after a first coarse manual removing of the bulky cholesteatoma is the most complicated issue in cholesteatoma resection surgery.

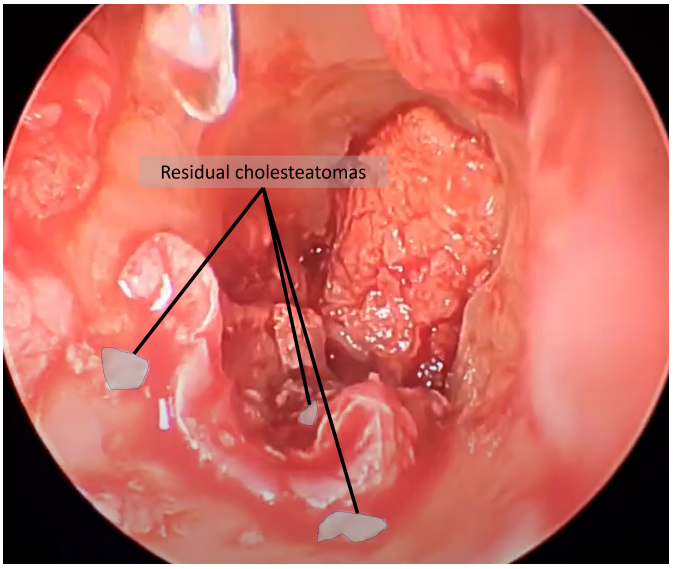

FIGURE 4.1: Endoscopic view of a residual cholesteatoma in the middle ear cavity[1].

Indeed, detecting and eliminating these residual pathological tissues are particularly challenging for a surgeon [Fichera, 2021]. The residual cholesteatoma size is in near sub-millimetric scale (as depicted in Figure. 4.1), and the treatment has to be done in the last phase of the operation when the fatigue level of the surgeon is at maximum. This makes manual treatment (*i.e.*, when the surgeon manually rakes the infected tissues) complicated or impossible in some cases and most of the time, residual pathological cells cannot be entirely eliminated in a single intervention.

The only option to fully remedy the problem is to get a second operation. A periodic follow-up after the first intervention, from 12 to 18 months, has to be carried out to monitor a possible regeneration of cholesteatoma. During this monitoring period, imaging techniques such as MRI [Williams et al., 2003, De Foer et al., 2008] or CT [Park et al., 2018], are employed to detect a possible regeneration of cholesteatoma. If it is the case,

[1]This image can be found in https://www.youtube.com/watch?v=tUR7pyY192w

a second surgery is performed. Figure 4.2 shows a regenerated cholesteatoma ball inside the middle ear, 6 months after the first intervention, with a size of 2 *mm* diameter.

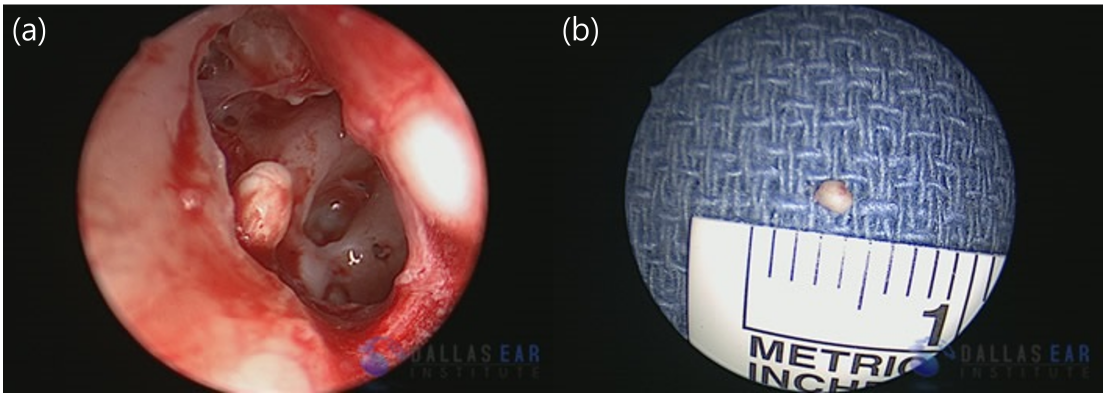

FIGURE 4.2: Extraction of regenerated cholesteatoma during the second look-up[2](a) Regenerated cholesteatoma ball inside the middle ear (b) Extracted cholesteatoma ball with its dimension.

The following study will consists of finding a solution to eliminate the residual cholesteatoma and reduce the surgeon's task load at the late phase of tissue resection/ablation. The solution we considered to tackle this problem is to integrate a function that removes the residual cholesteatoma with the incorporated laser source on our developed macro/micro-system. Indeed, employing a surgical laser to ablate the cholesteatoma has been shown [Hamilton, 2005] to possibly contribute to decreasing the rate of residual cholesteatoma down to 3% while conventional surgery has a rate of 30%.

Besides, in our approach we considered an automatic task execution instead of an interactive scheme with those developed in Chapter 2. Several reasons can be cited to back up this choice:

- the residual cholesteatoma are small and difficult to distinguish from other tissues,
- the operating site is often located in hidden side of the middle ear cavity,
- the hand tremor of the operator is incompatible with micro-surgery.

To make such an approach possible, one can use the image information from visual sensors and design a control law by exploiting key features from the obtained image [Espiau et al., 1992]. The implementation of a visual-based automatic control of residual cholesteatoma resection would decrease the surgeon's fatigue and contribute to reducing the regeneration rate of the residual cholesteatoma.

[2]These images can be found in https://www.dallasear.com/conditions-cholesteatoma-cases.html

4.2 Rapid overview of vision-based robotic laser surgery

Several studies can be found in the vision-based methods for surgical laser ablation [Azizian et al., 2014, Tamadazte et al., 2018]:

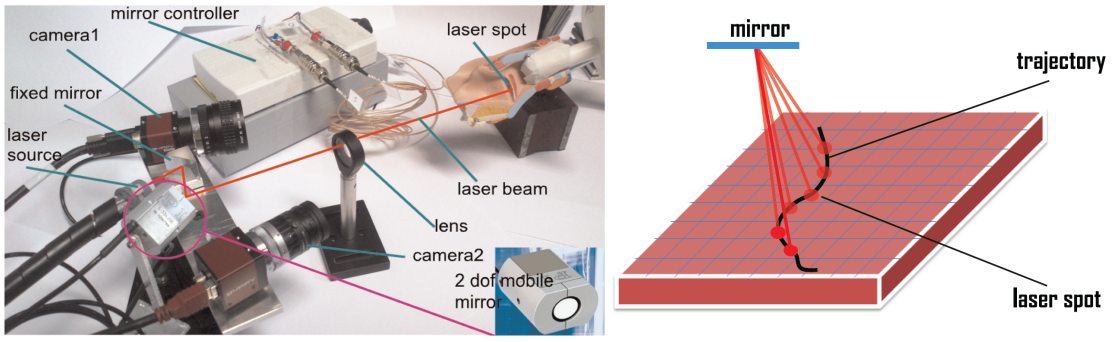

FIGURE 4.3: Experimental setup of the trifocal visual servoing a laser spot and the validating scenario of laser spot steering [Andreff and Tamadazte, 2016].

In micro-phonosurgery, [Andreff and Tamadazte, 2016, Renevier et al., 2016] worked on a laser control using a visual servoing controller stereo-vision feedback. The targeted system would be integrating 2 cameras and a 2 DOF actuating mirror which reflects the laser beam to the surface of vocal cords. As the location of the cameras and the actuating unit is known, an adaptation of a trifocal geometric relation gives the 3D position of any point inside the image frame. Thus, the laser spot visible from the 2 cameras can be controlled by a visual servoing strategy. The 2 DOF actuating mirror would steer the laser spot to reach the desired position or to follow the desired path (as shown in Figure. 4.3).

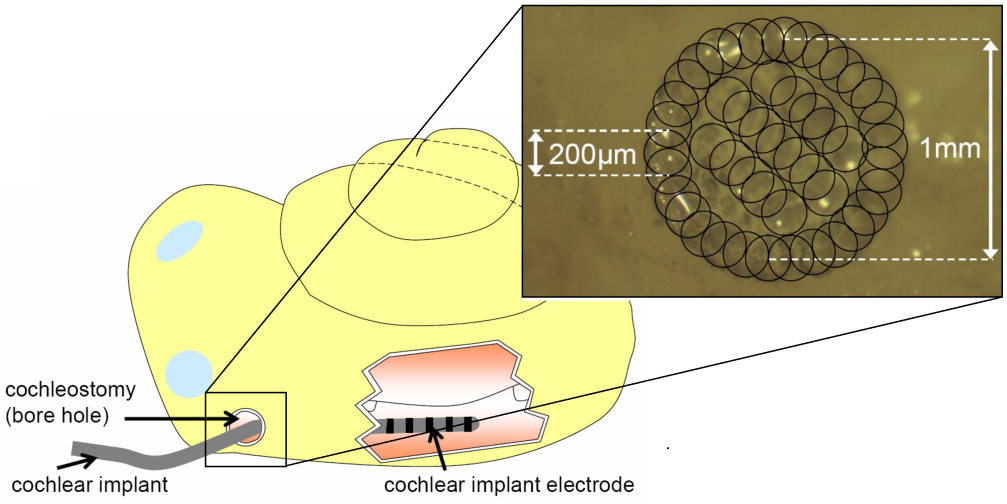

FIGURE 4.4: Vision-based cochleostomy using laser beam and the distribution of laser positions (black circle) to perforate the bore hole [Kahrs et al., 2008].

For ear surgery, [Kahrs et al., 2008] reports a laser ablation process to perforate a hole and install a cochlear implant. The objective of this study is to make a cochleostomy [3] by a laser beam on the cochlear system (Figure 4.4). The drilled hole lets the cochlear implant electrode enter inside this hearing organ. The drilling process is challenging due to the danger of damaging close hearing organs. To achieve such task, the ablation area is first monitored by a color camera to detect the boundary layers of the inner ear. Then, the laser source is automatically guided, and positions of target points are reached inside the borehole via visual servoing technique using a two-mirror galvanometric scanner.

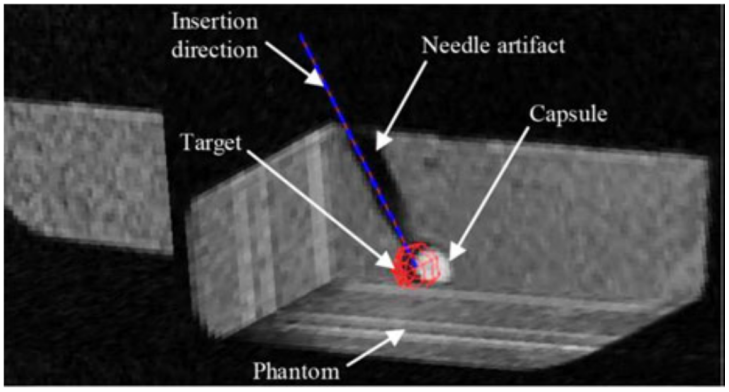

FIGURE 4.5: MRI image of the inserted needle approaching the target (in red) [Franco et al., 2015]

Other imaging techniques can be applied instead of conventional cameras, as demonstrated in [Franco et al., 2015]. This work presents a flexible needle-guiding robot operating in the abdominal cavity to make laser ablation of liver tumors. The needle-tip is in an asymmetrical shape; changing the orientation of the needle-tip leads to controlling the direction of its insertion. As the laser ablation is achieved without opening the abdominal wall, an MRI image stream is used to track the end-effector of the needle and the tumor visually. Thus, it makes a favorable condition to using a visual-based control technique to control the robot.

The above listed examples show that vision-based techniques can play a prominent role to make an automatic control of robotic systems, especially in medical applications. However, ablation does not mean one-point destruction of tissue. It is a continuous carbonization of an area of interest *i.e.*, the laser beam has to follow a path of interest to cover the area to be ablated and has to avoid the area where healthy tissues are.

[3] It is a perforation on the surface of the cochleovestibular organ

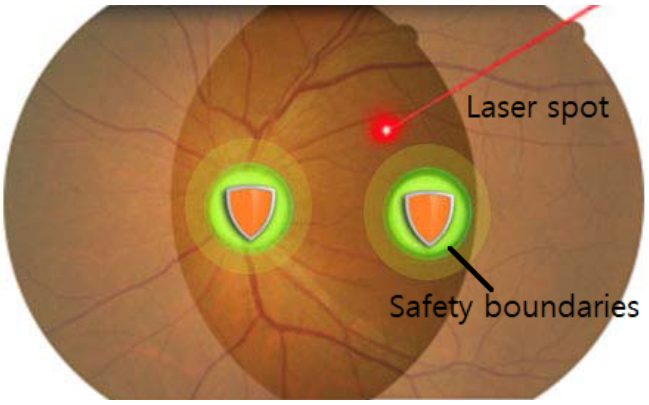

FIGURE 4.6: Demarcated safety zones – safe (unmarked), close (yellow), boundary (dark green) and forbidden zone (green) [Chng et al., 2015].

For example in retinal surgery, [Chng et al., 2015] presents an image processing technique in order to create a "forbidden zone" where the robotic tool must avoid shooting laser spots for safety reasons. This work introduces a shared control technique in which teleoperation control lets the user move the surgical laser for retinal tissues ablation. At the same time, a visual tracking algorithm checks the laser spot if the latter is near a "forbidden zone" *i.e.*, healthy retinal tissues, and if the laser enters the "forbidden zone", the visual servoing controller stops the laser spot motion (Figure 4.6).

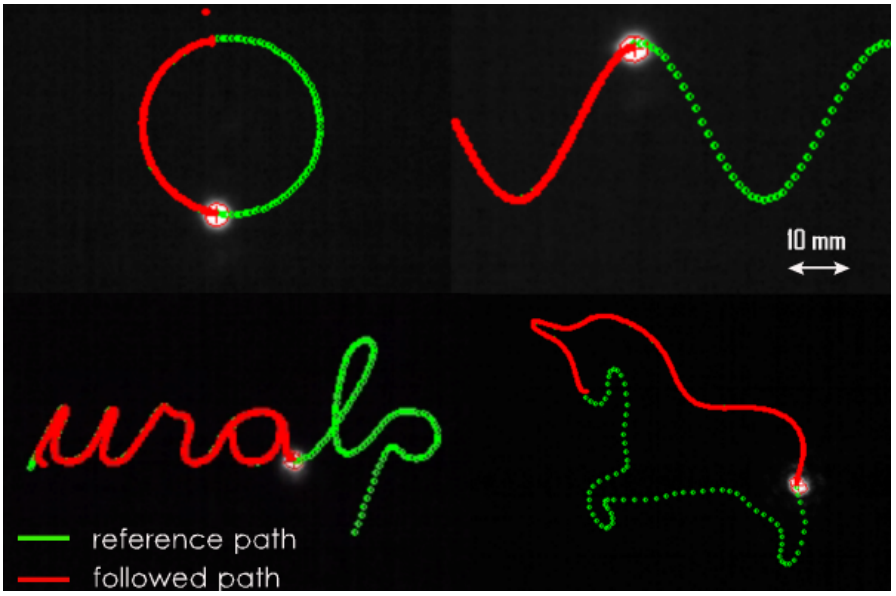

FIGURE 4.7: Image depicting an experimental validation of path following task using laser steering [Seon et al., 2015].

Also, the vision-based technique can be applied to steer a laser spot to a desired position. In [Seon et al., 2014, Seon et al., 2015], a laser steering method is presented in which the user defines himself the path to be followed by the laser. The defined path by the operator is divided into a long list of desired positions. The laser continues to

move to the next position as soon as it reaches the desired one. This study also suggests using a path rather than a trajectory. Path following is generally preferred in medical applications to avoid time-coupling in the velocity profile that characterizes trajectory tracking methods.

Subsequent studies in [Andreff and Tamadazte, 2016] show that most of the time the surgeon himself fully defines the path or area of interest. However, the residual cholesteatoma can occur randomly during the resection process. It means that creating a path manually can be difficult for the surgeon due to the significant number of residues. Consequently, an automatic path planning would reduce the surgeon's cognitive load if he had to draw this path by himself.

The above survey shows possibilities for creating an automatic laser ablation of residual cholesteatoma. Consequently, the solution we propose lies in developing an image-based laser steering controller with an optimal path generator linking and covering all the detected residual cholesteatoma. The observable laser spot inside the middle ear cavity would follow this generated path. Two elements are necessary to achieve this objective. The first is the generation of an optimal path starting from the laser spot initial position and passing through the geometrical feature representing the detected residual cholesteatoma. The second is the integration of a vision-based controller to guide the laser spot across the defined path.

4.3 Visual tracking and vision-based control

The first step of the proposed method concerns the detection of the residual cholesteatoma regions and of the laser spot and their visual tracking over time. The visual tracking algorithms presented in this section entail 2 points:

- The visual tracking of the laser spot is used for controlling the tool-tip of the surgical tool by providing essential image information to integrate a vision-based control of the developed robotic system.
- The visual tracking of the residual cholesteatoma regions provides necessary information (the image position of each residual cholesteatoma) to generate optimal path which the laser spot has to follow.

FIGURE 4.8: Endoscopic view of the middle ear cavity with simulated residual cholesteatoma.

Note that a residual cholesteatoma is a debris that remains in the middle ear cavity after the surgeon has resected the large parts of infected tissues. The residual cholesteatoma tissues are relatively small, randomly distributed in the middle ear, and have a whiter appearance than the rest of the healthy tissue. In our simulated environment, the residues of cholesteatoma are randomly superimposed on a real middle ear view, with various shapes, as can be seen in Figure 4.8.

4.3.1 Residual cholesteatoma and laser spot tracking

Laser spot tracking:

To track a laser spot, different open-source visual tracking algorithms were evaluated and the one that seems to be the most efficient and the most adapted for this task is the Channel and Spatial Reliability Tracker (CSRT) [Lukezic et al., 2017] available in OpenCV library[4]. It is based on the estimation of the reliability using the properties of a constrained least-squares solution in the filter design surrounding the region of interest suitable for tracking. Therefore, the channel reliability scores are used for weighting the per-channel filter responses in the object localization process. Note that the filter support can be adjusted during the tracking which allows enlarging the search region and improves tracking of non-rectangular objects.

The choice of the CSRT tracking algorithm is due to several motivations. The CSRT algorithm gives best performance in overall for single object tracking even if the resolution

[4]The OpenCV library can be found at: https://docs.opencv.org/3.4/d2/da2/classcv_1_1TrackerCSRT.html

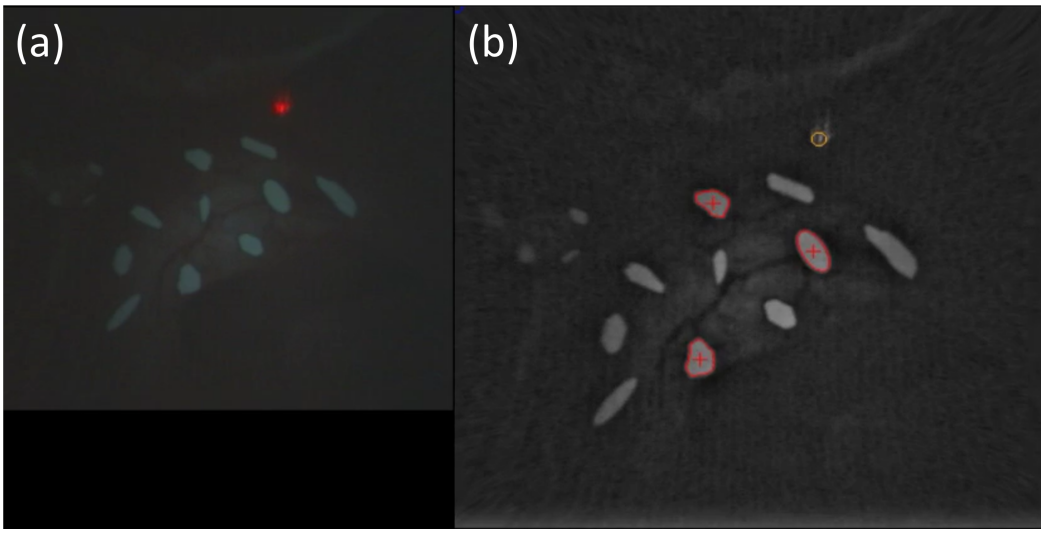

FIGURE 4.9: Figure depicting visual tracking method for the laser spot (a) Raw endoscopic view of the simulated image of middle ear cavity, the red point is the laser spot (b) Contour (in orange) of the laser spot representing the visual tracking after camera calibration and image processing of the endoscopic image.

and the camera frame rate of the image are low [Brdjanin et al., 2020]. It is also used either for simple object such as a tennis ball [Calandre et al., 2021] or for complex shape objects [Amitha and Narayanan, 2021] .

Residual cholesteatoma tracking:

As for the residual cholesteatoma, a image processing technique called "BloB tracker" from ViSP (Visual Servoing Platform) library [Marchand et al., 2005] is used[5]. The BloB tracker detects and tracks regions by comparing the color and intensity level of image pixels with its neighboring area. After comparison, areas presenting similar color level are then regrouped. As Figure 4.10B shows, the image simulating the cholesteatoma has a noticeable difference of color intensity than other part of the image. Using this color-intensity property, the residual cholesteatoma can be detected and visually tracked along this study.

Note that different image processing techniques or image sources than using a conventional camera can be applied for residual cholesteatoma. As previously mentioned, the detection and tracking of the residual cholesteatoma can be achieved with other imaging modalities such as OCT imaging [Gora et al., 2017], ultrasound imaging [Jang et al., 2002] or fluorescence imaging [Lademann et al., 2007]. The best option would be to integrate an OCT imaging seemed to give a higher accuracy than other techniques in detecting the residual cholesteatoma.

[5]The ViSP library documentation can be found at: https://visp-doc.inria.fr/doxygen/visp-daily/

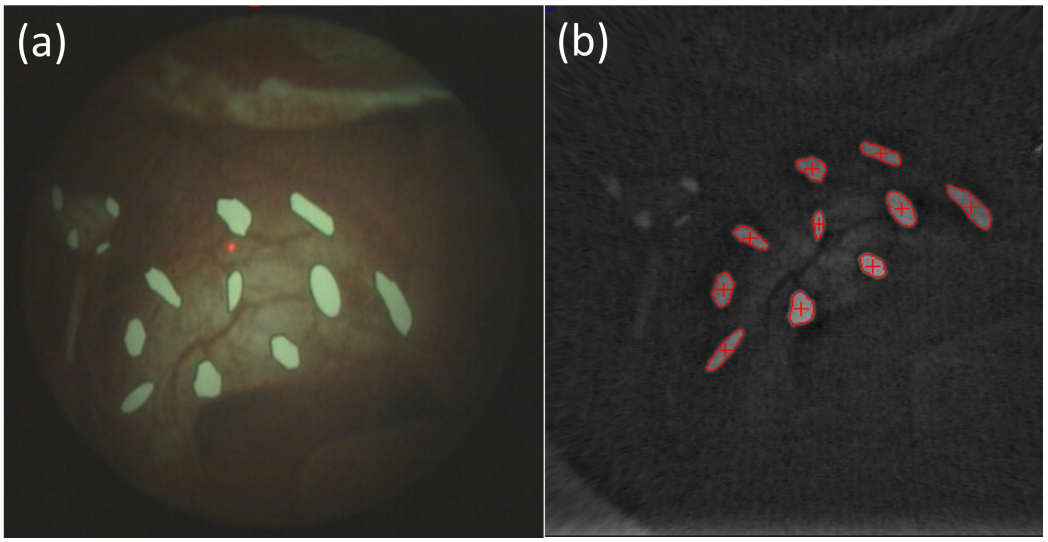

FIGURE 4.10: Figure depicting visual tracking method used for residual cholesteatoma (a) Raw endoscopic view of the simulated image of middle ear cavity (b) Obtained contours (in red) of each selected residual cholesteatoma representing the visual tracking after camera calibration and image processing of the endoscopic image.

4.3.2 Vision-based controller

As evoked earlier, the proposed resection protocol uses the flexible micro-tool inserted via a perforated hole (on the mastoid bone) and integrating a surgical laser source that can eliminate the residual cholesteatoma. In conventional surgery, the surgeon uses an additional bent endoscope inserted in the external ear canal to get visual feedback of the surgical workspace. The configuration of the residual cholesteatoma's laser ablation method is depicted in Figure 4.11. This setup is analogical to enlisted solutions integrating a robotic system with an embedded laser source and vision sensor (endoscope in our case).

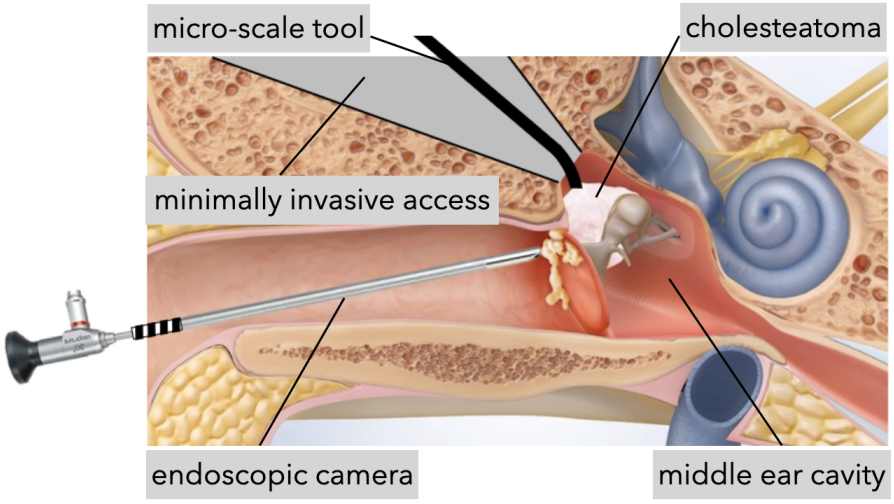

FIGURE 4.11: Example of cholesteatoma growth within the middle ear. Also, one can see the targeted surgical protocol with two accesses to the middle ear cavity.

The image positions of the laser spot and residual cholesteatoma are extracted from the endoscopic image by integrating the previously introduced visual tracking algorithms. Thus, automatic control of the micro-tool's end-effector can be established by integrating a vision-based control method.

Among the different vision-based control strategies reported in the literature during the last 30 years, we opted for an image-based visual servoing (IBVS). This approach is known to be robust and satisfying the requirement of laser surgery [Dahroug et al., 2018a] in terms of accuracy, stability, and dynamics. Note that, the laser ablation we consider, is similar to an *eye-to-hand* configuration in vision-based control theory [Wijesoma et al., 1993], in which the vision sensor (*i.e.*, the rigid endoscope inside the external ear canal) is not embedded on the moving part (*i.e.*, the micro-robot's end-effector).

I this development, the kinematic modeling of the targeted procedure will rely on the same kinematic model as Chapter 2, wherein the RCM position is supposed to be fixed. The simplified model from equation (2.10) is used across this chapter. Figure 4.12 depicts the kinematic model of our proposed automatic residual cholesteatoma ablation.

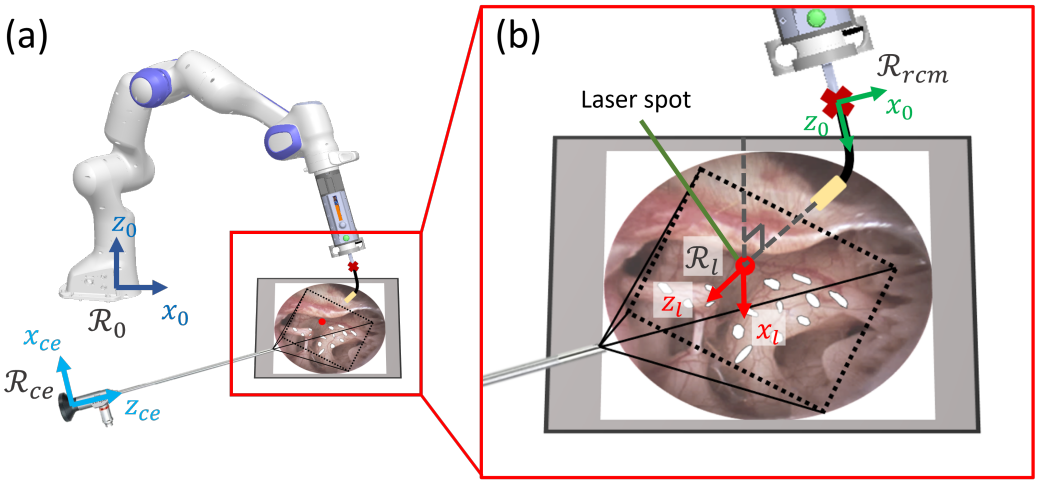

FIGURE 4.12: Kinematic model of the robotic system configured to integrate visual servoing technique, with the associated frames of the rigid endoscope, the RCM point, the laser spot frame, and the robot base frame.

According to [Chaumette and Hutchinson, 2006], the aim of a visual servoing is to control the motion of a dynamic system in order to allow a set of geometric visual features $\mathbf{s}$ ($\mathbf{s} \in \mathbb{R}^k$) defining a robot pose $\mathbf{r}(t) \in SE(3)$ $\big(i.e., \mathbf{s} = \mathbf{s}\big(\mathbf{r}(t)\big)\big)$ to reach a set of desired ones $\mathbf{s}^*$ ($\mathbf{s}^* \in \mathbb{R}^k$), which represent the desired positions. In this chapter, $\mathbf{s}^*$ represents the list of points set defining the path to be followed. Therefore, the visual error $\mathbf{e}$ is defined as follows:

$$\mathbf{e} = \mathbf{s}\big(\mathbf{r}(t)\big) - \mathbf{s}^* \tag{4.1}$$

The time-variation of $\mathbf{s}$ is related to the velocity twist $\mathbf{v}_{ce} = (v_{ce}, \omega_{ce})^\top$ of the camera frame $\mathcal{R}_{ce}$ by $\dot{\mathbf{s}} = \mathbf{L_s}\mathbf{v}_{ce}$, where $\mathbf{L_s} \in \mathbb{R}^{k\times 6}$ is commonly called the *interaction matrix* (or *Jacobian image* in certain papers).

From equation (4.1), the variation of the visual error $\mathbf{e}$ due to the visual sensor velocity is $\dot{\mathbf{e}} = \mathbf{L_s}\mathbf{v}_{ce} - \dot{\mathbf{s}}^*$ (here, $\dot{\mathbf{s}}^* = 0$). If one wants to ensure an exponential decoupled decrease of the error $\mathbf{e}$ ($\dot{\mathbf{e}} = -\lambda\mathbf{e}$), it is possible to express the velocity tensor as follows:

$$\mathbf{v}_{ce} = -\lambda\widehat{\mathbf{L}_\mathbf{s}}^{+}\big(\mathbf{s}(t) - \mathbf{s}^*\big) \tag{4.2}$$

where λ is a control positive gain and $\widehat{\mathbf{L}_\mathbf{s}}^{+}$ $\Big(\widehat{\mathbf{L}_\mathbf{s}}^{+} = \big(\widehat{\mathbf{L}_\mathbf{s}}^{\top}\widehat{\mathbf{L}_\mathbf{s}}\big)^{-1}\widehat{\mathbf{L}_\mathbf{s}}^{\top}\Big)$ is the *Moore-Penrose* pseudo-inverse of the approximated interaction matrix denoted $\widehat{\mathbf{L}_\mathbf{s}}$.

Note that the laser is mounted on a flexible and actuated tool which is in turn mounted on the Panda robot arm as shown in Figure 4.12. And, as explained, the scene is viewed by an external endoscopic system (Figure 4.12(b)) mounted in an *eye-to-hand* configuration. The relation between the robot joint-space velocity $\dot{\mathbf{q}}^*$ and the laser spot's image-space velocity $\dot{\mathbf{s}}$ is then expressed by:

$$\dot{\mathbf{s}} = \lambda(\mathbf{L_s}\,{}^{ce}\mathbf{V}_{rcm}\,{}^{rcm}\mathbf{V}_l\mathbf{J}_{tip})\dot{\mathbf{q}}^* \tag{4.3}$$

where ${}^{ce}\mathbf{V}_{rcm}$ is the spatial motion transform matrix from the camera frame $\mathcal{R}_{ce}$ to the reference frame $\mathcal{R}_{rcm}$. ${}^{ce}\mathbf{V}_{rcm}$ is constant if the camera is considered static and ${}^{rcm}\mathbf{V}_l$ is the spatial motion transform matrix from the robot reference frame $\mathcal{R}_{rcm}$ to the end-effector frame $\mathcal{R}_l$ which can be known from the robot kinematics model (considering that the laser spot is controlled in 2D) [Chaumette, 2020]. The spatial motion transformation matrix is obtained with:

$${}^{ce}\mathbf{V}_{rcm} = \begin{bmatrix} {}^{ce}\mathbf{R}_{rcm} & [{}^{ce}\mathbf{t}_{rcm}]_\times\,{}^{ce}\mathbf{R}_{rcm} \\ 0 & {}^{ce}\mathbf{R}_{rcm} \end{bmatrix} \tag{4.4}$$

where $[{}^{ce}\mathbf{t}_{rcm}]_\times$ is the translation skew matrix.

As for the interaction matrix $\mathbf{L}_s$, it gives the relation between the 3D point $\mathbf{p_{3D}} = (X, Y, Z)$ associated to the camera frame and the 2D projection of this point in the 2D image-plane frame noted $\mathbf{x_{im}} = (x_{im}, y_{im})$ defined as:

$$\begin{cases} x_{im} = \frac{X}{Z} = (u - u_0) * \left(1 + k_{du}r^2\right)/f_x \\ \\ y_{im} = \frac{Y}{Z} = (v - v_0) * \left(1 + k_{du}r^2\right)/f_y \end{cases} \tag{4.5}$$

where (u, v) is the image point coordinates in pixel, (u_0, v_0) is the coordinates of the principal point of the image, (f_x, f_y) is the ratio between the focal length and the size of pixel, k_{du} is the distortion parameter with $r^2 = ((u - u_0)/f_x)^2 + ((v - v_0)/f_x)^2$. Finally $\mathbf{L_s}$ is expressed as follow:

$$\mathbf{L_s} = \begin{bmatrix} -1/Z & 0 & x_{im}/Z & x_{im}y_{im} & -\left(1 + x_{im}^2\right) & y_{im} \\ 0 & -1/Z & y_{im}/Z & 1 + y_{im}^2 & -x_{im}y_{im} & -x_{im} \end{bmatrix} \tag{4.6}$$

with Z the depth of the 3D point. In this study, the depth Z can be assumed as constant since the $x - y$ plane displacement of the robot is not big enough to influence it.

In this work, the laser source or the tool-tip of the micro-scale part will remain normal to the experimental image of the middle ear cavity separated with a distance of 3 cm (cf. Figure 4.12), leading to a 3 dof control of the tool-tip. Within this configuration, the laser spot remains its circular shape and limits the translation motion induced by the angular motion.

4.4 Optimal path generation

The previous section described the integration of vision-based control for our developed system. This section focuses on another crucial development step of the proposed method for residual cholesteatoma resection, *i.e.*, the generation of a path that will let the laser move and cover all areas of infected residual cholesteatoma. The proposed solution is to create a path where the laser spot covers every selected region of residual cholesteatoma optimally, *i.e.*, with the lowest distancial cost. For that, the path of the laser spot is composed of linear portions linking between successive regions of residues (inter-region path) followed by a sine wave portion that cover the residual area (intra-region path). Note that, for the intra-region path strategy, other shapes of line can be applied but are not treated in this study, *e.g.*, zig-zag shaped path [Hu et al., 2018].

4.4.1 Intra-region path generation

The intra-region scanning path is intended to move the laser spot cover the entire area of a residual cholesteatoma. The coverage will of course depend on the geometrical property of this area. As presented in the previous section, the visual tracking method of residual cholesteatoma regions provides the position, the bounding box as well as the contour-points list of each cholesteatoma region. Based on this, Principal Components Analysis (PCA) is used to determine the input points $\mathbf{p}_{in} = (\mathbf{p}_{in}, \mathbf{y}_{in})^\intercal$ and the output points $\mathbf{p}_{out} = (\mathbf{x}_{out}, \mathbf{y}_{out})^\intercal$. These points correspond to the intersection between the first principal axis found by the PCA method and the contour of a given region (see Figure 4.13).

The contours-points that delimit a given cholesteatoma region are defined by $p_i = (x_i, y_i) = [p_1, p_2, ..., p_N]$ with N is the total number of contours-points (represented in the image frame) of the given region. The re-projection p'_i of the contour-points p_i according to the first two principal components is given by:

$$p'_i = \mathbf{A}(p_i - p_c) \tag{4.7}$$

where $p_c = (x_c, y_c)^\intercal$ is the centroid of the considered region which is computed as:

$$p_c = \frac{1}{N}\sum_{i=1}^{N} p_i, \tag{4.8}$$

and $\mathbf{A} \in \mathbb{R}^{2\times 2}$ is the transformation matrix from the original representation to the PCA one. $\mathbf{A}$ is obtained by the computation of the eigenvectors of the covariance matrix $\mathbf{C}$ given by:

$$\mathbf{C} = \begin{pmatrix} var(x_i) & cov(x_i, y_i) \\ cov(y_i, x_i) & var(y_i) \end{pmatrix} \tag{4.9}$$

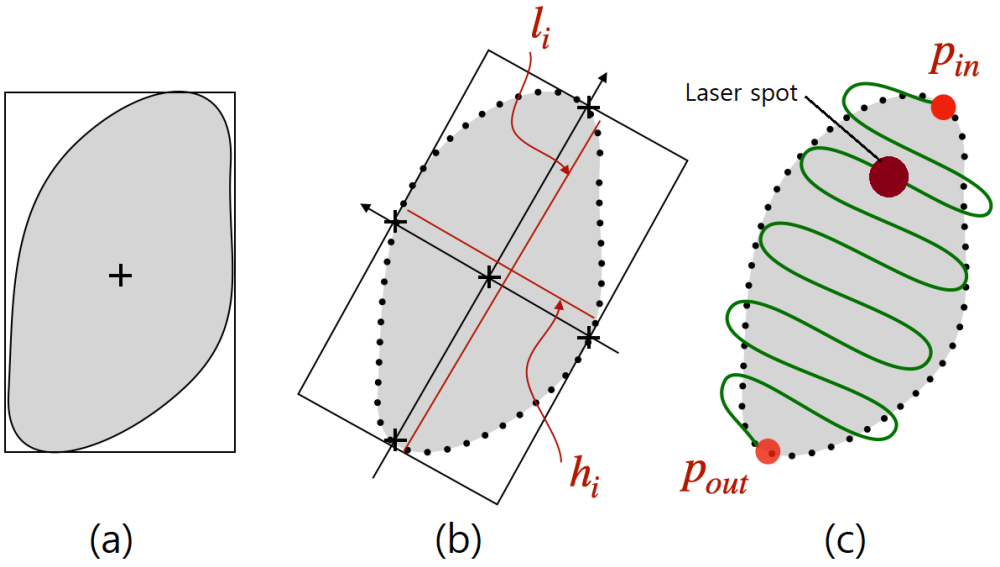

FIGURE 4.13: Intra-regions path generation step. (a) Extraction of contour points list (b) Extraction of geometrical parameters (major axis, centroid) (c) Drawing of sinusoidal path to cover the residual zone where the laser spot has to follow.

where *var* and *cov* represent the variance and the covariance of the contour-point list, respectively.

While the PCA gives the main two principal axes of a residual cholesteatoma area, following geometrical properties can be derived:

- p_{in}: The input point from which the laser spot enter on the cholesteatoma region,
- p_{out}: The output point from which the laser spot should exit once the cholesteatoma region has been completely covered,
- h_i: The maximum width for i-th cholesteatoma region,
- l_i: The length for i-th cholesteatoma region.

Now, using these extracted parameters, it is possible to define the scanning curve that allows covering the whole surface of the residual cholesteatoma region. According to the diameter of the laser spot (generally from 50μm to 200μm) [Fichera, 2016], different scanning curves can be candidates. In this work, we opted for a simple sinusoidal curve defined by the following relationship:

$$y' = h_i \sin\left(\frac{2\pi}{d_{laser}} x'\right) \qquad \text{with } x' \in [0, l_i] \tag{4.10}$$

with d_{laser} is the diameter of the laser spot (Figure 4.14).

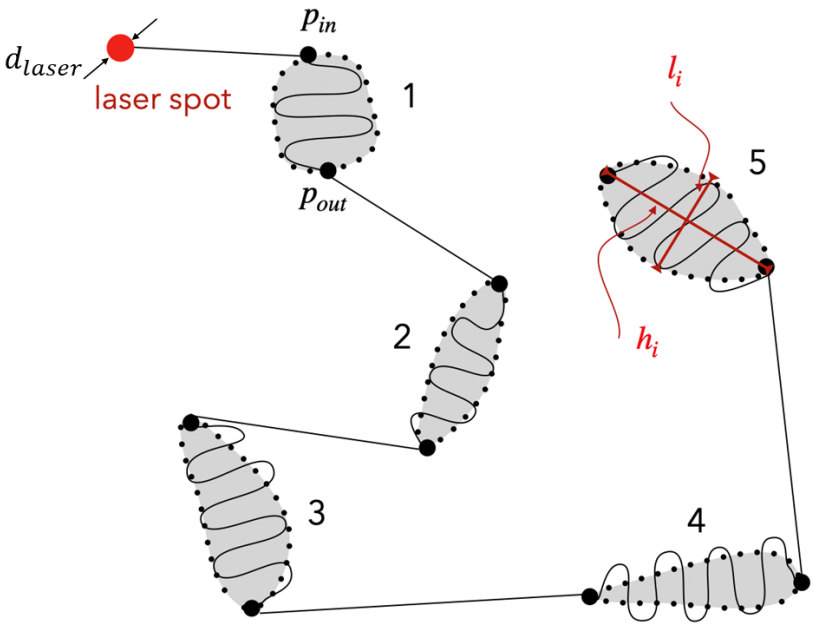

FIGURE 4.14: Illustration of the generation of a scanning path to be followed by the laser spot in case of 5 residual cholesteatoma regions.

Finally, the coordinates of each discretized sinusoidal curve $\tilde{p}_i = (\tilde{x}', \tilde{y}')$ are expressed in the image frame $\mathcal{R}_I$ by the inverse of (4.7):

$$\tilde{p}_i = \mathbf{A}^{\intercal}\tilde{p}_i' + p_c \tag{4.11}$$

4.4.2 Inter-region path generation

The last step of the design of the whole scanning path consists of the connection between the cholesteatoma regions. As mentioned above, the path should be as short and accurate as possible. This can be associated with a typical optimization problem, widely studied in transportation theory, which can be addressed by the well-known Traveling Salesman Problem (TSP) [Lawler, 1985]. In this study, we proposed an adaptation of the traditional TSP algorithm by adding a new condition during the computation of the scanning path of a set of locations. The considered set of 2D positions includes: the current position of the laser spot $p_l = (x_l, y_l)$ and a pair of points that forms the input and output points of each region, *i.e.*, $\mathbf{p}_{in} = (\mathbf{x}_{in}, \mathbf{y}_{in})$, $\mathbf{p}_{out} = (\mathbf{x}_{out}, \mathbf{y}_{out})$, respectively. At this stage, the TSP algorithm does not yet know the input and output points of each region. To formalize the optimization problem (Figure 4.15), we consider $(2n + 1)$ "nodes"comprising the current laser position and the input and output positions of all the n regions.

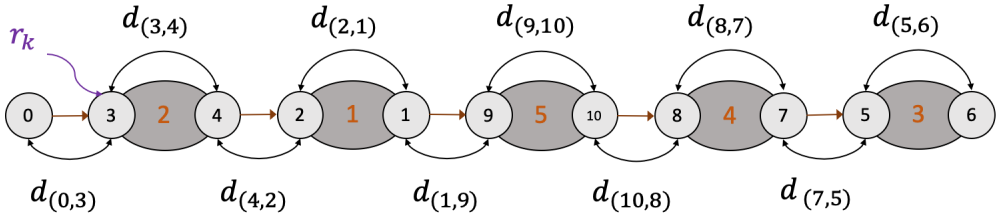

FIGURE 4.15: Construction of the TSP problem as a graph of nodes. Here, considered nodes are the laser spot position and the pair of points that forms the input and output points of each individual cholesteatoma region (5 in total).

To solve the optimization problem, we start by constructing the whole graph of nodes. This is formalized by the following method:

- Each region is assigned a number k, $k \in [1, 2, \cdots, n]$,
- For each region, the two extremities (*i.e.*, the future input and output points are assigned the number r_k via equation (4.12),
- Systematically, a "0" represents the first of the laser spot.

$$\begin{cases} r_k = 2k - 1 \\ r_{k+1} = 2k \end{cases} \quad \text{for} \quad k = 1, \cdots, n \tag{4.12}$$

For example, in Figure 4.15, for the region (2), the associated nodes are (3) and (4). The next step is to construct a sequence of nodes $S = (s_0, s_1, s_2, \cdots, s_{2n})$ defining the laser scanning path. For that, for each pair of nodes, a Cartesian distance d is computed. The algorithm then attempts to find the sequence that offers the shortest path to connect all nodes. This minimum distance $d_{\min}$ is obtained as follows:

$$d_{\min} = \min \sum_{i=0}^{2n} d_{(s_i, s_{i+1})} \tag{4.13}$$

Based on the traditional TSP problem, we added supplementary conditions corresponding to the study case, *i.e.*, 1) the first node s_0 is always the laser location, 2) successive pairs of nodes $\big((s_1, s_2), (s_3, s_4), ...\big)$ are belong to the same region k, and 3) the absolute difference value between the assigned number of each pair of nodes must be 1. These conditions can be formalized as follows:

$$\begin{array}{lccll} 1) & s_0 & = & 0 & \\ 2) & \frac{1+s_{2i-1}+s_{2i}}{4} & = & k & \text{for} \quad i = 1, 2, \cdots, n. \\ 3) & |s_{2i-1} - s_{2i}| & = & 1 & \text{for} \quad i = 1, 2, \cdots, n \end{array}$$

An example of the result of this algorithm can be seen in Figure 4.15. In this example, five regions are considered making a total of 11 nodes organized as a sequence $S = (0, 3, 4, 2, 1, 9, 10, 8, 7, 5, 6)$, which gives the shortest scanning path to cover the considered residual cholesteatoma regions.

At this stage of development, the entire laser path in the middle ear cavity is constructed. It includes sinusoidal parts where the surgical laser is activated to ablate the cholesteatoma tissues and other straight-line segments parts where only the aiming (visible) laser is activated.

4.5 Experimental validation

In this section, the above proposed methods are tested. For that, we rely on the developed robotic setup with a slightly modified configuration for this experiment, as depicted in Figure 4.16. For reminder, the setup includes a Panda robot with 7 DOF and a 2 DOF actuated and flexible mechanism (here a miniature fiberscope). The laser fiber source is fixed along the flexible fiberscope. An external rigid fiberscope (from KARL STORZ) equipped with an integrated light source is used to visualize the scene, *i.e.*, both the laser spot and the residual cholesteatoma. The endoscopic camera offers images of a resolution of 768×576 pixels at the frame rate of 25 images/second.

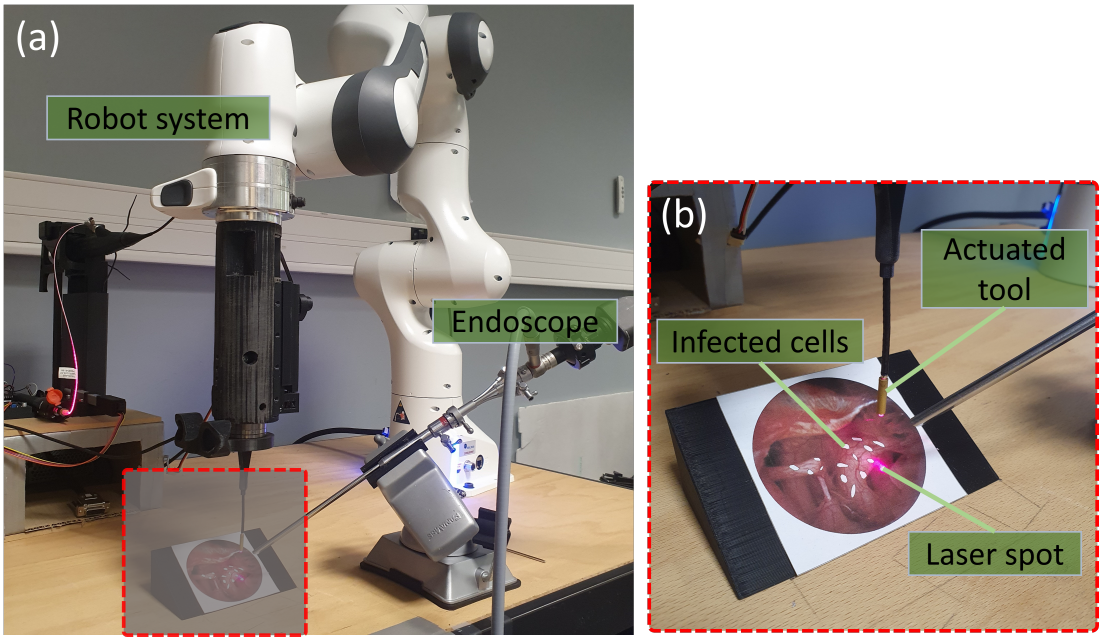

FIGURE 4.16: Photography of the designed experimental setup: (a) global view of the whole robotic system (b) a zoom-in on the distal part of the flexible tool embedding the laser source.

Similar to the achievements described in Chapter 2 and Chapter 3, the developed image processing, path generation, and control methods were also implemented in ROS framework. Then, we set up an evaluation scenario that mimics the residual cholesteatoma's laser ablation after a mechanical resection of the significant parts of infected tissues. To do so, a simulating image depicting the middle ear cavity and the remaining cholesteatoma tissue after the first phase of intervention is added to the setup at a location consistent with the middle ear cavity anatomy. Note that the experimental setup is scaled up with a ratio of 1:3.

4.5.1 Results and analysis

Various trials with different numbers and positions of simulated residual cholesteatoma were conducted. Three main points are evaluated in this phase: the performance of the vision-based control of the laser spot during the path following, the generation of the optimized path, and the coverage of residual cholesteatoma by the laser spot.

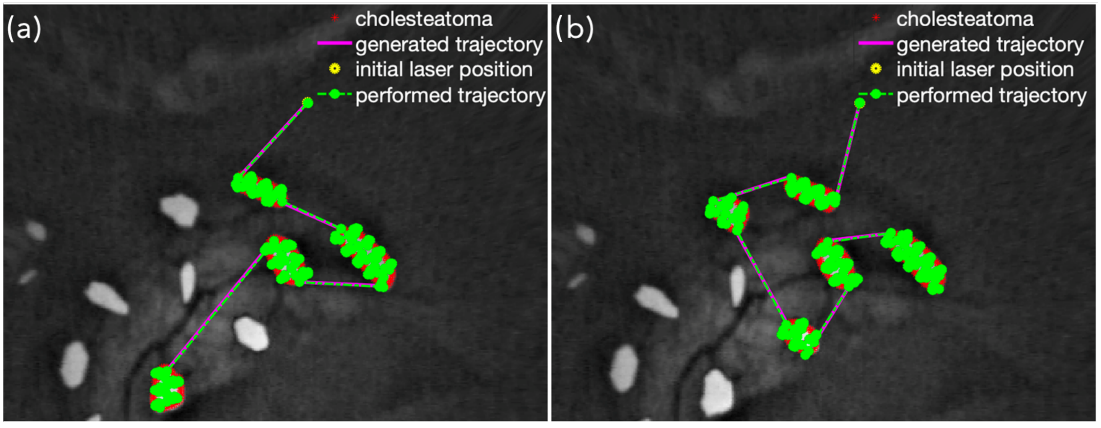

FIGURE 4.17: Examples of performed paths (in green): (a) with 4 cholesteatoma regions and (b) with 5 residual cholesteatoma.

The performance of the vision-based steering method is analyzed during the path following. The behavior of the laser spot motion as well as the accuracy of the image-based path tracking is evaluated experimentally. Figure 4.17 shows example of generated (in magenta) and performed (in green) paths. As can be highlighted, both performed inter-region (linear portions) and intra-region (sinusoidal portions) paths are almost superposed with the desired ones.

The good path following accuracy is confirmed by the tracking errors for different achieved paths summarized in Table 4.1. The average error $\bar{e}$ for each evaluation is estimated to $85\mu m$ (with a STD of about $25\mu m$) regardless of the number of considered residual cholesteatoma regions, *e.g.*, 3, 4 or 5. The mean error value is in accordance

with the threshold set as 1.0 px (120 μm), wherein the desired position is considered as reached when the error is below the threshold.

Test	Number of Regions	Mean Error ($\bar{e}$) (μm)	STD (μm)	Cover (%)
1	3	83.72	27.09	99.38
2	3	83.33	26.98	97.77
3	4	77.90	27.87	98.71
4	4	81.40	27.63	96.62
5	5	86.05	26.51	98.01
6	5	87.63	26.59	99.00
7	3	89.78	22.21	97.82
8	3	90.17	21.35	97.77
9	4	87.31	25.60	98.37
10	4	90.60	22.79	97.82
	average	85.78 μm	25.46 μm	98.12%

TABLE 4.1: Accuracy analysis for the paths generated for different scenarios with 3, 4 or 5 residual cholesteatoma regions.

The norm of the visual servoing error decay was recorded for several performed paths and plotted in Figure 4.18. The latter shows that the regulation of the error is linear instead of the traditional exponential decay obtained in visual servoing. This phenomenon can be explained by the motion of the actuated fiberscope that carries the laser source. As noticed in Chapter 1, the fiberscope is actuated by wires whose triggering mechanism is located at the base, and whose low-level control relies on an approximated linear function while the hysteresis induces non-linear property. Thus, movements of the end-effecting part of the fiberscope are induced with a small permanent flexion angle error. To minimize the problem caused by the angle error, the maximum velocity was set at 0.5 mm/s, thus decreasing the risk of instability.

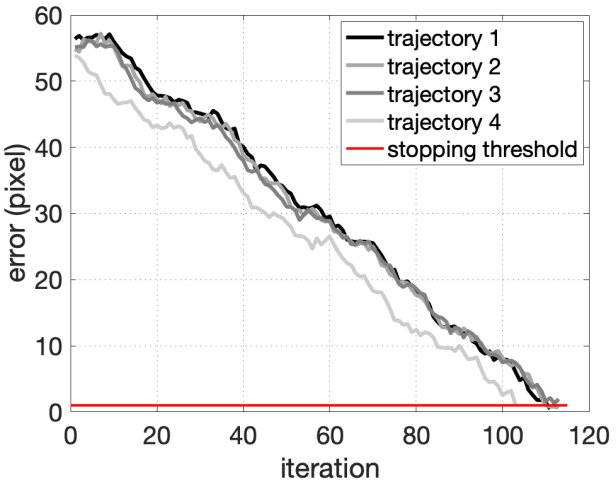

FIGURE 4.18: Example of error decay versus iterations (each iteration takes 100ms) for different achieved paths. The convergence criteria is fixed to 1 pixel corresponding to 0.12mm.

The detection and visual tracking of the remaining infected tissues as well as the path generation, were also evaluated. Different numbers and positions of residual cholesteatoma were considered. The generated scanning paths (inter and intra-region) are the results of the developed augmented TSP algorithm in which the minimal distance cost is retained from every possible path. Figure 4.19 shows only the retained minimized paths which fit perfectly the optimal scanning problem in terms of path length minimization.

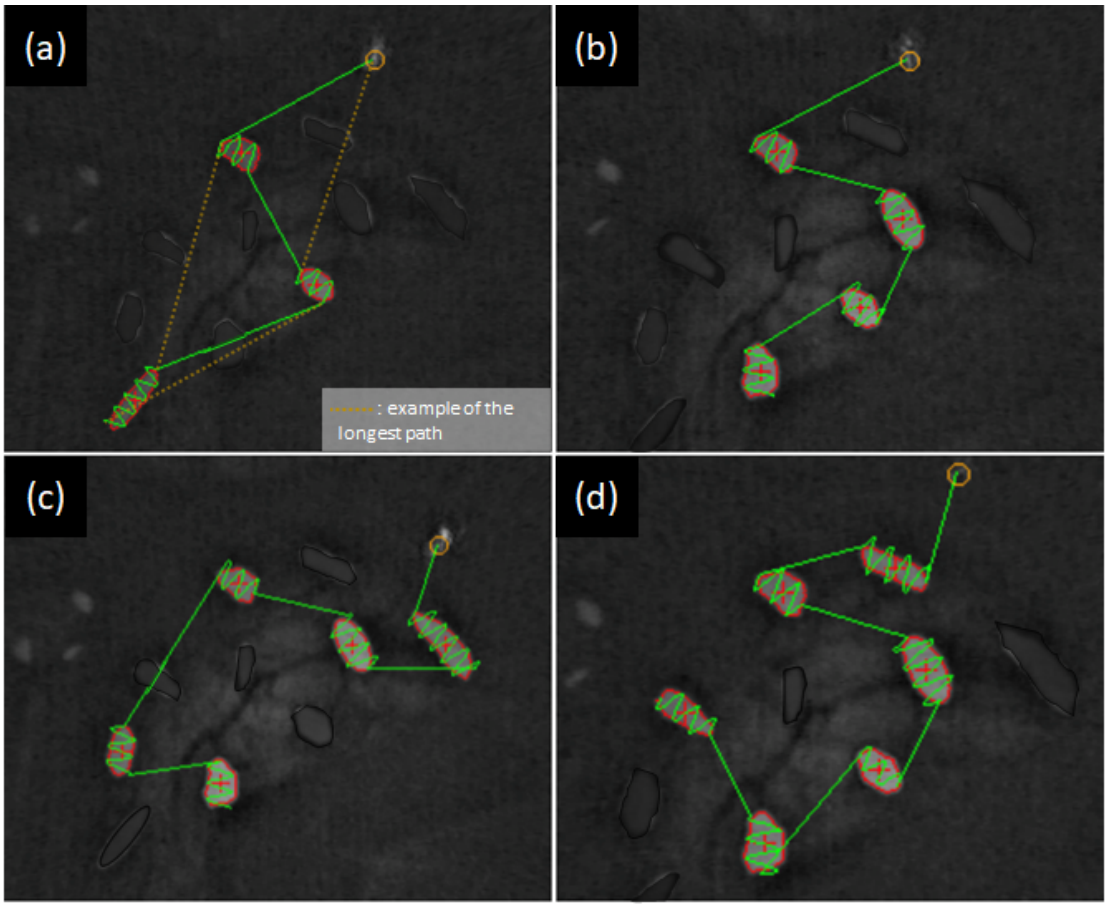

FIGURE 4.19: Examples of generated scanning paths: (a) 3 cholesteatoma regions to be ablated and an example of the longest path (b) 4 regions (c) 5 regions (d) 6 regions.

The last evaluation criterion consisted of the ability to sufficiently cover the cholesteatoma regions with the laser spot to carbonize the infected tissue completely. This parameter is calculated as an overlap rate of all positions of the laser spot (the laser spot diameter is fixed to $d_{laser} = 5$ pixels, equivalent to 600 μm) over the total surface of the treated region. Note that the experimental setup was scaled 3 times bigger than the considered real condition. As mentioned above, a real laser tool used in micro-surgery has a maximal diameter up to 200 μm.

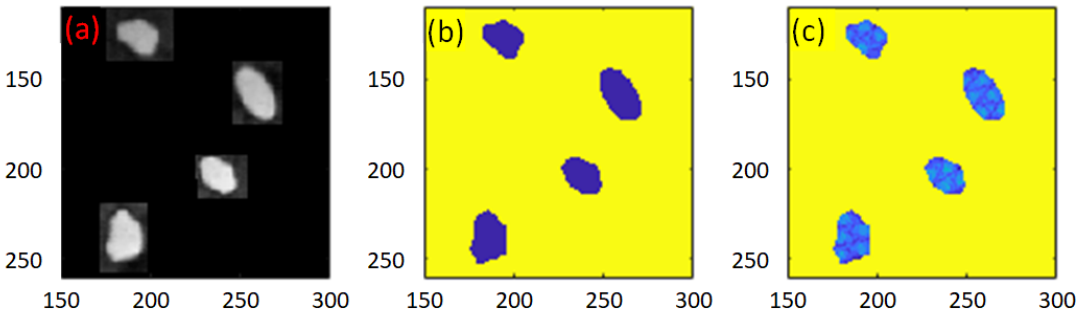

FIGURE 4.20: Example of coverage computational process (a) Extraction of residual cholesteatoma region (b) Converted intensity pixel image (c) Updated intensity image with respected laser spot position

Figure 4.20 depicts the method used to compute the coverage rate of the cholesteatoma region by the laser spot. The endoscopic image was first filtered to get the selected cholesteatoma region and converted into an intensity scaled pixel graph. Then, at every position where the laser spot has stopped, a constant value was added for each pixel inside the laser (Figure 4.20 (c)). Finally, the total number of pixels with the value 0 and the total number of pixels corresponding to the cholesteatoma region are used to compute the coverage rate.

For the ten tests reported in Table 4.1, the average covering rate is estimated to be 98.12%, which almost perfectly meets the specifications of laser surgery. This rate can also be improved by reducing the period of the sinusoidal path, *i.e.*, by changing the periodic parameter of the sine wave or studying other curves (path) that could more efficiently cover the cholesteatoma regions.

4.6 Conclusion

This chapter began by presenting a brief use case of image-based robot control techniques. It describes the advantage of integrating such functions in a micro-surgical context. Then, this chapter proposed a general methodology to integrate an image-based robot control and an optimal path generator to cover the simulating ablation process. The developed solution was tested in an experimental setup mimicking the surgical configuration of the targeted treatment for residual cholesteatoma.

The main contribution of this chapter is the integration of an *eye-to-hand* vision-based control method to steer a laser beam applied to tissue ablation. The developed visual servoing controller allows to steer the laser spot across the detected residual cholesteatoma regions.

This study also proposes an innovative solution to handle the issue of remaining cholesteatoma, *i.e.*, an automatic function that generates an optimal path linking the initial laser spot position to all residual cholesteatoma areas. The generation of an optimal path can be done thanks to an augmented TSP solving algorithm which computes the shortest path allowing a time-efficient resection of the residual cholesteatoma region.

Future work will be to apply and test the developed functions in experimental conditions close to a real clinical case of middle ear surgery. An improvement of the tool is also required, *i.e.*, miniature surgical tools, surgical laser, and fiber-optic camera will replace the current flexible fiberscope.

Conclusion and Perspectives

Contents

General conclusion

This doctoral research work consisted in creating an enhanced surgical robotic system dedicated to cholesteatoma resection. Current surgery can be described as:

- invasive: due to canal down technique applied in major cases
- difficult: due to residual cholesteatoma which causes second operation
- exhausting: due to high load of mental concentration to the surgeon for operating (manipulating a rigid tool) inside a visually obstructed workspace

Thus, the main objective set by the project μRoCS was to develop a robot assisted cholesteatoma resection involving a laser-embedded flexible micro-tool fixed on a tool handling robotic device.

This study started with an overview on the clinical context of cholesteatoma disease and robotic systems dedicated to otological surgery. It also presents the requirements and specifications for designing and implementing a robotic system to deal with the cholesteatoma surgery. The main conclusion drawn from this analysis was to create a novel robotic system which consists of the combination of a macro-scale robotic arm and a flexible micro-scale surgical tool (where a surgical laser can be embedded on). The

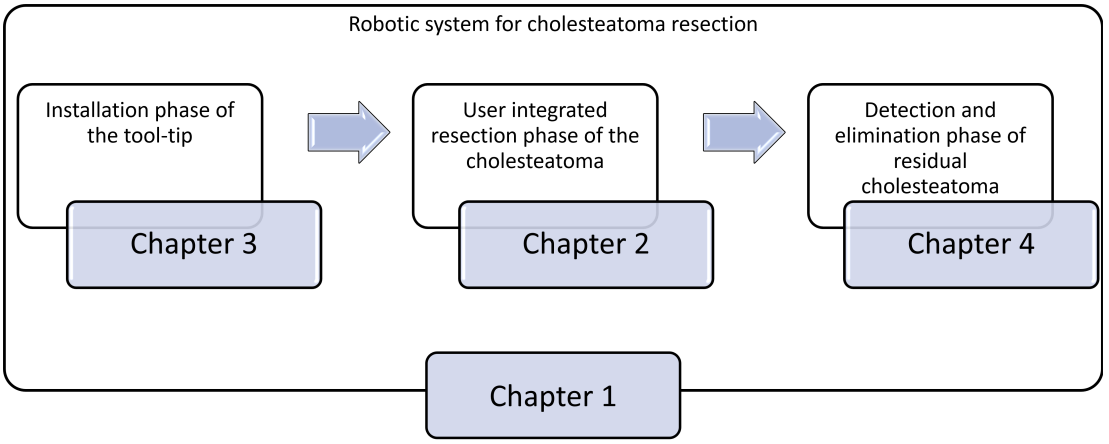

FIGURE 4.21: Surgical protocol for the new robot-assisted cholesteatoma resection and its related contributions.

method of conception was then detailed, treating both the mechatronic design and the control schemes used to command the designed macro/micro-system.

The next objective was to integrate the surgeon inside the control process. To do so, two main control strategies frequently used in surgical robotic have been studied. It is the end-frame teleoperation mode and the comanipulation mode. These two control methods were adapted to be functional for cholesteatoma resection. The teleoperation was implemented from the entry point of the middle ear cavity (*i.e.*, the RCM located inside the drilled hole obtained by mastoidectomy) to the micro-scale tool-tip. It has 5 DOF, 3 rotations at the RCM and 2 DOF with the translation and the flexion of the micro-tool, all controlled with a Phantom Omni joystick. The comanipulation was adapted to middle ear surgery, engaging 6 DOF at the RCM in comanipulation and the same 2 DOF of the micro-tool by teleoperation using a lab-made joystick attached on the robot arm. Both control strategies have been compared to a manual control of the fibroscope (in which the operator manipulates a simple 2 DOF fibroscope by hand). A task which consisted of pointing tool-tip in 5 different positions has been introduced to validate the enhancement of positioning precision. Through multiple quantitative parameters, it has been proved that the proposed solutions led to better results.

The second part of this thesis focused on the early phase of robot-assisted surgery, the tool positioning and installation. In a general look of existing solutions, one can notice that the positioning approaches are divided into 2 categories. Manual guiding of the robotic system in which the surgeon chooses the point of interest by himself and assisted guiding of the robot using a camera attached to the robot and a vision-based control to precisely position the tool. Each solution had its advantage and drawbacks; it can be noticed that manual guiding was much simpler from the computational point of view and took less time to position. In opposition, the positioning precision was better in assisted guiding. Thus, the challenge was to find an intermediate solution

which includes only the advantages of both solutions. That is why, we proposed shared control methods combining force/position control with a vision-based control. Through an experimental setup, a positioning task was performed with all the proposed controllers. The comparative analysis showed that parallel hybrid approaches are much more efficient than the external hybrid ones and the manual ones, in almost all the evaluation criteria (precision, behavior, etc...).

After working on the early phase and middle phase of the cholesteatoma surgery, the last part of this thesis focused on the detection and resection of residual cholesteatoma. To begin, the last chapter described the residual cholesteatoma and its consequence if it is not entirely destroyed. To oppose to the critical result of this issue, a solution consisting of integrating a vision-based framework was proposed. The first part was to detect and automatically track the cholesteatoma residues. The visual tracking function was then used to generate an optimal path in which the laser spot has to follow. An automatic path-following was then implemented thanks to a visual servoing technique under an eye-to-hand configuration. An experimental setup was installed to check the performance of the proposed solution. It has been noticed that the laser steering performed well with a satisfying precision of $85\mu m$. The total area of residual cholesteatoma covered by the laser path was computed. The computed coverage was above 98%, a pledging result for this developed technique.

To summarize, this research proposed an innovative solution to manage all the issue of robot-assisted cholesteatoma resection. The first was the control technique of robotic system dedicated to cholesteatoma ablation increasing the precision, safety and speed. The second was a shared control method to easily install the tool before initiating the operation. The last was an automatic function which generates the shortest path covering all residual cholesteatoma areas and a control of the laser spot using a vision-based controller.

Limitations and perspectives

There are various tracks to follow-up our work, mostly application issues. The first perspective is the integration of a real micro-scale tool dedicated to cholesteatoma [Nguyen et al., 2021]. The developed system will have an actuated flexible fibroscope mimicking a functional micro-tool currently under development at FEMTO-ST Institute. The designed micro-tool is a hybrid Concentric Tube Robot (CTR) with a tendon-driven terminal wrist (as depicted in Figure 4.22A). It has 4 DOF and can carry optical fibers for surgical laser and biopsy using OCT imaging technique (attached by an end cap at the distal part of the micro-tool as seen on Figure 4.22B). The integration of the novel tool will need a re-computation of the macro/micro system kinematic model and a re-design of the embedded micro-joystick accounting for the number and type of the tool DOF.

FIGURE 4.22: Scheme of hybrid CTR developed at FEMTO-ST (a) Hybrid CTR is built according to the simulation results. (b) The end cap to fix the tendon and the laser OF at the distal end [Nguyen et al., 2021].

The second short-term perspective is the vision-based control of the micro-tool using OCT image as visual feedback. An optical biopsy tool engaging OCT method and fluorescence imaging (integratable to the flexible micro-tool) is currently under development at CHU Besanǫn as a solution to detect residual cholesteatoma. The OCT probe must move across the surface of middle ear to detect and map all positions where residual cholesteatoma remains. Besides, the positioning of the micro-tool to residual cholesteatoma via visual servoing with OCT image feedback has been studied in the literature [Dahroug et al., 2020a, Ourak et al., 2016a, Ourak et al., 2016b, Ourak et al., 2019]. The implementation of such control methods seems necessary for our developed robotic system. An interesting work of Zhang and Nageotte investigated a potential solution where vision-based controllers are integrated [Zhang et al., 2021]. The study deals with an image-guided flexible robot control for OCT image based real-time biopsy. To get a precise control of the probe, two image-based controllers were integrated, one is a contact controller using the OCT probe image and another is a tool-tracking controller using an external camera. Implementing this function into our context would be a solution to complete the automatic resection function of residual cholesteatoma based on OCT and fluorescence imaging.

The third perspective is the experimental validation of the finalized robotic system. The developed functions in this study were tested through preliminary experiments. Although results have shown an enhancement of control precision, a deeper study engaging real cholesteatoma surgery has to be performed. That is why future work will be devoted to evaluate the developed functions in experimental conditions close to a real clinical case of middle ear surgery, with senior and junior surgeons recruited to test the benefit of the developed robotic solution. A comparative study between the recent surgical protocol engaging a simple robotic tool handler and the novel one integrating our developed robotic solution is considered as essential to check the validity of our work.

A last long-term perspective to be studied is to assess the applicability of other flexible micro-tool dedicated to other types of middle ear surgeries. The overview of

ENT surgery in Chapter 1 showed that other possible ENT interventions (*e.g.*, cochlear implant surgery, other types of laser surgery in the middle ear cavity) are subject to be assisted with robotic solution. Thus, new flexible micro-tool dedicated to, *e.g.*, hearing organ replacement, would be an interesting point of study to broaden the developed system to a general middle ear surgical tool.

Appendices

Appendix A

Formulation of Jacobian

A.1 Identification of the Jacobian from the kinematic model

To find the Jacobian model from the kinematic model, we use the geometrical properties or the transformation matrices which are defined in Section 2.2. Then, following formula is applied to fill each column of the Jacobian.

	Prismatic	Revolute
Linear	$\mathbf{R}_{i-1}^{0} \begin{bmatrix} 0 \\ 0 \\ 1 \end{bmatrix}$	$\mathbf{R}_{i-1}^{0} \begin{bmatrix} 0 \\ 0 \\ 1 \end{bmatrix} \times \left(\mathbf{t}_{n}^{0} - \mathbf{t}_{i-1}^{0}\right)$
Rotational	$\begin{bmatrix} 0 \\ 0 \\ 0 \end{bmatrix}$	$\mathbf{R}_{i-1}^{0} \begin{bmatrix} 0 \\ 0 \\ 1 \end{bmatrix}$

For example, the Jacobian $\mathbf{J} \in \mathbb{R}^{6\times 9}$ is found by:

$$\mathbf{J} = \begin{pmatrix} \mathbf{R}_{0}^{0} \begin{bmatrix} 0 \\ 0 \\ 1 \end{bmatrix} \times \left(\mathbf{t}_{9}^{0} - \mathbf{t}_{1}^{0}\right) & \mathbf{R}_{1}^{0} \begin{bmatrix} 0 \\ 0 \\ 1 \end{bmatrix} \times \left(\mathbf{t}_{9}^{0} - \mathbf{t}_{2}^{0}\right) & \cdots & \cdots & \cdots & \cdots & \cdots & \mathbf{R}_{7}^{0} \begin{bmatrix} 0 \\ 0 \\ 1 \end{bmatrix} & \mathbf{R}_{8}^{0} \begin{bmatrix} 0 \\ 0 \\ 1 \end{bmatrix} \times \left(\mathbf{t}_{9}^{0} - \mathbf{t}_{8}^{0}\right) \\ \mathbf{R}_{0}^{0} \begin{bmatrix} 0 \\ 0 \\ 1 \end{bmatrix} & \mathbf{R}_{1}^{0} \begin{bmatrix} 0 \\ 0 \\ 1 \end{bmatrix} & \cdots & \cdots & \cdots & \cdots & \cdots & \begin{bmatrix} 0 \\ 0 \\ 1 \end{bmatrix} & \mathbf{R}_{8}^{0} \begin{bmatrix} 0 \\ 0 \\ 1 \end{bmatrix} \end{pmatrix} \tag{A.1}$$

A.2 Formulation of the Jacobian $\mathbf{J}^*$

The presented Jacobian $\mathbf{J}^*$ is obtained directly from the derivative of the transformation matrices taken from the geometrical model of the developed system detailed from A.1.

$$\mathbf{J}^* = \begin{pmatrix} J_{11}^* & J_{12}^* & J_{13}^* & J_{14}^* & J_{15}^* \\ J_{21}^* & J_{22}^* & J_{23}^* & J_{24}^* & J_{25}^* \\ J_{31}^* & J_{32}^* & J_{33}^* & J_{34}^* & J_{35}^* \\ J_{41}^* & J_{42}^* & J_{43}^* & J_{44}^* & J_{45}^* \\ J_{51}^* & J_{52}^* & J_{53}^* & J_{54}^* & J_{55}^* \\ J_{61}^* & J_{62}^* & J_{63}^* & J_{64}^* & J_{65}^* \end{pmatrix}$$

$J_{11}^* = 0$
$J_{12}^* = c(\beta)(d_{9b} + d_{9t}c(k_9l_9) + s(k_9l_9)/k_9) + \lambda_8 c(\beta) + s(\beta)s(\gamma)((c(k_9l_9) - 1)/k_9 - d_{9t}s(k_9l_9))$
$J_{13}^* = -c(\beta)c(\gamma)((c(k_9l_9) - 1)/k_9 - d_{9t}s(k_9l_9))$
$J_{14}^* = s(\beta)$
$J_{15}^* = c(\beta)s(\gamma)((c(k_9l_9) - 1)/{k_9}^2 + (ks(k_9l_9))/k_9 + d_{9t} * l_9c(k_9l_9)) - s(\beta)(s(k_9l_9)/{k_9}^2 - (l_9c(k_9l_9))/k_9 + d_{9t} * ks(k_9l_9))$

$J_{21}^* = -((c(k_9l_9) - 1)/k_9 - d_{9t}s(k_9l_9))(c(\gamma)s(\alpha) + c(\alpha)s(\beta)s(\gamma)) - c(\alpha)c(\beta)(d_{9b} + d_{9t}c(k_9l_9) + s(k_9l_9)/k_9) - \lambda_8 c(\alpha)c(\beta)$
$J_{22}^* = s(\alpha)s(\beta)(d_{9b} + d_{9t}c(k_9l_9) + s(k_9l_9)/k_9) + \lambda_8 s(\alpha)s(\beta) - c(\beta)s(\alpha)s(\gamma)((c(k_9l_9) - 1)/k_9 - d_{9t}s(k_9l_9))$
$J_{23}^* = -((c(k_9l_9) - 1)/k_9 - d_{9t}s(k_9l_9))(c(\alpha)s(\gamma) + c(\gamma)s(\alpha)s(\beta))$
$J_{24}^* = -c(\beta)s(\alpha)$
$J_{25}^* = c(\beta)s(\alpha)(s(k_9l_9)/{k_9}^2 - (l_9c(k_9l_9))/k_9 + d_{9t} * ks(k_9l_9)) - (c(\alpha)c(\gamma) - s(\alpha)s(\beta)s(\gamma))((c(k_9l_9) - 1)/{k_9}^2 + (ks(k_9l_9))/k_9 + d_{9t} * l_9c(k_9l_9))$

$J_{31}^* = ((c(k_9l_9) - 1)/k_9 - d_{9t}s(k_9l_9))(c(\alpha)c(\gamma) - s(\alpha)s(\beta)s(\gamma)) - c(\beta)s(\alpha)(d_{9b} + d_{9t}c(k_9l_9) + s(k_9l_9)/k_9) - \lambda_8 c(\beta)s(\alpha)$
$J_{32}^* = c(\alpha)c(\beta)s(\gamma)((c(k_9l_9) - 1)/k_9 - d_{9t}s(k_9l_9)) - \lambda_8 c(\alpha)s(\beta) - c(\alpha)s(\beta)(d_{9b} + d_{9t}c(k_9l_9) + s(k_9l_9)/k_9)$
$J_{33}^* = -((c(k_9l_9) - 1)/k_9 - d_{9t}s(k_9l_9))(s(\alpha)s(\gamma) - c(\alpha)c(\gamma)s(\beta))$
$J_{34}^* = c(\alpha)c(\beta)$
$J_{35}^* = -(c(\gamma)s(\alpha) + c(\alpha)s(\beta)s(\gamma))((c(k_9l_9) - 1)/{k_9}^2 + (ks(k_9l_9))/k_9 + d_{9t} * l_9c(k_9l_9)) - c(\alpha)c(\beta)(s(k_9l_9)/{k_9}^2 - (l_9c(k_9l_9))/k_9 + d_{9t} * ks(k_9l_9))$

$J_{41}^* = 1$
$J_{42}^* = 0$
$J_{43}^* = s(\beta)$
$J_{44}^* = 0$

$J^*_{45} = l_9 c(\beta) c(\gamma)$

$J^*_{51} = 0$
$J^*_{52} = c$
$J^*_{53} = -c(\beta) s(\alpha)$
$J^*_{54} = 0$
$J^*_{55} = l_9 c(\alpha) s(\gamma) + l_9 c(\gamma) s(\alpha) s(\beta)$

$J^*_{61} = 0$
$J^*_{62} = s(\alpha)$
$J^*_{63} = c(\alpha) c(\beta)$
$J^*_{64} = 0$
$J^*_{65} = l_9 s(\alpha) s(\gamma) - l_9 c(\alpha) c(\gamma) s(\beta)$

Bibliography

[Adjigble et al., 2019] Adjigble, M., Marturi, N., Ortenzi, V., and Stolkin, R. (2019). An assisted telemanipulation approach: combining autonomous grasp planning with haptic cues. In *2019 IEEE/RSJ International Conference on Intelligent Robots and Systems (IROS)*, pages 3164–3171. *2 citations page 64 and 67*

[Alper, 2004] Alper, C. M. (2004). *Advanced therapy of otitis media*. PMPH-USA. *Cited page 13*

[Amitha and Narayanan, 2021] Amitha, I. and Narayanan, N. (2021). Improved vehicle detection and tracking using yolo and csrt. In *Communication and Intelligent Systems*, pages 435–446. Springer. *Cited page 89*

[Anderson and Spong, 1988] Anderson, R. J. and Spong, M. W. (1988). Bilateral control of teleoperators with time delay. In *Proceedings of the 1988 IEEE International Conference on Systems, Man, and Cybernetics*, volume 1, pages 131–138. IEEE. *Cited page 34*

[Andreff and Tamadazte, 2016] Andreff, N. and Tamadazte, B. (2016). Laser steering using virtual trifocal visual servoing. *The International Journal of Robotics Research*, 35(6):672–694. *3 citations page v, 84, and 87*

[Aquino et al., 2011] Aquino, J. E. A. P. d., Cruz Filho, N. A., and Aquino, J. N. P. d. (2011). Epidemiology of middle ear and mastoid cholesteatomas: study of 1146 cases. *Brazilian journal of otorhinolaryngology*, 77(3):341–347. *Cited page 13*

[Arata et al., 2019] Arata, J., Fujisawa, Y., Nakadate, R., Kiguchi, K., Harada, K., Mitsuishi, M., and Hashizume, M. (2019). Compliant four degree-of-freedom manipulator with locally deformable elastic elements for minimally invasive surgery. In *2019 International Conference on Robotics and Automation (ICRA)*, pages 2663–2669. *Cited page 60*

[Azizian et al., 2014] Azizian, M., Khoshnam, M., Najmaei, N., and Patel, R. V. (2014). Visual servoing in medical robotics: a survey. part i: endoscopic and direct vision imaging–techniques and applications. *The international journal of medical robotics and computer assisted surgery*, 10(3):263–274. *Cited page 84*

[Bae et al., 2019] Bae, M. R., Kang, W. S., and Chung, J. W. (2019). Comparison of the clinical results of attic cholesteatoma treatment: endoscopic versus microscopic ear surgery. *Clinical and experimental otorhinolaryngology*, 12(2):156. *Cited page 12*

[Bansal, 2012] Bansal, M. (2012). *Diseases of ear, nose and throat*. JP Medical Ltd. *2 citations page iii and 11*

[Blanco et al., 2014] Blanco, P., González, F., Holguín, J., and Guerra, C. (2014). Surgical management of middle ear cholesteatoma and reconstruction at the same time. *Colombia Médica*, 45(3):127–131. *Cited page 13*

[Bordure et al., 2005] Bordure, P., Robier, A., and Malard, O. (2005). *Chirurgie otologique et otoneurologique*. Elsevier Masson. *2 citations page 12 and 14*

[Brdjanin et al., 2020] Brdjanin, A., Dardagan, N., Dzigal, D., and Akagic, A. (2020). Single object trackers in opencv: A benchmark. In *2020 International Conference on INnovations in Intelligent SysTems and Applications (INISTA)*, pages 1–6. IEEE. *Cited page 89*

[Burgner-Kahrs et al., 2015] Burgner-Kahrs, J., Rucker, D. C., and Choset, H. (2015). Continuum robots for medical applications: A survey. *IEEE Transactions on Robotics*, 31(6):1261–1280. *Cited page 14*

[Caffier et al., 2008] Caffier, P. P., Marzahn, U., Franke, A., Sudhoff, H., Jovanovic, S., Haisch, A., and Sedlmaier, B. (2008). Laser-assisted cholesteatoma surgery: technical aspects, in vitro implementation and challenge of selective cell destruction. *European archives of oto-rhino-laryngology*, 265(10):1179–1188. *Cited page 14*

[Calandre et al., 2021] Calandre, J., Péteri, R., Mascarilla, L., and Tremblais, B. (2021). Table tennis ball kinematic parameters estimation from non-intrusive single-view videos. In *2021 International Conference on Content-Based Multimedia Indexing (CBMI)*, pages 1–6. IEEE. *Cited page 89*

[Chaumette, 2020] Chaumette, F. (2020). Visual Servoing. In *Encyclopedia of Robotics*, pages 1–9. Springer Berlin Heidelberg. *Cited page 93*

[Chaumette and Hutchinson, 2006] Chaumette, F. and Hutchinson, S. (2006). Visual servo control. i. basic approaches. *IEEE Robotics & Automation Magazine*, 13(4):82–90. *2 citations page 67 and 92*

[Chng et al., 2015] Chng, C.-B., Ho, Y., and Chui, C.-K. (2015). Automation of retinal surgery: A shared control robotic system for laser ablation. In *2015 IEEE International Conference on Information and Automation*, pages 1957–1962. IEEE. *2 citations page v and 86*

[Colan et al., 2020] Colan, J., Nakanishi, J., Aoyama, T., and Hasegawa, Y. (2020). A cooperative human-robot interface for constrained manipulation in robot-assisted endonasal surgery. *Applied Sciences*, 10(14). *3 citations page iv, 60, and 61*

[Dahroug et al., 2020a] Dahroug, B., Tamadazte, B., and Andreff, N. (2020a). Pca-based visual servoing using optical coherence tomography. *IEEE Robotics and Automation Letters*, 5(2):3430–3437. *Cited page 108*

[Dahroug et al., 2020b] Dahroug, B., Tamadazte, B., and Andreff, N. (2020b). Unilaterally constrained motion of a curved surgical tool. *Robotica*, 38(11):1940–1962. *Cited page 30*

[Dahroug et al., 2018a] Dahroug, B., Tamadazte, B., Tavernier, L., Weber, S., and Andreff, N. (2018a). Review on otological robotic systems: Toward micro-robot assisted cholesteatoma surgery. *IEEE Reviews in Biomedical Engineering*, 11:125 – 142. *Cited page 91*

[Dahroug et al., 2018b] Dahroug, B., Tamadazte, B., Weber, S., Tavernier, L., and Andreff, N. (2018b). Review on otological robotic systems: toward microrobot-assisted cholesteatoma surgery. *IEEE reviews in biomedical engineering*, 11:125–142. *6 citations page 3, 13, 20, 25, 46, and 53*

[Danilchenko et al., 2011] Danilchenko, A., Balachandran, R., Toennies, J. L., Baron, S., Munske, B., Fitzpatrick, J. M., Withrow, T. J., Webster III, R. J., and Labadie, R. F. (2011). Robotic mastoidectomy. *Otology & neurotology: official publication of the American Otological Society, American Neurotology Society [and] European Academy of Otology and Neurotology*, 32(1):11. *2 citations page iii and 16*

[De Foer et al., 2008] De Foer, B., Vercruysse, J.-P., Bernaerts, A., Deckers, F., Pouillon, M., Somers, T., Casselman, J., and Offeciers, E. (2008). Detection of postoperative residual cholesteatoma with non-echo-planar diffusion-weighted magnetic resonance imaging. *Otology & Neurotology*, 29(4):513–517. *Cited page 82*

[Dhingra, 2010] Dhingra, P. (2010). *Diseases of Ear, Nose & Throat*. Elsevier India. *3 citations page iii, 10, and 11*

[Dillon et al., 2014] Dillon, N. P., Balachandran, R., dit Falisse, A. M., Wanna, G. B., Labadie, R. F., Withrow, T. J., Fitzpatrick, J. M., and Webster III, R. J. (2014). Preliminary testing of a compact bone-attached robot for otologic surgery. In

Medical Imaging 2014: Image-Guided Procedures, Robotic Interventions, and Modeling, volume 9036, page 903614. International Society for Optics and Photonics. *2 citations page iii and 17*

[Du et al., 2014] Du, G., Zhang, P., and Li, D. (2014). Human-manipulator interface based on multisensory process via kalman filters. *IEEE Transactions on Industrial Electronics*, 61(10):5411–5418. *Cited page 38*

[Entsfellner et al., 2015] Entsfellner, K., Schuermann, J., Coy, J. A., Strauss, G., and Lueth, T. C. (2015). A modular micro-macro robot system for instrument guiding in middle ear surgery. In *2015 IEEE International Conference on Robotics and Biomimetics (ROBIO)*, pages 374–379. IEEE. *2 citations page iii and 18*

[Entsfellner et al., 2012] Entsfellner, K., Strauss, G., Berger, T., Dietz, A., and Lueth, T. C. (2012). Micro-macro telemanipulator for middle-ear microsurgery. In *ROBOTIK 2012; 7th German Conference on Robotics*, pages 1–4. VDE. *2 citations page iv and 36*

[Espiau et al., 1992] Espiau, B., Chaumette, F., and Rives, P. (1992). A new approach to visual servoing in robotics. *ieee Transactions on Robotics and Automation*, 8(3):313–326. *Cited page 83*

[Fang et al., 2017] Fang, B., Sun, F., Liu, H., Guo, D., Chen, W., and Yao, G. (2017). Robotic teleoperation systems using a wearable multimodal fusion device. *International journal of advanced robotic systems*, 14(4):1729881417717057. *Cited page 38*

[Fichera, 2016] Fichera, L. (2016). Learning the temperature dynamics during thermal laser ablation. In *Cognitive Supervision for Robot-Assisted Minimally Invasive Laser Surgery*, pages 43–62. Springer. *Cited page 95*

[Fichera, 2021] Fichera, L. (2021). Bringing the light inside the body to perform better surgery. *Science Robotics*, 6(50):eabf1523. *Cited page 82*

[Fichera et al., 2017] Fichera, L., Dillon, N. P., Zhang, D., Godage, I. S., Siebold, M. A., Hartley, B. I., Noble, J. H., Russell, P. T., Labadie, R. F., and Webster, R. J. (2017). Through the eustachian tube and beyond: A new miniature robotic endoscope to see into the middle ear. *IEEE Rob. and Auto. Let.*, 2(3):1488–1494. *Cited page 20*

[Franco et al., 2015] Franco, E., Brujic, D., Rea, M., Gedroyc, W. M., and Ristic, M. (2015). Needle-guiding robot for laser ablation of liver tumors under mri guidance. *IEEE/ASME Transactions on Mechatronics*, 21(2):931–944. *2 citations page v and 85*

[Fuchs, 2002] Fuchs, K. (2002). Minimally invasive surgery. *Endoscopy*, 34(02):154–159. *Cited page 33*

[Gaillardin et al., 2012] Gaillardin, L., Lescanne, E., Morinière, S., Cottier, J.-P., and Robier, A. (2012). Residual cholesteatoma: prevalence and location. follow-up strategy

in adults. *European annals of otorhinolaryngology, head and neck diseases*, 129(3):136–140. *Cited page 81*

[Gijbels et al., 2014] Gijbels, A., Vander Poorten, E. B., Gorissen, B., Devreker, A., Stalmans, P., and Reynaerts, D. (2014). Experimental validation of a robotic comanipulation and telemanipulation system for retinal surgery. In *5th IEEE RAS/EMBS International Conference on Biomedical Robotics and Biomechatronics*, pages 144–150. IEEE. *Cited page 42*

[Goertz, 1949] Goertz, R. C. (1949). *Master-slave manipulator*, volume 2635. Argonne National Laboratory. *Cited page 32*

[Goertz and Thompson, 1954] Goertz, R. C. and Thompson, W. M. (1954). Electronically controlled manipulator. *Nucleonics (US) Ceased publication*, 12. *Cited page 32*

[Gora et al., 2017] Gora, M. J., Suter, M. J., Tearney, G. J., and Li, X. (2017). Endoscopic optical coherence tomography: technologies and clinical applications. *Biomedical optics express*, 8(5):2405–2444. *Cited page 89*

[Gosline et al., 2012] Gosline, A. H., Vasilyev, N. V., Veeramani, A., Wu, M., Schmitz, G., Chen, R., Arabagi, V., Pedro, J., and Dupont, P. E. (2012). Metal mems tools for beating-heart tissue removal. In *2012 IEEE International Conference on Robotics and Automation*, pages 1921–1926. IEEE. *2 citations page 14 and 20*

[Guthart and Salisbury, 2000] Guthart, G. S. and Salisbury, J. K. (2000). The intuitive/-sup tm/telesurgery system: overview and application. In *Proceedings 2000 ICRA. Millennium Conference. IEEE International Conference on Robotics and Automation. Symposia Proceedings (Cat. No. 00CH37065)*, volume 1, pages 618–621. IEEE. *2 citations page 32 and 60*

[Habermann, 1888] Habermann, F. (1888). Zur entstehung des cholesteatoms des mittelohres. *Archiv für Ohrenheilkunde*, 27(2):230–230. *Cited page 11*

[Hagag et al., 2011] Hagag, B., Abovitz, R., Kang, H., Schmitz, B., and Conditt, M. (2011). Rio: Robotic-arm interactive orthopedic system makoplasty: User interactive haptic orthopedic robotics. In *Surgical robotics*, pages 219–246. Springer. *Cited page 41*

[Hamilton, 2005] Hamilton, J. W. (2005). Efficacy of the ktp laser in the treatment of middle ear cholesteatoma. *Otology & Neurotology*, 26(2):135–139. *2 citations page 14 and 83*

[Hessinger et al., 2015] Hessinger, M., Müller, R., Werthschützky, R., and Pott, P. (2015). Tool position control of an upper limb exoskeleton for robot-assisted surgery. *IFAC-PapersOnLine*, 48(20):195–200. 9th IFAC Symposium on Biological and Medical Systems BMS 2015. *2 citations page 40 and 41*

[Heunis et al., 2012] Heunis, J. S., Scheffer, C., and Schreve, K. (2012). A user interface for a seven degree of freedom surgical robot. In *2012 5th Robotics and Mechatronics Conference of South Africa*, pages 1–6. IEEE. *2 citations page iv and 37*

[Hildmann and Sudhoff, 2006] Hildmann, H. and Sudhoff, H. (2006). *Middle ear surgery*. Springer Science & Business Media. *5 citations page iii, 12, 13, 14, and 16*

[Hokayem and Spong, 2006] Hokayem, P. F. and Spong, M. W. (2006). Bilateral teleoperation: An historical survey. *Automatica*, 42(12):2035–2057. *3 citations page iii, 33, and 34*

[Hu et al., 2018] Hu, D., Gong, Y., Seibel, E. J., Sekhar, L. N., and Hannaford, B. (2018). Semi-autonomous image-guided brain tumour resection using an integrated robotic system: A bench-top study. *The International Journal of Medical Robotics and Computer Assisted Surgery*, 14(1):e1872. *Cited page 94*

[Huang et al., 1991] Huang, D., Swanson, E. A., Lin, C. P., Schuman, J. S., Stinson, W. G., Chang, W., Hee, M. R., Flotte, T., Gregory, K., Puliafito, C. A., et al. (1991). Optical coherence tomography. *science*, 254(5035):1178–1181. *Cited page 14*

[Jang et al., 2002] Jang, I.-K., Bouma, B. E., Kang, D.-H., Park, S.-J., Park, S.-W., Seung, K.-B., Choi, K.-B., Shishkov, M., Schlendorf, K., Pomerantsev, E., et al. (2002). Visualization of coronary atherosclerotic plaques in patients using optical coherence tomography: comparison with intravascular ultrasound. *Journal of the American College of Cardiology*, 39(4):604–609. *2 citations page 14 and 89*

[Kahrs et al., 2008] Kahrs, L. A., Raczkowsky, J., Werner, M., Knapp, F. B., Mehrwald, M., Hering, P., Schipper, J., Klenzner, T., and Wörn, H. (2008). Visual servoing of a laser ablation based cochleostomy. In *Medical Imaging 2008: Visualization, Image-Guided Procedures, and Modeling*, volume 6918, page 69182C. International Society for Optics and Photonics. *3 citations page v, 84, and 85*

[Katanacho et al., 2016] Katanacho, M., De la Cadena, W., and Engel, S. (2016). Surgical navigation with qr codes: Marker detection and pose estimation of qr code markers for surgical navigation. *Current Directions in Biomedical Engineering*, 2(1):355–358. *Cited page 68*

[Kobayashi et al., 2013] Kobayashi, F., Kitabayashi, K., Nakamoto, H., and Kojima, F. (2013). Hand/arm robot teleoperation by inertial motion capture. In *2013 Second international conference on robot, vision and signal processing*, pages 234–237. IEEE. *3 citations page iv, 37, and 38*

[Koliakos et al., 2008] Koliakos, N., Denaeyer, G., Willemsen, P., Schatteman, P., and Mottrie, A. (2008). Failure of a robotic arm during da vinci prostatectomy: a case report. *Journal of robotic surgery*, 2(2):95–96. *Cited page 19*

[Lademann et al., 2007] Lademann, J., Otberg, N., Richter, H., Meyer, L., Audring, H., Teichmann, A., Thomas, S., Knüttel, A., and Sterry, W. (2007). Application of optical non-invasive methods in skin physiology: a comparison of laser scanning microscopy and optical coherent tomography with histological analysis. *Skin Research and Technology*, 13(2):119–132. *2 citations page 14 and 89*

[Lawler, 1985] Lawler, E. L. (1985). The traveling salesman problem: a guided tour of combinatorial optimization. *Wiley-Interscience Series in Discrete Mathematics*. *Cited page 96*

[Liang et al., 2017] Liang, W., Gao, W., and Tan, K. K. (2017). Stabilization system on an office-based ear surgical device by force and vision feedback. *Mechatronics*, 42:1–10. *Cited page 64*

[Lichiardopol, 2007] Lichiardopol, S. (2007). A survey on teleoperation. *Technische Universitat Eindhoven, DCT report*, 20:40–60. *Cited page 33*

[Liu et al., 2019] Liu, L., Mariani, S. G., De Schlichting, E., Grand, S., Lefranc, M., Seigneuret, E., and Chabardès, S. (2019). Frameless ROSA® Robot-Assisted Lead Implantation for Deep Brain Stimulation: Technique and Accuracy. *Operative Neurosurgery*, 19(1):57–64. *2 citations page 62 and 68*

[Lukezic et al., 2017] Lukezic, A., Vojir, T., ˇCehovin Zajc, L., Matas, J., and Kristan, M. (2017). Discriminative correlation filter with channel and spatial reliability. In *Proceedings of the IEEE conference on computer vision and pattern recognition*, pages 6309–6318. *Cited page 88*

[Madhani, 1998] Madhani, A. J. (1998). *Design of teleoperated surgical instruments for minimally invasive surgery*. PhD thesis, Massachusetts Institute of Technology. *Cited page 1*

[Maillet et al., 2005] Maillet, P., Nahum, B., Blondel, L., Poignet, P., and Dombre, E. (2005). Brigit, a robotized tool guide for orthopedic surgery. In *Proceedings of the 2005 IEEE International Conference on Robotics and Automation*, pages 211–216. IEEE. *2 citations page iv and 61*

[Malis et al., 1999] Malis, E., Chaumette, F., and Boudet, S. (1999). 2 1/2 d visual servoing. *IEEE Transactions on Robotics and Automation*, 15(2):238–250. *Cited page 69*

[Marchand et al., 2002] Marchand, E., Chaumette, F., Spindler, F., and Perrier, M. (2002). Controlling an uninstrumented manipulator by visual servoing. *The International Journal of Robotics Research*, 21(7):635–647. *Cited page 68*

[Marchand et al., 2005] Marchand, É., Spindler, F., and Chaumette, F. (2005). Visp for visual servoing: a generic software platform with a wide class of robot control skills. *IEEE Robotics & Automation Magazine*, 12(4):40–52. *Cited page 89*

[Marescaux and Rubino, 2003] Marescaux, J. and Rubino, F. (2003). The zeus robotic system: experimental and clinical applications. *Surgical Clinics*, 83(6):1305–1315. *2 citations page 2 and 32*

[Mehrdad et al., 2021] Mehrdad, S., Liu, F., Pham, M. T., Lelevé, A., and Atashzar, S. F. (2021). Review of advanced medical telerobots. *Applied Sciences*, 11(1):209. *Cited page 34*

[Mezouar et al., 2007] Mezouar, Y., Prats, M., and Martinet, P. (2007). External hybrid vision/force control. In *Intl. Conference on Advanced Robotics (ICAR07)*, pages 170–175. *2 citations page 64 and 67*

[Miroir et al., 2012] Miroir, M., Nguyen, Y., Szewczyk, J., Sterkers, O., and Bozorg Grayeli, A. (2012). Design, kinematic optimization, and evaluation of a teleoperated system for middle ear microsurgery. *The Scientific World Journal*, 2012. *2 citations page iii and 18*

[Mohiuddin and Swanson, 2013] Mohiuddin, K. and Swanson, S. J. (2013). Maximizing the benefit of minimally invasive surgery. *Journal of surgical oncology*, 108(5):315–319. *Cited page 2*

[Monroy et al., 2015] Monroy, G. L., Shelton, R. L., Nolan, R. M., Nguyen, C. T., Novak, M. A., Hill, M. C., McCormick, D. T., and Boppart, S. A. (2015). Noninvasive depth-resolved optical measurements of the tympanic membrane and middle ear for differentiating otitis media. *The Laryngoscope*, 125(8):E276–E282. *Cited page 15*

[Moorthy et al., 2004] Moorthy, K., Munz, Y., Dosis, A., Hernandez, J., Martin, S., Bello, F., Rockall, T., and Darzi, A. (2004). Dexterity enhancement with robotic surgery. *Surgical Endoscopy and Other Interventional Techniques*, 18(5):790–795. *Cited page 33*

[Morel et al., 1998] Morel, G., Malis, E., and Boudet, S. (1998). Impedance based combination of visual and force control. In *Proceedings. 1998 IEEE International Conference on Robotics and Automation (Cat. No. 98CH36146)*, volume 2, pages 1743–1748. *Cited page 64*

[Morel et al., 2013] Morel, G., Szewczyk, J., and Vitrani, M.-A. (2013). Comanipulation. *Medical Robotics*, pages 303–350. *4 citations page iv, 38, 39, and 41*

[Nelson et al., 2002] Nelson, M., Roger, G., Koltai, P. J., Garabedian, E.-N., Triglia, J.-M., Roman, S., Castellon, R. J., and Hammel, J. P. (2002). Congenital Cholesteatoma: Classification, Management, and Outcome. *Archives of Otolaryngology–Head & Neck Surgery*, 128(7):810–814. *Cited page 11*

[Nguyen et al., 2021] Nguyen, D., Girerd, C., Boyer, Q., Rougeot, P., Lehmann, O., Tavernier, L., Szewczyk, J., and Rabenorosoa, K. (2021). A hybrid concentric tube robot

for cholesteatoma laser surgery. *IEEE Robotics and Automation Letters*, 7(1):462–469. *4 citations page vi, 23, 107, and 108*

[Nguyen et al., 2012] Nguyen, Y., Miroir, M., Kazmitcheff, G., Ferrary, E., Sterkers, O., and Grayeli, A. B. (2012). From conception to application of a tele-operated assistance robot for middle ear surgery. *Surgical innovation*, 19(3):241–251. *Cited page 18*

[Oka and Matsushima, 2016] Oka, T. and Matsushima, K. (2016). Evaluation of a three-mode robotic manipulator control interface that employs voice and multi-touch commands. In *2016 IEEE International Conference on Advanced Intelligent Mechatronics (AIM)*, pages 130–135. IEEE. *2 citations page iv and 35*

[Olson, 2011] Olson, E. (2011). Apriltag: A robust and flexible visual fiducial system. In *2011 IEEE International Conference on Robotics and Automation*, pages 3400–3407. IEEE. *Cited page 72*

[Olszewska et al., 2004] Olszewska, E., Wagner, M., Bernal-Sprekelsen, M., Ebmeyer, J., Dazert, S., Hildmann, H., and Sudhoff, H. (2004). Etiopathogenesis of cholesteatoma. *European Archives of Oto-Rhino-Laryngology and Head & Neck*, 261(1):6–24. *2 citations page 10 and 11*

[Ott et al., 2011] Ott, L., Nageotte, F., Zanne, P., and de Mathelin, M. (2011). Robotic assistance to flexible endoscopy by physiological-motion tracking. *IEEE Transactions on Robotics*, 27(2):346–359. *2 citations page 20 and 44*

[Ourak et al., 2016a] Ourak, M., De Simone, A., Tamadazte, B., Laurent, G. J., Menciassi, A., and Andreff, N. (2016a). Automated in-plane oct-probe positioning towards repetitive optical biopsies. In *2016 IEEE International Conference on Robotics and Automation (ICRA)*, pages 4186–4191. IEEE. *Cited page 108*

[Ourak et al., 2016b] Ourak, M., Tamadazte, B., and Andreff, N. (2016b). Partitioned camera-oct based 6 dof visual servoing for automatic repetitive optical biopsies. In *2016 IEEE/RSJ International Conference on Intelligent Robots and Systems (IROS)*, pages 2337–2342. IEEE. *2 citations page 67 and 108*

[Ourak et al., 2019] Ourak, M., Tamadazte, B., Lehmann, O., and Andreff, N. (2019). Direct visual servoing using wavelet coefficients. *IEEE/ASME Transactions on Mechatronics*, 24(3):1129–1140. *Cited page 108*

[Park et al., 2018] Park, J. H., Ahn, J., and Moon, I. J. (2018). Transcanal endoscopic ear surgery for congenital cholesteatoma. *Clinical and experimental otorhinolaryngology*, 11(4):233. *Cited page 82*

[Parmar et al., 2010] Parmar, A., Grant, D. G., and Loizou, P. (2010). Robotic surgery in ear nose and throat. *European archives of oto-rhino-laryngology*, 267(4):625–633. *Cited page 15*

[Pitris et al., 2001] Pitris, C., Saunders, K. T., Fujimoto, J. G., and Brezinski, M. E. (2001). High-resolution imaging of the middle ear with optical coherence tomography: a feasibility study. *Archives of Otolaryngology–Head & Neck Surgery*, 127(6):637–642. *Cited page 15*

[Prasad et al., 2004] Prasad, S. M., Prasad, S. M., Maniar, H. S., Chu, C., Schuessler, R. B., and Damiano Jr, R. J. (2004). Surgical robotics: impact of motion scaling on task performance. *Journal of the American College of Surgeons*, 199(6):863–868. *Cited page 33*

[Prats et al., 2007] Prats, M., Martinet, P., del Pobil, A. P., and Lee, S. (2007). Vision force control in task-oriented grasping and manipulation. In *2007 IEEE/RSJ International Conference on Intelligent Robots and Systems*, pages 1320–1325. *Cited page 64*

[Renevier et al., 2016] Renevier, R., Tamadazte, B., Rabenorosoa, K., Tavernier, L., and Andreff, N. (2016). Endoscopic laser surgery: Design, modeling, and control. *IEEE/ASME Transactions on Mechatronics*, 22(1):99–106. *Cited page 84*

[Robert J. Webster and Jones, 2010] Robert J. Webster, I. and Jones, B. A. (2010). Design and kinematic modeling of constant curvature continuum robots: A review. *The International Journal of Robotics Research*, 29(13):1661–1683. *Cited page 44*

[Rüedi, 1959] Rüedi, L. (1959). Cholesteatoma formation in the middle ear in animal experiments. *Acta Oto-Laryngologica*, 50(3-6):233–242. *Cited page 12*

[Sade et al., 1983] Sade, J., Babiacki, A., and Pinkus, G. (1983). The metaplastic and congenital origin of cholesteatoma. *Acta oto-laryngologica*, 96(1-2):119–129. *Cited page 12*

[Scheiner and Schmitt, 2019] Scheiner, B. and Schmitt, M. (2019). The role of incidence angle in the laser ablation of a planar target. *Physics of Plasmas*, 26(2):024502. *Cited page 54*

[Seon et al., 2014] Seon, J.-A., Tamadazte, B., and Andreff, N. (2014). Path following: from mobile robotics to laser surgery. In *3rd Work. on Visual Control of Mobile Rob. at IEEE/RSJ Int. Conf. on Intel. Rob. and Sys*, pages 8–15. *Cited page 86*

[Seon et al., 2015] Seon, J.-A., Tamadazte, B., and Andreff, N. (2015). Decoupling path following and velocity profile in vision-guided laser steering. *IEEE Transactions on Robotics*, 31(2):280–289. *2 citations page v and 86*

[Sharon et al., 1993] Sharon, A., Hogan, N., and Hardt, D. E. (1993). The macro/micro manipulator: An improved architecture for robot control. *Robotics and computer-integrated manufacturing*, 10(3):209–222. *Cited page 21*

[Sheridan, 1995] Sheridan, T. B. (1995). Teleoperation, telerobotics and telepresence: A progress report. *Control Engineering Practice*, 3(2):205–214. *Cited page 32*

[Siciliano et al., 2008] Siciliano, B., Khatib, O., and Kröger, T. (2008). *Springer handbook of robotics*, volume 200. Springer. *Cited page 47*

[Simorov et al., 2012] Simorov, A., Otte, S., and Kopietz, C. e. a. (2012). Review of surgical robotics user interface: what is the best way to control robotic surgery? *Surgical endoscopy*, 26:2117–25. *2 citations page 34 and 35*

[Smoljkic et al., 2016] Smoljkic, G., Borghesan, G., Devreker, A., Vander Poorten, E., Rosa, B., De Praetere, H., De Schutter, J., Reynaerts, D., and Vander Sloten, J. (2016). Control of a hybrid robotic system for computer-assisted interventions in dynamic environments. *International journal of computer assisted radiology and surgery*, 11(7):1371–1383. *2 citations page iii and 22*

[So et al., 2022a] So, J.-H., , Sobucki, S., Szewczyk, J., Marturi, N., and Tamadazte, B. (2022a). Hybrid controllers for middle ear surgery: towards efficient cholesteatoma removal. *Conference on New Technologies for Computer and Robot Assisted Surgery (CRAS)*. *2 citations page 4 and 67*

[So et al., 2022b] So, J.-H., , Sobucki, S., Szewczyk, J., Marturi, N., and Tamadazte, B. (2022b). Shared control schemes for middle ear surgery. *Frontiers in Robotics and AI*. *2 citations page 4 and 67*

[So et al., 2022c] So, J.-H., Tamadazte, B., Marturi, N., and Szewczyk, J. (2022c). Dual-scale robotic solution for middle ear surgery. In *2022 IEEE International Conference on Robotics and Automation (ICRA)*. IEEE. *Cited page 3*

[So et al., 2020] So, J.-H., Tamadazte, B., and Szewczyk, J. (2020). Micro/macro-scale robotic approach for middle ear surgery. *IEEE Transactions on Medical Robotics and Bionics*, 2(4):533–536. *Cited page 4*

[So et al., 2022d] So, J.-H., Tamadazte, B., and Szewczyk, J. (2022d). Image-guided laser steering for middle ear surgery. In *2022 IEEE/RSJ International Conference on Intelligent Robots and Systems (IROS)*. IEEE. *Cited page 4*

[Stevens et al., 2019] Stevens, S. M., Walters, Z. A., Babo, K., Peddireddy, N., Tawfik, K. O., and Samy, R. N. (2019). Canal reconstruction mastoidectomy: Outcomes comparison following primary versus secondary surgery. *The Laryngoscope*, 129(11):2580–2587. *Cited page 13*

[Su et al., 2018] Su, H., Sandoval, J., Makhdoomi, M., Ferrigno, G., and De Momi, E. (2018). Safety-enhanced human-robot interaction control of redundant robot for teleoperated minimally invasive surgery. In *2018 IEEE International Conference on Robotics and Automation (ICRA)*, pages 6611–6616. IEEE. *Cited page 30*

[Tamadazte et al., 2018] Tamadazte, B., Renevier, R., Séon, J.-A., Kudryavtsev, A. V., and Andreff, N. (2018). Laser beam steering along three-dimensional paths. *IEEE/ASME Transactions on Mechatronics*, 23(3):1148–1158. *Cited page 84*

[Tan et al., 2018] Tan, H. E. I., Santa Maria, P. L., Wijesinghe, P., Francis Kennedy, B., Allardyce, B. J., Eikelboom, R. H., Atlas, M. D., and Dilley, R. J. (2018). Optical coherence tomography of the tympanic membrane and middle ear: a review. *Otolaryngology–Head and Neck Surgery*, 159(3):424–438. *Cited page 15*

[Taylor et al., 2016] Taylor, R. H., Menciassi, A., Fichtinger, G., Fiorini, P., and Dario, P. (2016). Medical robotics and computer-integrated surgery. In *Springer handbook of robotics*, pages 1657–1684. Springer. *Cited page 2*

[Tian et al., 2019] Tian, W., Liu, Y.-j., Liu, B., He, D., Wu, J.-y., Han, X.-g., Zhao, J.-w., Fan, M.-x., on Medical Robot Engineering of Chinese Society of Biomedical Engineering, T. C., and of National Robotic Orthopaedic Surgery Application Center, T. C. C. (2019). Guideline for thoracolumbar pedicle screw placement assisted by orthopaedic surgical robot. *Orthopaedic surgery*, 11(2):153–159. *2 citations page iv and 62*

[Tobergte et al., 2011] Tobergte, A., Helmer, P., Hagn, U., Rouiller, P., Thielmann, S., Grange, S., Albu-Schäffer, A., Conti, F., and Hirzinger, G. (2011). The sigma.7 haptic interface for mirosurge: A new bi-manual surgical console. In *2011 IEEE/RSJ International Conference on Intelligent Robots and Systems*, pages 3023–3030. *2 citations page iii and 35*

[Troccaz, 2013] Troccaz, J. (2013). *Medical Robotics*. John Wiley & Sons, Inc., Hoboken, NJ USA. *Cited page 2*

[Vitiello et al., 2013] Vitiello, V., Su-Lin Lee, Cundy, T. P., and Guang-Zhong Yang (2013). Emerging Robotic Platforms for Minimally Invasive Surgery. *IEEE Reviews in Biomedical Engineering*, 6:111–126. *Cited page 15*

[Webster III and Jones, 2010] Webster III, R. J. and Jones, B. A. (2010). Design and kinematic modeling of constant curvature continuum robots: A review. *The Int. J. of Rob. Res.*, 29(13):1661–1683. *Cited page 44*

[Wijesoma et al., 1993] Wijesoma, S., Wolfe, D., and Richards, R. (1993). Eye-to-hand coordination for vision-guided robot control applications. *The International Journal of Robotics Research*, 12(1):65–78. *Cited page 91*

[Williams et al., 2003] Williams, M. T., Ayache, D., Alberti, C., Héran, F., Lafitte, F., Elmaleh-Bergès, M., and Piekarski, J.-D. (2003). Detection of postoperative residual cholesteatoma with delayed contrast-enhanced mr imaging: initial findings. *European radiology*, 13(1):169–174. *Cited page 82*

[Wittmaack, 1933] Wittmaack, K. (1933). Wie entsteht ein genuines cholesteatom? *Archiv für Ohren-, Nasen-und Kehlkopfheilkunde*, 137(4):306–332. *Cited page 11*

[Zhan et al., 2015] Zhan, Y., Duan, X.-G., and Li, J.-X. (2015). Review of Comanipulation Robot in Surgery. *2015 IEEE International Conference on Mechatronics and Automation*, pages 1466–1471. *Cited page 41*

[Zhang et al., 2020] Zhang, X., Li, W., Chiu, P. W. Y., and Li, Z. (2020). A novel flexible robotic endoscope with constrained tendon-driven continuum mechanism. *IEEE Robotics and Automation Letters*, 5(2):1366–1372. *2 citations page iii and 21*

[Zhang et al., 2021] Zhang, Z., Rosa, B., Mora, O. C., Zanne, P., Gora, M., and Nageotte, F. (2021). Image-guided control of an endoscopic robot for oct path scanning. *IEEE Robotics and Automation Letters*. *Cited page 108*